

[1996]



This is to certify that the

dissertation entitled

1/F NOISE AND QUANTUM TRANSPORT IN THE LOW SPIN-ORBIT SCATTERING LIMIT

presented by

Jeong-Sun Moon

has been accepted towards fulfillment of the requirements for

Doctor degree in Philosophy

Morman O. Brys Major professor

/ /

MSU is an Affirmative Action/Equal Opportunity Institution

0-12771

LIBRARY Michigan State University

PLACE IN RETURN BOX to remove this checkout from your record. TO AVOID FINES return on or before date due.

DATE DUE	DATE DUE	DATE DUE

MSU is An Affirmative Action/Equal Opportunity Institution

1/F NOISE AND QUANTUM TRANSPORT IN THE LOW SPIN-ORBIT SCATTERING LIMIT

By Jeong-Sun Moon

A DISSERTATION

Submitted to
Michigan State University
in partial fulfillment of the requirements for the degree of

DOCTOR OF PHILOSOPHY

Department of Physics and Astronomy and Center for Fundamental Materials Research

ABSTRACT

1/F NOISE AND QUANTUM TRANSPORT IN THE LOW SPIN-ORBIT SCATTERING LIMIT

By

Jeong-Sun Moon

Recent advances in microfabrication technology have enabled the experimental investigation of quantum interference effects on electron transport in disordered systems. At low temperature, the electrons diffuse coherently for a distance which can become much longer than the elastic mean free path. The resulting quantum interference among diffusive paths gives rise to universal conductance fluctuations(UCF), in which the conductance fluctuates chaotically as a function of a control parameter by a universal amplitude $\delta G \sim e^2/h$ at zero temperature, independent of the magnitude of the conductance itself. Recent theoretical developments provide a connection between UCF and random matrix theory(RMT), pioneered by Wigner and Dyson. It is shown that the conductance is related to the eigenvalues of the transmission matrix and the relative amplitude of the conductance fluctuations is governed by the symmetry of the transfer matrix.

This thesis describes low temperature measurements of 1/f noise on a quench-condensed quasi-1D Li wire, to study UCF in a low spin-orbit and spin-flip scattering system, which has the feature of maximum symmetry in the absence of a magnetic field. We observed two distinct reductions by factors of 2 in the noise versus magnetic field: the first from breaking time-reversal symmetry and the second due to lifting the Zeeman degeneracy. We measure and calculate the complete crossover function for both reductions, and find good agreement over the range 0 to 9 T. Our

results show that the magnetic field scale for the Zeeman crossover is determined by the sample temperature, rather than by the Thouless energy.

We also studied the effect of the spin-flip scattering on conductance fluctuations in the regime where the magnetic spin-flip scattering rate is comparable to the electron phase breaking rate. We found that the magnitude of conductance fluctuations is affected in a dramatic way: 1/f noise is reduced by factor of 2 at low magnetic field and increases dramatically at high field. The results are interpreted that the magnetic field induces a transition from a low-field state where the impurity spins are free to flip and destroy the phase coherence to a high-field state where spin-flip scattering is frozen and recover the universal conductance fluctuations.

To my dearest wife Kyung-ah and son sol and my parents

ACKNOWLEDGMENTS

I am grateful to Professor Norman O. Birge, my thesis advisor, for his insight, encouragement and efforts to provide me with a complete Ph.D. training. He always taught me deeper understanding of physics and instrumentation. I also thank Professor Brage Golding who helped design this research project and provided us with lots of useful information and microfabrication facilities. I have benefitted a great deal from Professor Mark Dykman and S. D. Mahanti. I also thank Professor H. Smith and V. Zelevinsky for being guidance committee members.

I thank the support from other members of Birge's group who care about my research: Dr. Kookjin Chun, Dr. Paul McConville, David Hoadley and Matt Miller. Dr. Chun, we shared a wonderful time together while discussing lithography and life in E. Lansing, and even while finding a leak in the dilution refrigerator. Dr. McConville, he taught me the complicated UCF theory with simple cartoon-type pictures. Mr. Hoadley, he is behind me but is smart so that I have learned from him. Mr. Miller, he always has nice jokes to make me laugh and I won't forget the old leak detector he completely fixed. I especially thank A. Engebretson and M. Jaeger for helpful discussion on the microfabrication. I enjoyed the friendship with other Korean students, and especially thank Sangil Hyun.

Most of all, I would like to thank the support from my parents who always show me what is valuable in my life, and my dear wife who gives me a smile with love while we are traveling against the wind. My happiness is rooted and grows with the love from my family.

Once more I like to thank my advisor for his warm care about my outside life.

This work is supported by the Center for Fundamental Materials Research at Michigan State University and the National Science Foundation under Grant # DMR-9321850.

TABLE OF CONTENTS

	LIST OF TABLES	1X
	LIST OF FIGURES	x
<i>1</i> .	INTRODUCTION	1
	References	8
2 .	THEORY OF QUANTUM TRANSPORT	10
	A. Diffusive Quantum Transport in Metal	10
	B. Landauer's Conductance	10
	C. Universal Conductance Fluctuations (UCF)	11
	C.1 Random Matrix Approach	12
	C.2 Random Hamiltonian Approach	15
	C.3 Diagrammatic Approach	17
	C.4 The Amplitude of UCF	18
	D. Quantitative Analysis of UCF	20
	D.1 Field correlation, Variance and UCF noise	20
	D.2 UCF Crossover Function at weak Magnetic Field	22
	D.3 UCF Crossover Function at strong Magnetic Field	28
	E. Weak-Localization and low-field Magnetoresistance	32
	References	34
<i>3</i> .	EXPERIMENTAL TECHNIQUES	41
	A. Quench-Condensation	41
	B. Electron-beam Lithography	43
	B.1 Resolution and Undercut Profile	44
	B.2 Sub-micron Metal Stencil	46

	C. Optical Lithography	52
	D. 1/f Noise Measurement	55
	C.1 Dual-Phase Technique	55
	C.2 Digital Lock-in Amplifier	56
	References	59
4 .	ZEEMAN EFFECT on UCF	74
	A. Introduction	74
	B. Experiment	74
	C. Magnetoresistance Measurement	75
	D. 1/f Noise Measurement	76
	D.1 Quantitative Analysis of GOE-GUE Crossover	76
	D.2 Quantitative Analysis of Zeeman Crossover	77
	E. Earlier work	78
	References	80
5.	SPIN-FLIP SCATTERING and UCF	90
	A. Introduction	90
	B. Experiment	91
	C Weak localization	91
	D 1/f noise and UCF	93
	D.1 Orbital effect on UCF	93
	D.2 Spin effect on UCF	96
	E. Summary	97
	References	99
6.	CONCLUSIONS	108
7.	APPENDIX	110
	1/f noise	110

LIST OF TABLES

Table 1.1

The relative amplitude of universal conductance fluctuations in various regimes determined by an applied magnetic field and spin-orbit scattering rate.

Table 3.1

The procedure for trilayer electron-beam lithography to make sub-micron metal stencil.

Table 3.2

The procedure for bilayer optical lithography.

Table 3.3

The characteristics of samples are summarized.

Table 3.4

An assembly code used for real-time signal processing in the implementation of a dual-channel digital lock-in amplifier.

Table 5.1

The parameters of metallic lithium Samples studied for quantum transport.

LIST OF FIGURES

Chapter 2

Figure 2.1

- (a) Evaluation of the one-dimensional (1D) field correlation by Beenakker and von Houton.
- (b) Evaluation of the 1D variance and 1/f noise crossover function in the particle-particle channel.

Figure 2.2

Evaluation of the 1D 1/f noise crossover as a function of magnetic field in the particle-particle channel at different values of L_{ϕ} .

Figure 2.3

- (a) Evaluation of the 1D variance crossover in the particle-hole channel.
- (b) Evaluation of the 1D 1/f noise crossover in the particle-hole channel.

Figure 2.4

Evaluation of the 1D noise crossover function in the particle-hole channel for the low-temperature and high-temperature limit.

Figure 2.5

Evaluation of the particle-hole channel noise crossover function in 2D with different spin-orbit scattering rate.

Chapter 3

Figure 3.1

(a). Schematic set-up for the quench-condensation with a cryo-evaporator inside the vacuum-can.

(b). Schematic view of the substrate with a metal stencil for *in-situ* measurement.

Figure 3.2

Plot of line width versus line dose obtained by electron-beam lithography.

Figure 3.3

Scanning electron microscope (SEM) photograph of the bilayer electron-beam resist pattern just after it is developed.

Figure 3.4

- (a). SEM photograph of the undercut profiles and line resolutions obtained in the ~400 nm thick bilayer system.
- (b). SEM photo which shows the \sim 80 nm deep undercut profile of the bilayer resist exposed by the line dose.

Figure 3.5

SEM photo which shows the ~100 nm deep undercut profile of the bilayer resist exposed by area dose, 225 μ C/cm².

Figure 3.6

Schematic procedure for trilayer electron beam lithography.

Figure 3.7

- (a). SEM photograph of the top view of a sub-micron metal stencil
- (b) SEM photograph of the side view of a sub-micron metal stencil on top of the copolymer resist.

Figure 3.8

Schematic diagram of the sample geometry.

Figure 3.9

Schematic set-up of the noise measurement using the Motorola Digital Signal Processing(DSP) boards and personal computer.

Figure 3.10

Block diagram for the digital signal processing of the input signal.

Figure 3.11

Transfer functions of the three Chevychev FIR digital filters used in the implementation of a digital lock-in amplifier.

Figure 3.12

Recovery of the small 1/f noise signal out of the large background.

Chapter 4

Figure 4.1

Sample resistance versus temperature obtained from one-dimensional metallic Li wire.

Figure 4.2

1/f noise power spectrum and background Johnson noise obtained simultaneously by two-phase digital lock-in amplifier.

Figure 4.3

Magnetoresistance data at temperature, T = 1.6 K, 2.8 K, 4.0 K and 5.6 K. The solid line is the fit to the quasi-1D weak-localization theory with zero spin-orbit scattering.

Figure 4.4

The values of $\chi 2$ in the fit of the magnetoresistance data at 1.6 K with respect to different spin-orbit scattering rate.

Figure 4.5

The electron phase breaking length versus temperature, obtained from the weak-localization fits of low-field magnetoresistance.

Figure 4.6

The resistance noise power spectra, $S_R(f)$, versus frequency at 1.6 K with fits to a power law, at three values of magnetic field, B = 0 T, 1.0 T and 8.8 T.

Figure 4.7

Conductance noise power, $S_G(0.1 \text{ Hz})$, as a function of magnetic field at 1.6 K and 4.2 K. The data are normalized by the noise power at zero field. The solid line is the theoretical expression for the noise crossover function.

Figure 4.8

Contribution of % UCF to the total noise versus L_{ϕ}/l_{e} .

Chapter 5

Figure 5.1

- (a) Magnetoresistance of quasi-1D Li sample #1 (W = 0.11 μ m, R_{\square} = 5.7 Ω) taken at T = 2 K. The solid line is the fit to the quasi-1D weak localization theory.
- (b) Magnetoresistance of 2D Li sample #3 (W = 205 μ m, R_{\square} = 7.8 Ω) taken at T = 3.5 K. The solid line is the fit to the 2D weak localization theory.

Figure 5.2

The electron phase breaking length versus temperature, obtained from the weak-localization fits of low field magnetoresistance (a) for quasi-1D wires and (b) for 2D films.

Figure 5.3

Conductance noise power as a function of the perpendicular magnetic field below 1T, normalized by its zero-field value (a) for sample #1 and (b) for sample #2.

Figure 5.4

Values of the phase breaking length, obtained from the fits to the data of noise vs magnetic field in figure 5.3, and obtained from the magnetoresistance data in figure 5.2.

Figure 5.5

Noise power as a function of magnetic field up to 9T from sample #1 at temperatures 1.6 K and 4.2 K. (The data are normalized by the noise power at zero-field.)

Figure 5.6

Noise power as a function of magnetic field up to 9T from sample #2 at temperatures 1.6 K, 4.2 K and 10 K. (The data are normalized by the noise power at zero-field.)

Figure 5.7

A fit to the noise power as a function of magnetic field from sample #1 at temperatures 1.6 K and 4.2 K.

Appendix

Figure A

- (a) Temporal representation of Johnson noise.
- (b) Temporal representation of 1/f noise.

Chapter 1

INTRODUCTION

A. Classical Drude conductivity and Quantum correction.

How can we understand the low-temperature electronic conduction in a metal such as gold? Until recently it was generally accepted that at sufficiently low temperature, the conductivity of a metal is dominated by the residual scattering by impurities and is given by the classical Drude formula,

$$\sigma = \frac{ne^2\tau}{m} \tag{1-1}$$

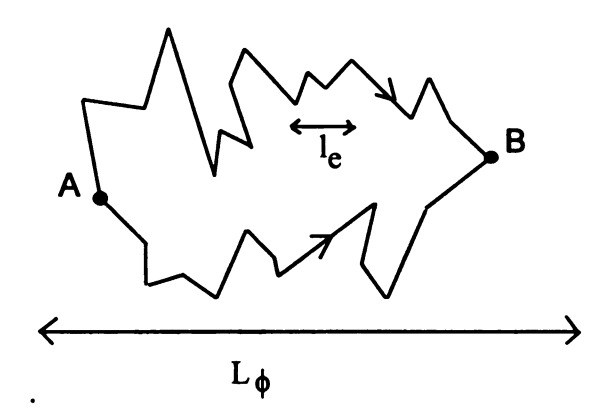
where τ is the elastic scattering time, related to the elastic mean free path $l_e = v_F \tau$. This model predicts that at low temperature, the resistance of a metal will reach a constant value determined by the concentration of static impurities.

Extensive theoretical and experimental studies showed that the effect of disorder on the electron transport is more dramatic than the classical transport estimated.[1] If the disorder is strong then electron wavefunctions can become localized, leading to a metal-insulator transition. Even in the weak disorder limit -- i.e. the good metallic regime, the deviation from Eq. (1-1) is significant. The resistance of thin films and wires increases above the residual value and continues to increase as the temperature is decreased.

These deviations in disordered metals can be understood in a new view of lowtemperature electron transport. Electrons are quantum mechanical waves and the conductance is given by the quantum mechanical transmission through scattering centers.[2] This remarkable idea led a number of groups to fabricate small wires and films and study their conductivity at low temperature. These efforts resulted in the discovery of novel phenomena -- weak localization and universal conductance fluctuations. Nowadays the quantum corrections to the classical Drude conductivity are well established in the low-temperature electron transport of disordered systems.

B. conductance as quantum transmission

The most intuitive explanation of quantum transport is based on Feynman's formulation of quantum mechanics; a particle propagates between two points via all possible paths. The picture below shows two typical paths between points $\bf A$ and $\bf B$. Each step along the path is determined by randomly located elastic scatterers due to the disorder and these elastic scatterers determine the electron mean free path, l_e . In disordered metals, at sufficiently low temperature, the electron transport is in the diffusive regime. The electrons diffuse coherently over a distance called the phase breaking length, $\bf L_{\phi}$, which can be much longer than the elastic mean free path.



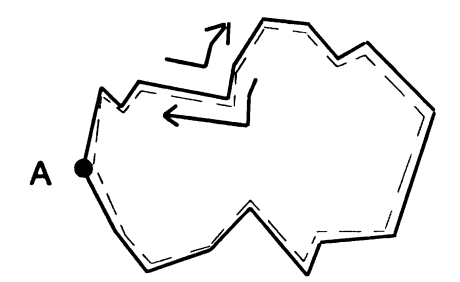
The elastic collisions with impurities do not destroy the phase information but shift the phase by some fixed amount. The different paths arrive at point **B** with different phases. The probability amplitude that an electron is transmitted from one side of the sample to the other is proportional to the sum of the amplitudes of Feynman paths that walk randomly across the sample. The transmission coefficient T is

$$T \propto \left| \sum_{\alpha} e^{i\phi_{\alpha}} \right|^2 \tag{1-2}$$

where α represents spatial path.[3] The cross terms in Eq. (1-2) correspond to the interference between paths, and lead to significant deviations from the classical Boltzman diffusion.

C. Weak-localization[4]

Consider the special paths that return to the origin as shown below.



There is always a time reversed path (dotted line) corresponding to a closed loop (solid line). These two paths will be in phase when they arrive at A because they are scattered by exactly the same elastic scattering centers. The interference between these two loops is always constructive and will enhance the probability of returning to the starting point A. The enhanced back-scattering decreases the diffusion constant and diminishes the conduction. This correction to the classical Drude conductivity is called "weak localization", and it depends on the amount of disorder but not on the details of the impurity configuration.

A dramatic effect of weak-localization occurs when a weak magnetic field is applied, in which case the theory predicts a negative magnetoresistance. This is a striking prediction because, in classical transport, a magnetic field pushes electrons transverse to the current direction and increases the resistance, resulting in a positive magnetoresistance. The classical magnetoresistance can be observed in relatively high fields. In weak-localization, the presence of a magnetic field perpendicular to a metallic film gives each Feynman path an additional phase factor $\frac{e}{\hbar} \int A \cdot dl$, where the line integral is along the trajectory. Since the path and its conjugate will pick up opposite phases in a magnetic field, the applied magnetic field destroys the coherent backscattering. Therefore, the resistivity will decrease as the magnetic field increases, leading to a negative magnetoresistance.

D. Universal Conductance Fluctuations[5]

An interesting question is what happens when we consider interference between all the paths. In small structures, mesoscopic systems, with dimensions on the order of the phase coherence length, the transmission coefficient has a *sample-specific* value that depends on the detailed location of the scattering centers. The transmission depends sensitively on perturbations such as rearrangement of scatterers, magnetic field and chemical potential, leading to chaotic fluctuations of conductance. This is the phenomenum called universal conductance fluctuations. In contrast to weak localization, universal conductance fluctuations (UCF) average to zero in large samples (the ensemble average).

D1. Universality of fluctuation amplitude.

The amplitude of UCF has a remarkable universality: the conductance of a metallic sample fluctuates by order e^2/h (\approx 4E-5 mho), independent of degree of disorder and

sample size (L) as long as $L < L_{\phi}$.[6] This universality is a key result in mesoscopic physics.

The universality of conductance fluctuations can be understood following several approaches. One approach is based on the microscopic theory using the impurity-averaged Green's function technique.[7,13,14] An alternative approach is built on the basis of Landauer's definition of conductance -- the conductance is related to the eigenvalues of the transmission matrix.[8] The eigenvalues obey the level repulsion property of the appropriate random matrix ensemble introduced by Wigner and Dyson: Gaussian orthogonal ensemble (GOE) for a system with time-reversal and spin symmetry, Gaussian unitary ensemble (GUE) when time-reversal symmetry is broken, and Gaussian sympletic ensemble (GSE) in the limit of strong spin-orbit scattering.[9] This random matrix approach provides the more fundamental understanding of the universal conductance fluctuations and gives a simple way to predict the relative amplitude of the UCF. The theoretical result is:

$$(\delta G)^2 \approx \frac{1}{4} \left(\frac{e^2}{h}\right)^2 \frac{ks^2}{\beta} \tag{1-3}$$

where k is the number of independent eigenvalue sequences, s is the eigenvalue degeneracy, and $\beta = 1,2$, or 4 for the GOE, GUE or GSE, respectively.

Experimental establishment of the different ensembles can be shown with application of magnetic field and spin-orbit scattering. Application of a weak magnetic field breaks the time-reversal symmetry of the electron orbital motion and a strong magnetic field lifts the electron spin symmetry due to Zeeman splitting. Strong spin-orbit scattering breaks the spin-rotation symmetry. The relative amplitude of fluctuations in various regimes determined by an applied magnetic field and spin-orbit scattering are summarized in Table 1-1. The characteristic field scales

involved in these symmetry breakings are denoted as B_{c1} and B_{c2} . (The field strength for B_{c1} and B_{c2} will be discussed later)

D2. UCF noise reduction induced by magnetic field.

Experimental verification of the UCF amplitude given by Eq. (1-3) can be achieved by measuring and comparing $(\delta G)^2$ in the different random matrix ensembles determined by the magnetic field. Measurement of $(\delta G)^2$ in a single sample requires that we vary some parameter to obtain different values of G in the ensemble. The usual method of measuring the static variation of G versus magnetic field (the "magnetofingerprint") is inadequate because we like to obtain $(\delta G)^2$ at fixed values of magnetic field. Fortunately, in disordered metals, impurities and scattering centers rearrange themselves spontaneously even at low temperature due to tunneling. The rearrangement of impurities gives rise to 1/f noise in the electrical resistance.[10] The noise measurement provides a tool to study $(\delta G)^2$ with excellent statistics at fixed magnetic field; the accuracy of the measurement increases with the measurement time. A further discussion of 1/f noise is given in the appendix.

Experiments pursuing the ratio of the UCF amplitude between the random matrix ensembles have been reported for several special cases. For the strong spin-orbit scattering case, Birge *et al.* studied the 1/f noise as a function of magnetic field in 2D films of Bi and clearly observed that UCF noise is reduced to half of the zero field value with a characteristic field scale determined by one-flux quantum(h/e) through a phase coherent area.[11] This reduction corresponds to the crossover from symplectic to unitary ensemble in the quantum transport with simultaneously breaking of the Kramers degeneracy. Measurements in the weak spin-orbit scattering limit, however, have been less clear. Debray et.al measured time-independent conductance fluctuations in a MOSFET as a function of gate voltage at several values of magnetic field at 1.3 K.[12] A reduction of the variance, $(\delta G)^2$, by a factor of 4 was observed

at ~0.7 kG. The authors attributed this reduction to the Zeeman effect with the characteristic field scale determined by the Thouless energy, $E_c = \hbar D/L_{\phi}^2$. It was not clear, however, whether B_{c2} is really determined by the Thouless energy because the value of the g-factor was not known in their MOSFET. In addition, theoretical arguments about the energy scale for the Zeeman crossover on UCF have been contradictory.[13,14] A second limitation of the MOSFET experiment is that the low field data were in the limit of either GOE or GUE --only one data point near the first reduction is shown and there were no data showing the crossover between those ensembles.

We studied universal conductance fluctuations in the low spin-orbit limit by measuring the 1/f resistance noise in a quasi-1D lithium wire fabricated by quench-condensation at 4.2 K. From the magnetoresistance, we confirm the low spin-dependent (spin-orbit or spin-flip) scattering in out Li wire; the upper bound of spin-orbit scattering rate is estimated to be $5\sim10$ times smaller than the phase breaking rate. At temperatures of 1.6 and 4.2 K, we observe that the noise is reduced *twice* as a function of magnetic field. The first drop occurs below 0.01 T and the second reduction occurs above 1 T. We calculate the theoretical crossover function for both drops and compare with the experimental data. The experimental data are fully consistent with the theory for the complete crossover function both for the GOE to GUE transition[15] and for the splitting of the Zeeman degeneracy[14]. Our results show that the characteristic field scale for the Zeeman crossover is determined by the sample temperature rather than the pre-assumed Thouless energy for the case $k_BT \gg E_C$.

References

- [1] For a reviews of this subject, see P. A. Lee and T. V. Ramakrishnan, Rev. Mod. Phys. 57, 287 (1985).
- [2] R. Landauer, Phil. Mag. 21, 863 (1970).
- [3] D. S. Fisher and P. A. Lee, Phys. Rev. B23, 6851 (1981).
- [4] see G. Bergmann, Phys. Rep. 107, 1 (1984).
- [5] Mesoscopic Phenomena in solids, edited by B. L. Al'tshuler, P. A. Lee, and R. A. Webb (North-Holland, New York, 1991).
- [6] B. L. Al'tshuler, Pis'ma Zh. Eksp. Teor. Fiz. 41, 530 (1985) [JEPT Lett. 41, 648 (1985)]; P. A. Lee and A. D. Stone, Phys. Rev. Lett. 55,1622 (1985).
- [7] P. A. Lee, A. D. Stone, and H. Fukuyama, Phys. Rev. B 35, 1039 (1987); S. Feng, Phys. Rev. B 39, 8722 (1989).
- [8] Y. Imry, Europhys. Lett. 1, 249 (1986); B. L. Al'tshuler and B. I. Shklovskii, Zh. Eksp. Teor. Fiz. 91, 220 (1986) [Sov. Phys. JETP 64, 127 (1986)]; P. A. Mello, Phys. Rev. Lett. 60,1089 (1988); K. A. Muttalib, J.-L. Pichard, and A. D. Stone, Phys. Rev. Lett. 59, 2475 (1987).
- [9] For a review of random matrix theory, see T. A. Brody et al., Rev. Mod. Phys. 53, 385 (1981).
- [10] S. Feng, P. A. Lee, A. D. Stone, Phys. Rev. Lett. 56, 1960 (1986).
- [11] N. O. Birge, B. Golding, and W. H. Haemmerle, Phys. Rev. Lett. 62, 195 (1989).
- [12] P. Debray, J.-L. Pichard, J. Vicente, P. N. Tung, Phys. Rev. Lett. 63, 2264 (1989).
- [13] A. D. Stone, Phys. Rev. B 39, 10736 (1989).
- [14] S. Feng, Phys. Rev. B 39, 8722 (1989).
- [15] The quasi-1D noise crossover function between GOE and GUE is derived from the field correlation, $\langle G(B)G(B+\Delta B)\rangle$.

Table 1.1: g is defined as $G/(e^2/h)$.

	B< <b<sub>c1</b<sub>	B _{c1} < <b<<b<sub>c2</b<<b<sub>	B>>B _{c2}
weak spin-orbit	$(\delta g)^2 \equiv 1$	$(\delta g)^2 \equiv 1/2$	$(\delta g)^2 \equiv 1/4$
limit	$\beta=1, k=1, s=2$	$\beta=2, k=1, s=2$	β=2, <i>k</i> =2, <i>s</i> =1
strong spin-orbit	$(\delta g)^2 \equiv 1/4$	$(\delta g)^2 \equiv 1/8$	$(\delta g)^2 \equiv 1/8$
limit	β =4, k =1, s =2	$\beta=2, k=1, s=1$	$\beta=2, k=1, s=1$

Chapter 2

THEORY OF QUANTUM TRANSPORT

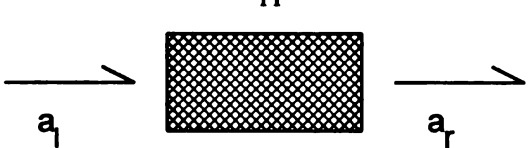
This chapter describes the theoretical background necessary to understand our experiments. In the first half, we explain the important concept of diffusive quantum transport in disordered metals, and its connection to random matrix theory. In the second half, we summarize the previous quantitative calculations of the amplitude of UCF and the UCF crossover functions between random matrix ensembles. In addition, we present our quantitative formulation of the UCF crossover and its evaluation, which is used in the data analysis.

2A. Diffusive quantum transport in metals

In disordered metals, at sufficiently low temperature, the electrons diffuse coherently through the disordered medium over a distance called the phase breaking length, L_{ϕ} . One can think of the electron motion as a random walk where the step distance is the elastic mean free path. When the sample size L is much longer than elastic mean free path, we call the transport "diffusive".

2B. Landauer's conductance[1]

Landauer considered the electrical conduction of a sample connected to two ideal probes, and showed that the conductance G is related to the transmission probability of electrons through the sample. Consider a coherent box of length less than L_{ϕ} and of transverse dimensions W. The number of quantized transverse momentum states within the probes is $N_c \approx (Wk_F)^{d-1}$ in dimension d.



The $\mathbf{a_l}$ is the incident flux from the left and the $\mathbf{a_r}$ is the transmitted flux through the scattering medium. The transmission matrix \mathbf{t} of the scattering medium can be defined as $\mathbf{a_r} = \mathbf{ta_l}$ where \mathbf{t} is a $N_c \times N_c$ matrix. Denoting the transmission amplitude between the channels i and j by t_{ij} in a transmission matrix \mathbf{t} , the conductance G is given by

$$G = 2(e^2/h) \operatorname{Tr} (\mathbf{t} \mathbf{t}^*) = 2(e^2/h) \sum_{i,j}^{N_C} |t_{ij}|^2$$
 (2-1)

where the factor of 2 is due to electron spin degeneracy.

2C. Universal Conductance Fluctuations

The quantum interference among diffusive paths gives rise to extreme sensitivity of the transmission probability to the detailed configuration of the microscopic scattering centers, leading to sample-specific transmission values. The resulting fluctuations of the conductance is a phenomenon called "universal conductance fluctuations" (UCF), where the conductance fluctuates as a function of a control parameter by a universal amplitude of order e^2/h (\approx 4E-5 mho), independent of disorder and sample size (L) as long as $L < L_{\phi}$

$$\delta G \approx e^2/h$$
 (2-2)

So, UCF is most evident in a small sample or mesoscopic system with size comparable to the phase breaking length and this remarkable universality stands out as the key result in the mesoscopic physics.

The universality of conductance fluctuations can be understood following several approaches. The original approach[2], by Al'tshuler and by Lee and Stone, is based on the microscopic theory using impurity-averaged Green's function technique. Alternative approaches are built on the statistical properties of the eigenvalues of either the random Hamiltonian[3] or random scattering matrix[4]. The second approaches provide the more intuitive understanding of the universal conductance fluctuations.

2C.1 Random matrix approach

Random matrix theory by Wigner and Dyson[5,6]

Wigner and Dyson introduced the universal random matrix ensembles to describe the statistics of nuclear energy levels. The Gaussian orthogonal ensemble describes systems with time-reversal symmetry and spin symmetry, the Gaussian unitary ensemble is appropriate when time-reversal symmetry is broken, while the Gaussian sympletic ensemble describes the case of broken spin-symmetry. Wigner and Dyson found that the level statistics depend on the symmetries of the ensemble, independent of the microscopic details of the system.

• Random matrix theory in UCF

Consider the conductance of a metal which is connected to two ideal leads of size W in dimension d. The sample length is L. The dimensionless conductance per spin channel, $g=G/(e^2/h)$, is given by the transmission matrix of the conductor as mentioned before, Eq. (2-1),

$$G = (e^2/h) \text{Tr} (\mathbf{tt}^*) = (e^2/h) \sum_{i,j}^{N_C} |t_{ij}|^2$$

where, i and j are channel indices.

It is interesting to see how Landauer's approach can be connected to random matrix theory[4]. Consider a scattering medium with incident flux $\{I_l, I_r\}$ and corresponding transmitted flux $\{O_l, O_r\}$.

The reflection and transmission matrices \mathbf{r} and \mathbf{t} are $N_c \times N_c$ matrices, where N_c is the number of propagation channels at the Fermi energy. The scattering property of a sample or scattering medium is described by either the scattering matrix \mathbf{S} or the transfer matrix \mathbf{T} as following

$$\mathbf{S}\begin{bmatrix} \mathbf{I}_{\mathbf{l}} \\ \mathbf{I}_{\mathbf{r}} \end{bmatrix} = \begin{bmatrix} \mathbf{O}_{\mathbf{r}} \\ \mathbf{O}_{\mathbf{l}} \end{bmatrix} \quad , \quad \mathbf{T}\begin{bmatrix} \mathbf{I}_{\mathbf{l}} \\ \mathbf{O}_{\mathbf{l}} \end{bmatrix} = \begin{bmatrix} \mathbf{O}_{\mathbf{r}} \\ \mathbf{I}_{\mathbf{r}} \end{bmatrix}$$
 (2-3)

Following simple algebra with r and t, the conductance is given by

$$g = Tr(tt^*) = Tr(\frac{2}{TT^* + (TT^*)^{-1} + 2I})$$
 (2-4)

This trace of the transfer matrix can be rewritten in terms of the eigenvalues of a random matrix in the following way:

$$g = \sum_{i=1}^{N_c} \frac{1}{1+\lambda_i} \tag{2-5}$$

where λ_i are the eigenvalues of the matrix, $\mathbf{X} = [(\mathbf{TT}^* + (\mathbf{TT}^*)^{-1} - 2\mathbf{I}]/4$.

Eq. (2-5) implies that the conductance is a "linear statistic" of eigenvalues λ_i (The word "linear statistic" means that the conductance does not contain products of the eigenvalues, but the functional dependence can be non-linear). The distribution of the eigenvalues is given by [9],

$$P(\{\lambda_n\}) \approx \exp[-\beta H(\{\lambda_n\})],$$

$$H(\{\lambda_n\}) = -\sum_{i < j} \ln |\lambda_i - \lambda_j| + \sum_i V(\lambda_i)$$
(2-6)

where, the number β is different for each of the three ensembles of random matrix; β is equal to 1,2 and 4 for the Gaussian orthogonal, Gaussian unitary and Gaussian sympletic ensembles respectively. The probability distribution has the form of a Gibbs distribution, with the symmetry parameter β playing the role of the temperature, and the H containing the logarithmic repulsive interaction between eigenvalues in addition to a "potential" V. Since the conductance is a linear statistic of the eigenvalues, its variance is given by [10]

$$Var(g) = \int_{0}^{\infty} d\lambda \int_{0}^{\infty} d\lambda' \frac{1}{1+\lambda} \frac{1}{1+\lambda'} K_2(\lambda, \lambda')$$
 (2-7)

Here, the two-point correlation function $K_2(\lambda, \lambda')$ is defined by

$$K_{2}(\lambda, \lambda') = \langle \rho(\lambda)\rho(\lambda')\rangle - \langle \rho(\lambda)\rangle\langle \rho(\lambda')\rangle \tag{2-8}$$

where $\rho(\lambda) = \sum_{n} \delta(\lambda - \lambda_n)$ is the eigenvalue density. As long as the correlation function $K_2(\lambda, \lambda')$ is known, the variance of the linear statistic can be calculated in a

straightforward manner. For the distribution of the eigenvalues in Eq. (2-6), the mean density of transmission eigenvalues $\langle \rho(\lambda) \rangle$ is

$$\langle \rho(\lambda) \rangle = \frac{\int d\lambda_1 \cdots \int d\lambda_N \rho(\lambda; \lambda_1 \cdots \lambda_N) \exp(-\beta H)}{\int d\lambda_1 \cdots \int d\lambda_N \exp(-\beta H)}$$
(2-9)

Differentiation of Eq. (2-9) with respect to $V(\lambda')$ yields

$$\frac{\delta\langle\rho(\lambda)\rangle}{\delta V(\lambda')} = -\beta\langle\rho(\lambda)\rho(\lambda')\rangle + \beta\langle\rho(\lambda)\rangle\langle\rho(\lambda')\rangle \tag{2-10}$$

Eq. (2-8) and (2-10) give $K_2(\lambda, \lambda') = \frac{1}{\beta} \frac{\delta \langle \rho(\lambda) \rangle}{\delta V(\lambda')}$. Then, Eq. (2-7) yields $Var(g) \propto 1/\beta$, if there is a linear relationship between $\rho(\lambda)$ and the "potential" V. This relation has been addressed by Dyson[11] and found to be linear as a consequence of the distribution function Eq. (2-6). Therefore, the variance is independent of the microscopic details of system and has a universal dependence on the symmetry constraint β . The full expression, i.e. Eq. (1-3), of conductance fluctuations probably can be derived by taking the degeneracy of eigenvalue into account, although no calculations with the degeneracy have been reported following the random scattering matrix approach.

2C.2 Random Hamiltonian approach.

Even though the conductance should be viewed in terms of quantum diffusion, it is heuristically interesting to consider the approach following the Thouless argument[12]. In a hypercube of size L, the electronic eigenstates are determined by the microscopic Hamiltonian. From the uncertainty principle, such eigenstates are associated with a width, $E_c = \hbar/\tau = \hbar D/L^2$ where τ is the time to diffuse through

the sample. Assuming there is an average energy level spacing ΔE , the conductance G is given by

$$G = \frac{e^2}{h} \cdot \frac{E_c}{\Lambda E} = \frac{e^2}{h} \cdot N(E_c)$$
 (2-11)

 $N(E_c)$ is the number of energy levels within an energy range E_c . If the energy levels are randomly distributed (Poisson distribution), one would expect fluctuations $\delta N \approx \sqrt{N}$ which results in $\delta G \approx \frac{e^2}{h} \cdot \sqrt{N(E_c)}$, which is the wrong answer. The amplitude of conductance fluctuations from this point of view are much stronger than the real fluctuations in Eq. (2-2). The fact that the level number fluctuations for a given energy band must be small compared to \sqrt{N} indicates a repulsion between the energy levels. Dyson[6] showed that in a closed system the level repulsion gives

$$\langle [\delta N(E)]^2 \rangle \approx \frac{1}{4} \frac{k \cdot s^2}{\beta} \ln \langle N(E) \rangle$$
 (2-12)

where, β is equal to 1,2 and 4 for the Gaussian orthogonal, Gaussian unitary and Gaussian sympletic ensembles respectively. The quantity k is equal to the number of the non-interacting series of levels; indeed, levels with different precisely defined quantum numbers do not interact with one-another. The quantity s is the degeneracy factor. Thus, the amplitude of fluctuations depends on β , s, and k. Later, Al'tshuler and Shklovskii[3] showed that in a system connected to the outside with ideal probes,

$$\langle [\delta N(E)]^2 \rangle \approx \frac{1}{4} \frac{k \cdot s^2}{\beta}$$
 (2-13)

which is consistent with Eq. (2-2) and directly gives Eq. (1-3).

2.C.3 Diagrammatic approach

The microscopic theory of UCF has been formulated on the basis of impurity-averaged Green function techniques with $k_F l_e$ as a perturbation parameter. This complicated calculation provides a quantitative description of UCF including the UCF crossover functions between the different random matrix ensembles. Also, the effect of finite temperature can be handled quantitatively.

Within the diagrammatic calculation, the amplitude of UCF stems from two channels which contribute equally at zero magnetic field: the cooper (particle-particle) and diffuson (particle-hole) channel. Quantitative understanding of the UCF crossover function requires the proper handling of such channels with respect to magnetic field and spin-orbit scattering. There are several calculations reported. Lee, Stone and Fukuyama[8] first pointed out some of the UCF reduction factors, and Feng[13] calculated the UCF reductions in the presence of spin-orbit scattering and the Zeeman effect. Stone[14] presented the calculation on the UCF noise crossover. Chandrasekhar et.al.[15] discussed the effect of spin-dependent scattering on UCF.

A simple way to look at various UCF reduction factors is to describe the amplitude of UCF in terms of the spin variables of the channels. The spin variables are total spin J and its projection M_z , of electron and hole for the diffuson channel, and of electron and electron for the cooper channel. We can re-write each channel in terms of spin-singlet (J=0, M=0) and spin-triplet (J=1, M= \pm 1,0) terms. The conductance variance is given by:

$$(\delta G)^{2} = \frac{1}{2} \left[\frac{1}{4} (\delta G_{s}(B)^{2} + \frac{3}{4} (\delta G_{t}(B, L_{so}))^{2}) \right]_{pp} + \frac{1}{2} \left[\frac{1}{4} (\delta G_{s})^{2} + \frac{3}{4} (\delta G_{t}(g\mu_{B}B, L_{so}))^{2} \right]_{ph}$$

where G_s and G_t stand for the conductance of singlet and triplet part respectively. Also, the pp and ph mean the particle-particle and the particle-hole channel, respectively. Strong spin-orbit scattering $(L_{so} \rightarrow 0)$ suppresses the triplet contribution in both channels, leading to a factor of 4 reduction in UCF. The effect of magnetic field comes from an orbital effect in the cooperon channel and spin effect in the diffuson channel. An application of weak magnetic field suppresses the B-dependent cooper channel (both singlet and triplet), and reduces UCF by factor of 2, whether the spin-orbit scattering is strong or not. The effect of Zeeman splitting can be observed due to the suppression of the M_z =±1 triplet parts in the diffuson channel only if the spin-orbit scattering is weak.

2.C.4 The Amplitude of UCF.

The theoretical approaches have shown that the amplitude of UCF depends on the statistical properties of the random matrix ensembles which can be varied experimentally by application of magnetic field and spin-orbit scattering. The predicted reduction factors are summarized in Eq. (1-3) as:

$$(\delta g)^2 \approx \frac{1}{4} \frac{k \cdot s^2}{\beta}$$

and are summarized in Table 1-1. The β represents the random matrix ensemble characterized by time-reversal and spin symmetry. The degeneracy s stems from the electron spin symmetry in the weak spin-orbit scattering regime, and from the Kramers degeneracy in the strong spin-orbit scattering regime. The k is the number of statistically independent channels. The characteristic field scales involved in the crossover between different regimes are denoted as B_{c1} and B_{c2} .

Here we repeat the Table 1-1 for convenience.

Table 1-1: g is defined as $G/(e^2/h)$.

	B< <b<sub>c1</b<sub>	B _{c1} < <b<<b<sub>c2</b<<b<sub>	B>>B _{c2}
weak spin-orbit	$(\delta g)^2 \equiv 1$	$(\delta g)^2 \equiv 1/2$	$(\delta g)^2 \equiv 1/4$
limit	$\beta=1, k=1, s=2$	$\beta=2, k=1, s=2$	$\beta=2, k=2, s=1$
strong spin-orbit	$(\delta g)^2 \equiv 1/4$	$(\delta g)^2 \equiv 1/8$	$(\delta g)^2 \equiv 1/8$
limit	$\beta=4, k=1, s=2$	$\beta=2, k=1, s=1$	$\beta=2, k=1, s=1$

2D. Quantitative Analysis of UCF

First, the mathematical definition of important quantities related to UCF (for example, field correlation, variance, and noise) are introduced. Since our experiment focused on the relative amplitude of UCF as a function of the external magnetic field, the theoretical derivation and evaluation of the UCF crossover functions is presented.

2D.1 Field correlation, Variance and UCF noise

Field correlation and Variance[8]

UCF theory is based on the ergodic hypothesis — ensemble averaging of the conductance is equivalent to averaging the conductance of a single sample over magnetic field, or over the Fermi energy in a semiconductor. Changing the Fermi energy or magnetic field randomizes the phases of electrons, leading to chaotic variation of the conductance. If one changes the field or Fermi energy enough so that the phases of electrons are totally uncorrelated with those at the original value of the field or energy, then the sample acts as a new sample in the measurement of conductance. The correlation function of conductance with respect to the variation of the field or the energy, $F(\Delta E, \Delta B)$, can be defined by,

$$F(\Delta E, \Delta B, B) = \langle \delta g(E_F, B) \delta g(E_F + \Delta E, B + \Delta B) \rangle$$
 (2-15)

where $\delta g = g(E_F, B) - \langle g(E_F, B) \rangle$. The angular bracket $\langle \rangle$ means an ensemble average. The variance of conductance is given by,

$$Var(g) = \langle (\delta g)^2 \rangle = \langle (g - \langle g \rangle)^2 \rangle$$
 (2-16)

The correlation function with $\Delta E = \Delta B = 0$ gives the variance.

At finite temperature, conductance fluctuations are reduced by "classical averaging" once the temperature is high enough that the phase breaking length is shorter than the sample length. Also, thermal smearing of the Fermi surface reduces the amplitude of conductance fluctuations due to "thermal averaging" in which the length scale is the thermal diffusion length $L_T = \sqrt{\frac{\hbar D}{k_B T}}$. The formula for the field correlation F_T at finite T is given by

$$F_T(\Delta\mu, \Delta B, T) = \int dE_1 \int dE_2 f'(E_1, \mu) f'(E_2, \mu + \Delta\mu) \times \langle \delta g(E_1, B) \delta g(E_2, B + \Delta B) \rangle$$
(2-17)

$$= \int d\Delta E K(\Delta E, \Delta \mu) F_0(|\Delta E|, \Delta B),$$

where $f' = \frac{df}{dE}$, f is the Fermi distribution function, F_0 is the T=0 correlation function defined by Eq. (2-15) and $K(\Delta E, \Delta \mu)$ is the convolution integral

$$K(\Delta E, \Delta \mu) = \int dE_1 f'(E_1, \mu) f'(E_1 - \Delta E, \mu + \Delta \mu)$$

The variance of g is

$$Var[g(B,T)] = \frac{4s^2}{\pi^2} \int \frac{d\Delta E}{2k_B T} K(\frac{\Delta E}{2k_B T}) F_0(\Delta E, B)$$
 (2-18)

where $K(x) = (x \coth x - 1) / \sinh^2(x)$ and s is the spin degeneracy.

UCF Noise

Since UCF arises from the interference of the electron waves scattered from the defects or impurities, a change of the random scattering potential yields fluctuations in conductance $(\delta g')^2$ or noise. (A brief discussion of the noise spectrum is given in the appendix.) Denoting the random impurity potentials of many impurities by $V(\mathbf{r})$ and $V'(\mathbf{r}')$, the noise at magnetic field B and temperature T is given by:

$$[\delta g'(B,T)]^2 = \langle [g(B,T,V) - g(B,T,V')]^2 \rangle$$

$$= 2\{Var[g(B,T)] - \langle \delta g(B,T,V) \delta g(B,T,V') \rangle \} \quad (2-19)$$

The sensitivity of UCF to a change of the random scattering potentials was calculated by Feng, Lee, and Stone[16] and by Al'tshuler and Spivak[17]. The conductance change, δg_1 , of a coherent volume due to a single impurity movement by a distance δr is:

$$(\delta g_1)^2 \sim \frac{1}{(k_F l_e)^{d-1}} (\frac{l_e}{L})^{d-2} \alpha(k_F \delta r)$$
 (2-20)

where $\alpha(k_F\delta r)$ is the phase shift that the electron experiences due to a single impurity motion, and $\alpha(k_F\delta r)$ approaches unity for $\delta r >> k_F^{-1}$. Surprisingly, a single impurity can cause saturation of the conductance fluctuations in the case of $k_F l_e = 1$, so the UCF noise shows extreme sensitivity to the motion of defects.

2D.2 Crossover function in particle-particle channel.

In this part, the derivation and evaluation of the UCF noise crossover functions in a quasi-1D sample will be discussed since we measured the 1/f noise in

quasi-1D samples. (See Chapter 4 & 5.) Stone[14] calculated the 1/f noise crossover function in 2D. To get the 1D crossover function, one approach is to modify Stone's 2D calculation. Instead, we used an alternative route in which the 1/f noise crossover function can be obtained starting with an analytical expression for the field autocorrelation of conductance, $F(\Delta B) = \langle g(B)g(B + \Delta B) \rangle$, given by Beenackker and von Houton[18].

2D.2.1 Method with field correlation function

overview

The amplitude of UCF stems from two channels which contribute equally: particle-particle and particle-hole channel. Lee et.al [8] showed that the magnetic field enters the UCF calculation by means of the semi-classical approximation for the Green function, $G(\mathbf{r},\mathbf{r}')$:

$$G(r,r',B) = \exp\left[\frac{2\pi i}{h/e} \int_{r'}^{r} \mathbf{A} \cdot dl\right] G(r,r')$$

Since the product of G(r,r')G(r',r) enters in the particle-hole channel, only ΔA appears in the diffusion equation and the correlation function $F^{ph}(\Delta B)$ is determined by the eigenvalues and eigenvectors of the diffusion equation[8]:

$$\tau(-i\Delta E + D(-i\nabla - e\Delta A)^2 + \tau_{\perp}^{-1})Q_{m}(r) = \lambda^{ph}Q_{m}(r)$$
 (2-21)

Whereas for the particle-particle channel, $(\Delta A + 2A)$ appears in the diffusion equation which determines $F^{pp}(B, \Delta B)$. The diffusion equation for the particle-particle channel is:

$$\tau (-i\Delta E + D(-i\nabla - e(2A + \Delta A))^{2} + \tau_{\perp}^{-1})Q_{m}(r) = \lambda^{pp}Q_{m}(r)$$
 (2-22)

The magnetic field correlation function is given by the sum of the two contributions, which are equal at B=0:

$$F(B, \Delta B) = F^{ph}(\Delta B) + F^{pp}(B, \Delta B) \tag{2-23}$$

The *B*-dependence of *F* comes from the particle-particle channel. (Here, we don't consider the Zeeman effect.) When there is magnetic flux larger than h/e (one flux quantum) in a coherent area of the sample, then $F^{pp} \to 0$ and $F(B,\Delta B) \approx F^{ph}(\Delta B)$, i.e. the variance drops by exactly a factor of two, i.e. $F(B >> B_{c1}, 0) \approx F^{ph}(0) = 1/2$ F(0,0).

Stone[14] pointed out that the crossover function for the variance of g is identical to the large field conductance correlation function $F^{ph}(\Delta B)$ if one makes the substitution $e\Delta B \rightarrow 2eB$. This can be checked from the diffusion equations Eq. (2-21) and (2-22). The cooperon contribution to the UCF variance at fixed field can be obtained from the diffusion Eq. (2-22) with $\Delta A = 0$. Compared to Eq.(2-21), the only difference in the diffusion equation is the substitution of ΔA into ΔA . Then

$$Var^{pp}(g:B) = F^{ph}(\Delta B \to 2B) \tag{2-24}$$

Al'tshuler and Spivak[16] showed that for small variations in the impurity potential V, and V, we get the noise function in the following way:

$$\left[\delta g'(B,T)\right]^2 \approx -2\gamma' \frac{d}{d(1/\tau_{\phi})} Var[g(B,T)] \tag{2-25}$$

where, $\gamma' = \left[1 - (\langle VV' \rangle / \langle V \rangle^2)\right] / \tau_{el}$. This is the case of unsaturated noise, i.e. $\delta g' <<$

1. The noise crossover function in the cooper channel is simply,

$$v^{pp}(B,T) = [\delta g'(B,T)]^2 / [\delta g'(B=0,T)]^2. \tag{2-26}$$

1D field correlation function

An analytical formula for the field correlation function for conductance in the diffusive regime was calculated by Beenakkar and von Houten[17], in the case of a quasi-1D geometry ($W \ll L_{\phi} \ll L$) where L and W are the length and width. The field correlation function is given by

$$F(\Delta B) \approx 6\left(\frac{e^2}{h}\right)^2 \frac{L_{\phi}^3}{L^3} \left(1 + \frac{9}{2\pi} \frac{L_{\phi}^2}{L_T^2}\right)^{-1}$$
 (2-27)

Here, the effect of magnetic field is corporated into $L_{\phi} = \sqrt{D\tau_{\phi}}$ with $D = v_f l_e / 3$ in the following way:

$$1/\tau_{\phi}(\Delta B) = 1/\tau_{\phi}(0) + 1/\tau_{\Delta B}$$

$$1/\tau_{\Delta B} = \frac{1}{3}D \times (\frac{\pi W \Delta B}{h/e})^2 \tag{2-28}$$

 L_T is the thermal length defined as $L_T = \sqrt{\frac{\hbar D}{k_B T}}$. From Eq. (2-24),

$$Var^{pp}(g:B) = F^{ph}(\Delta B \to 2B)$$

$$\approx 6(\frac{e^2}{h})^2 \frac{L_{\phi}^3(B)}{L^3} (1 + \frac{9}{2\pi} \frac{L_{\phi}^2(B)}{L_T^2})^{-1}$$
(2-29)

where

$$L_{\phi}^{-2}(B) = \frac{1}{L_{\phi}^{2}(0)} + \frac{1}{3} \left(\frac{\pi WB}{h/2e}\right)^{2}$$
 (2-30)

(Note the factor of 2 compared to Eq. (2-28).)

1D 1/f noise crossover function

The 1/f noise crossover function, $v^{pp}(B)$, in the cooper channel is calculated from Eq. (2-25) and (2-29):

$$\delta g^{\prime 2}(B,T) \approx L_{\phi}^{5}(B) \cdot \left(1 + \frac{9}{2\pi} \frac{L_{\phi}^{2}(B)}{L_{T}^{2}}\right)^{-1} \times \left[1 - \frac{3}{\pi} \frac{L_{\phi}^{2}(B)}{L_{T}^{2}} \left(1 + \frac{9}{2\pi} \frac{L_{\phi}^{2}(B)}{L_{T}^{2}}\right)^{-1}\right]$$
(2-31)

where the effect of magnetic field is incorporated into $L_{\phi}(B)$ using Eq. (2-30). The total noise is given by Cooperon and diffuson contributions that are equal at zero field, so the crossover function for the relative noise power at low magnetic field is:

$$v(B) = \frac{1}{2} \left(1 + \frac{\delta g'^2(B)}{\delta g'^2(0)} \right)$$
 (2-32)

Figure 2.1 shows the evaluation of the 1D field correlation, variance and 1/f noise crossover function. Here, we use $1\mu m$ for L_{ϕ} , 0.17 μm for L_{T} and 0.45 μm for the

sample width W. (These values are appropriate for the sample in Chapter 4 at T = 1.6 K.)

2D.2.2 Method by Stone[14]

Stone showed that the T=0 energy correlation function $F_0(\Delta E, B)$ is given by

$$F_0(\Delta E, B) = \sum_{\alpha} \left[\frac{1}{\left| \lambda_{\alpha}^{pp} \right|^2} + \frac{1}{2} \operatorname{Re}(\frac{1}{\lambda_{\alpha}^{pp^2}}) \right]$$
 (2-33)

where, λ^{pp}_{α} are the eigenvalues of the differential equation,

$$(-i\Delta E/\hbar + D(-i\nabla - 2eA)^2 + \tau_{\phi}^{-1})Q_{\alpha}(r) = \lambda_{\alpha}^{pp}Q_{\alpha}(r)$$
 (2-34)

The variance of conductance is given by Eq. (2-18) and the 1/f noise can be obtained from Eq. (2-25). The noise $(\delta g')^2$ of the cooper channel can be written as following,

$$\delta g^{2}(B,T) = -\frac{4s^{2}}{\pi^{2}} \int \frac{d\Delta E}{2k_{B}T} K(\frac{\Delta E}{2k_{B}T}) \frac{d}{d(1/\tau_{\phi})} F_{0}(\Delta E, B) \quad (2-35)$$

Substitution of F_0 yields numerical formula for the noise crossover. The difference between the analytical and numerical expressions for the field correlation is less than 10% [18]. We expect that the difference in the noise crossover function is similarly insignificant.

2.D.2.3 Characteristic field scale

From a measurement of the static variation of G versus magnetic field (the "magnetofingerprint"), we get the magnetic field correlation range B_c where $F(\Delta B)$ drops to half of its fully correlated value(i.e. $F(\Delta B=0)$). B_c represents the typical

spacing of the peaks and valleys in $\delta G(B)$ of the magnetofingerprint and it is shown[8,18] that the field correlation range of $\delta G(B)$ is determined by the phase breaking length L_{ϕ} in a quasi 1D sample (thickness t, width $W \ll L_{\phi}$). The value of B_c is given by

$$B_{c} = const \times \frac{h/e}{WL_{\phi}}$$

Beenakker et. al [18] calculated the numerical constant and showed that is equal to 0.95 for $L_{\phi} >> L_T$ and 0.42 for $L_{\phi} << L_T$.

In the 1/f noise measurement the field scale B_{c1} is defined as the magnetic field where the 1/f noise power drops to 3/4 of that of zero field. B_{c1} is the field scale required to suppress the particle-particle channel contribution to the 1/f noise, and is also determined by the phase breaking length L_{ϕ} . In quasi-1D system[8,13,14] B_{c1} is given by

$$B_{c1} = const \frac{h/e}{WL_{\phi}}$$

where the numerical constant is evaluated as 0.21 for $L_{\phi}>>L_T$ and 0.16 for $L_{\phi}<< L_T$ from Eq. (2-31) and (2-32).

2.D.3 UCF crossover function at strong magnetic field

Overview

At strong magnetic field where the cooper channel is completely suppressed, the magnetic field couples to the diffuson channel due to the Zeeman splitting of the electron spin state in the weak spin-orbit scattering limit. Because the $M_z=\pm 1$ triplet

states are sensitive to the Zeeman splitting, there will be a second reduction of UCF from suppression of the contribution of the diffusons with Mz=±1. The Zeeman effect can be incorporated into UCF theory following the work of Stone[14] or Feng's[13] calculations. According to Stone, the Zeeman effect can be incorporated by replacing ΔE by $\Delta E + g\mu_B B$ in Eq. (2-33). Stone claimed that for the 1/f noise in all dimensions and for Var(g) in quasi-1D samples, the characteristic field scale(Bc2) is determined by the energy correlation length ("Thouless energy") of a phase coherent area, $\hbar D/L_{\phi}^2$, not by the temperature. For Var(g) in 2D- or 3D- samples, B_{c2} given by $B_{c2}=E_{max}/g\mu_B$, where E_{max} is the larger of $\{k_BT,\frac{\hbar}{\tau_A}\}$. Independently, Feng calculated the Zeeman effect on UCF, and showed that the values of Bc2 are determined by the temperature in all situations when $L_T < L_{\phi} < L$. We have checked that Feng's formula in 1D is the same as the 1D formula based on Stone's approach. We also evaluated the noise crossover function in 2D, following Stone's calculation (see figure 2.5). We found that B_{c2} is determined by the larger of $\{k_BT, \frac{\hbar}{\tau_1}\}$ in all sample dimensions, and our current understanding of the B_{c2} is consistent with Feng's predictions. Thus Stone's statement about the Zeeman crossover of the noise is incorrect, although his calculations are correct. Here, we describe the calculations on the Zeeman effect on the UCF variance, and present our numerical evaluation of the Zeeman effect on the 1/f noise.

1D variance calculation

Feng has treated the Zeeman effect on UCF diagrammatically by taking the Zeeman energy into account in the spin-dependent electronic energy $\xi_{k,\nu}=\hbar^2k^2/2m+\nu\frac{g}{2}\mu_BH-E_F \quad \text{where }\nu=\pm 1 \text{ is the spin index. The complex calculation of the spin-dependent diffuson diagram in the particle-hole channel is carried out using a Dyson equation. Here, we skip the details of the algebra but$

explain the outline to get the variance of conductance in the particle-hole channel. From the algebraic manipulations, the particle-hole diffusion propagators $\Lambda_{\alpha\beta\gamma\delta}$ are obtained explicitly. The T=0 energy correlation function can be given, following Lee et.al.[8] and Al'tshuler and Shklovskii[3], by

$$F^{ph}_{0}(\Delta E, B) \approx \sum_{q_{ph}} \left(2 \sum_{\alpha \beta \gamma \delta} \left| \Lambda_{\alpha \beta \gamma \delta} (q_{ph}, 1/\tau_{\phi}, g\mu_{B}B) \right|^{2} + \sum_{\alpha \beta \gamma \delta} \text{Re}(\Lambda_{\alpha \beta \gamma \delta})^{2} \right) (2-35)$$

where, $q_{ph} = (\pi m/L)^2$, $m = 1, 2, \dots \infty$. By substituting the various expressions into this equation, the T=0 energy correlation function is

$$F^{ph}_{0}(\Delta E, B) = 2\left(\frac{e^{2}}{h}\right)^{2}L^{-4}\sum_{qph}\left\{\frac{4}{q^{4}} + \left(\frac{\Delta E}{D}\right)^{2} + \frac{2}{q^{4}} + \left(\frac{\Delta E - g\mu_{B}B}{D}\right)^{2} + \frac{2}{q^{4}} + \left(\frac{\Delta E + g\mu_{B}B}{D}\right)^{2}\right\}$$
$$+ \frac{2(q^{4} - \left(\frac{\Delta E}{D}\right)^{2})}{q^{4}} + \left(\frac{\Delta E}{D}\right)^{2} + \frac{(q^{4} - \left(\frac{\Delta E - g\mu_{B}B}{D}\right)^{2})}{q^{4}} + \left(\frac{\Delta E - g\mu_{B}B}{D}\right)^{2} + \frac{(q^{4} - \left(\frac{\Delta E + g\mu_{B}B}{D}\right)^{2})}{q^{4}} + \left(\frac{\Delta E + g\mu_{B}B}{D}\right)^{2}}\right\} \qquad (2-36)$$

where $q^{2} = q_{ph}^{2} + \frac{1}{L_{\phi}^{2}}$. The conductance fluctuations at T=0 are given by

 $F^{ph}_0(\Delta E = 0, B)$. One can recover the formula of the T=0 conductance fluctuations given by Feng's published result[13] and by the Lee and Stone result[2] for the case of B=0. From Eq. (2-18), the conductance fluctuations at finite temperature are

$$Var^{ph}[g(B,T)] \approx \int \frac{d\Delta E}{2k_B T} K(\frac{\Delta E}{2k_B T}) F^{ph}_{0}(\Delta E, B)$$

A typical term contributing to the conductance fluctuations with the Zeeman effect is,

$$Var[g(B,T)] \propto \sum_{m=1}^{\infty} \int_{0}^{t} d\eta K(\eta) \frac{1}{[(m^2 + \gamma)^2 + (\eta \pm \varsigma)^2]}$$
 (2-37)

where
$$\gamma = (\frac{L}{\pi L_{\phi}})^2$$
, $\eta = \Delta E / \varepsilon_c$, $\varepsilon_c = \frac{\hbar \pi^2 D}{L^2}$, $\zeta = g \mu_B B / (k_B T)$, $t = \frac{k_B T}{\varepsilon_c}$.

Figure 2.3a shows the evaluation of the finite temperature variance in the particlehole channel.

• 1D 1/f noise crossover function

From Eq. (2-25), the 1/f noise amplitude in the particle-hole channel can be calculated in a straightforward manner. A typical contribution is

$$\delta g^{2}(B,T) \propto \sum_{m=1}^{\infty} \int_{0}^{t} d\eta \ K(\eta) \left\{ -\frac{d}{d\gamma} \frac{1}{\left[(m^{2} + \gamma)^{2} + (\eta \pm \zeta)^{2} \right]} \right\}$$
 (2-38)

Figure 2.3b shows the evaluation of the noise crossover function in the particle-hole channel.

Characteristic field scale

The field dependence of the conductance fluctuations due to the Zeeman effect in the particle-hole channel can be characterized by the field scale B_{c2} where the variance or the 1/f noise drops to the half of the value at zero field. From figure 2.3a for variance and 2.3b for the noise, we conclude that for the case $k_B T >> \frac{\hbar D}{L_{\phi}^2}$ in quasi-1D at finite temperature, B_{c2} is given by

$$B_{c2} \cong 2.7 \frac{k_B T}{g \mu_B}$$

in all dimensions. B_{c2} is the same for measurement of the variance or the 1/f noise. When $k_BT << \frac{\hbar D}{L_{\phi}^2}$, B_{c2} is determined by the Thouless energy. Figure 2.4 shows the

evaluation of the UCF noise at different temperatures with a fixed Thouless energy, and implies that B_{c2} is determined by the larger of $\{k_BT, \frac{\hbar D}{L_{\phi}^2}\}$.

Effect of spin-orbit scattering

The calculation of the Zeeman effect shown so far has been limited to the weak spin-orbit scattering limit. Strong spin-orbit scattering breaks the spin-rotation symmetry and the Zeeman effect can not be observed. This interplay between the Zeeman effect and the spin-orbit scattering is demonstrated in figure 2.5. Figure 2.5 shows the relative amplitude of the variance of the particle-hole channel for several values of the spin-orbit scattering rate. It is shown that for $L_{\phi} \approx 3L_{so}$, we are already in the strong spin-orbit scattering limit.

2E. Weak localization and low field magnetoresistance

The usefulness of weak localization(WL) is that it allows one to extract the electron transport length scales from the low-field magnetoresistance. One can get then information about the phase breaking mechanism from the temperature dependence of the phase breaking rate. Here, we describe briefly the quasi-1D WL application to the magnetoresistance. A comprehensive overview of WL is given by the review of Bergmann (1984)[19].

The 1D WL correction to the resistance can be written in the terms of the spin-triplet and spin-singlet[20],

$$\frac{R(0) - R(B)}{R(0)} = \frac{e^2}{\pi h} \frac{R}{L} \left\{ \frac{3}{2} \left[L_{\phi}^{-2} + \frac{4}{3} L_{so}^{-2} + \frac{2}{3} L_{s}^{-2} + L_{B}^{-2} \right]_{triplet}^{-1/2} - \frac{1}{2} \left[L_{\phi}^{-2} + 2L_{s}^{-2} + L_{B}^{-2} \right]_{singlet}^{-1/2} \right\}$$
(3-39)

where the effect of a magnetic field is expressed in terms of a one-dimensional "magnetic length", $L_B=(\frac{\sqrt{3}}{\pi}\frac{h}{2e}\frac{1}{BW})$. $L_{\rm so}$ is the spin-orbit scattering length and $L_{\rm sf}$ is the spin-flip scattering length assuming the spin is static. This formula is valid in the region of $L_{\phi}(T)>W$ and $W< L_B$. In one-dimensional WL, the resistance correction is sensitive to W, giving an estimation of W of the 1D wire. In the case of $L_{\rm so}<< L_{\phi}$, the triplet term is suppressed, resulting in a positive magnetoresistance. Strong spin-flip scattering suppresses the WL contribution completely.

References

- [1] R. Landauer, Phil. Mag. 21,863 (1970).
- [2] B. L. Al'tshuler, Pis'ma Zh. Eksp. Teor. Fiz. 41, 530 (1985) [JEPT Lett. 41, 648 (1985); P. A. Lee and A. D. Stone, Phys. Rev. Lett. 55,1622 (1985).
- [3] B. L. Al'tshuler and B. I. Shklovskii, Zh. Eksp. Teor. Fiz. 91, 220 (1986) [Sov. Phys. JETP 64, 127 (1986)].
- [4] Y. Imry, Europhys. Lett. 1, 249 (1986).
- [5] For a review of random matrix theory, see T. A. Brody et al., Rev. Mod. Phys. 53, 385 (1981).
- [6] F. J. Dyson, J. Math. Phys. 3, 140 (1962); 3, 166 (1962); F. J. Dyson and M. L. Metha, ibid. 4, 701 (1963).
- [7] D. S. Fisher and P. A. Lee, Phys. Rev. B23. 6851 (1981).
- [8] P. A. Lee, A. D. Stone, and H. Fukuyama, Phys. Rev. B 35, 1039 (1987).
- [9] R. Balian, Nuovo Cimento 57, 183 (1968); K. A. Muttalib, J.-L. Pichard, and A.D. Stone, Phys. Rev. Lett. 59, 2475 (1987).
- [10] C. W. J. Beenakker, Phys. Rev. B47, 15763 (1993).
- [11] F. J. Dyson, J. Math. Phys. 13, 90 (1972).
- [12] D. J. Thouless, Phys. Rev. Lett. 37, 1167, (1977).
- [13] S. Feng, Phys. Rev. B 39, 8722 (1989).
- [14]A. D. Stone, Phys. Rev. B 39, 10736 (1989).
- [15] V. Chandrasekhar et. al, Phys. Rev. B 42, 6823 (1990).
- [16] S. Feng, P. A. Lee, A. D. Stone, Phys. Rev. Lett. **56**, 1960 (1986)
- [17] B. L. Al'tshuler and B. Z. Spivak, Pis'ma Zh. Eksp. Teor. Fiz. 42, 363 (1985)[JETP Lett. 42, 447 (1985)]
- [18] C. W. J. Beenakker and H. van Houten, phys. Rev. B 37, 6544 (1988)
- [19] G. Bergman, Phys. Report 107, 1 (1984).

[20] B. L. Al'tshuler and A. G. Aronov, Pis'ma Zh. Eksp. Teor. Fiz. 33, 515 (1981)
[JETP Lett. 33, 499 (1981)]

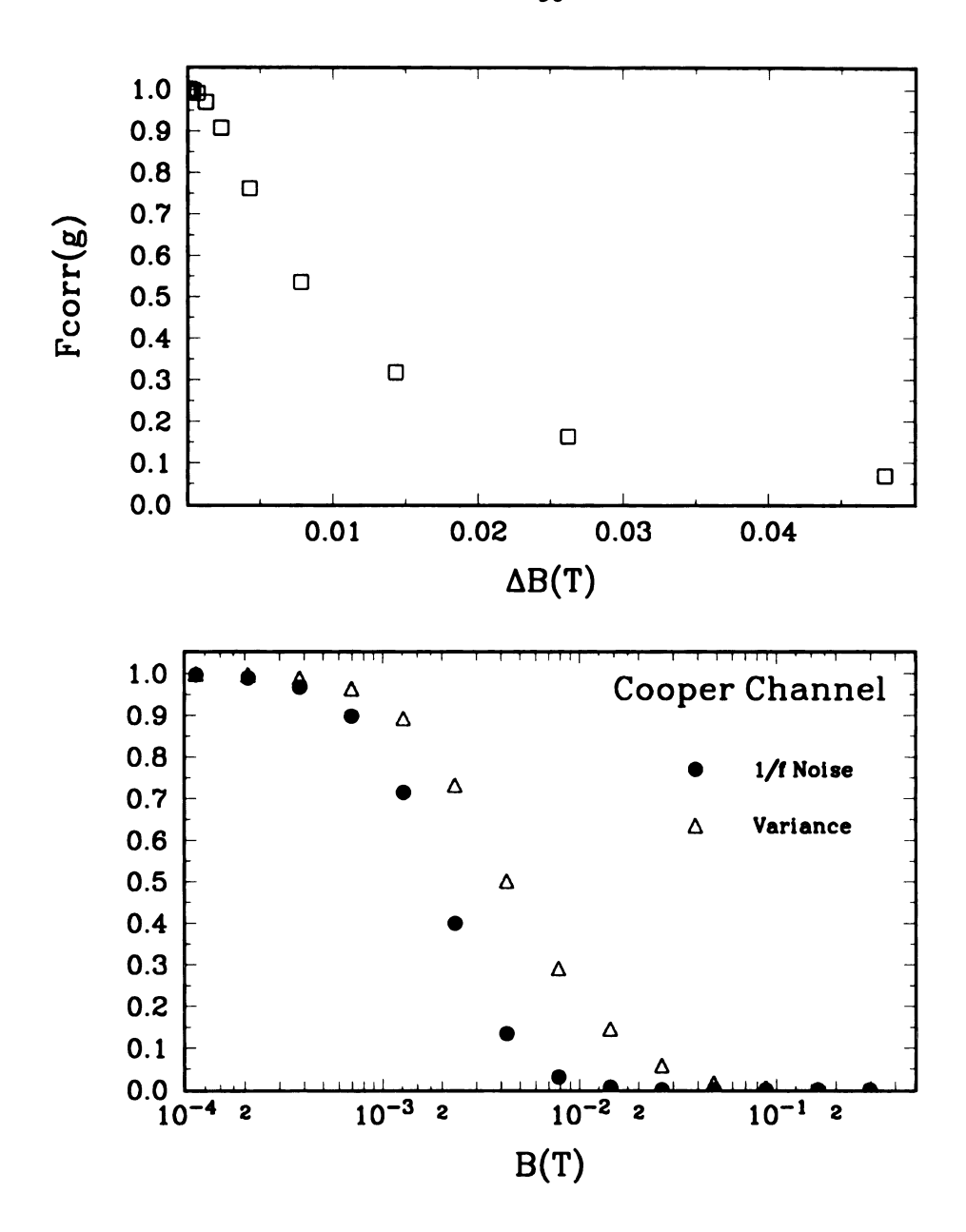


Figure 2.1 Evaluation of (a) 1D field autocorrelation function $F(B=0, \Delta B)$ calculated by Beenakker and von Houton and (b) variance $\delta g^2(B)$ and 1/f noise crossover $\nu^{pp}(B)$ in particle-particle channel. The parameter values are $L_{\phi}=1~\mu m$, $L_T=0.17~\mu m$.

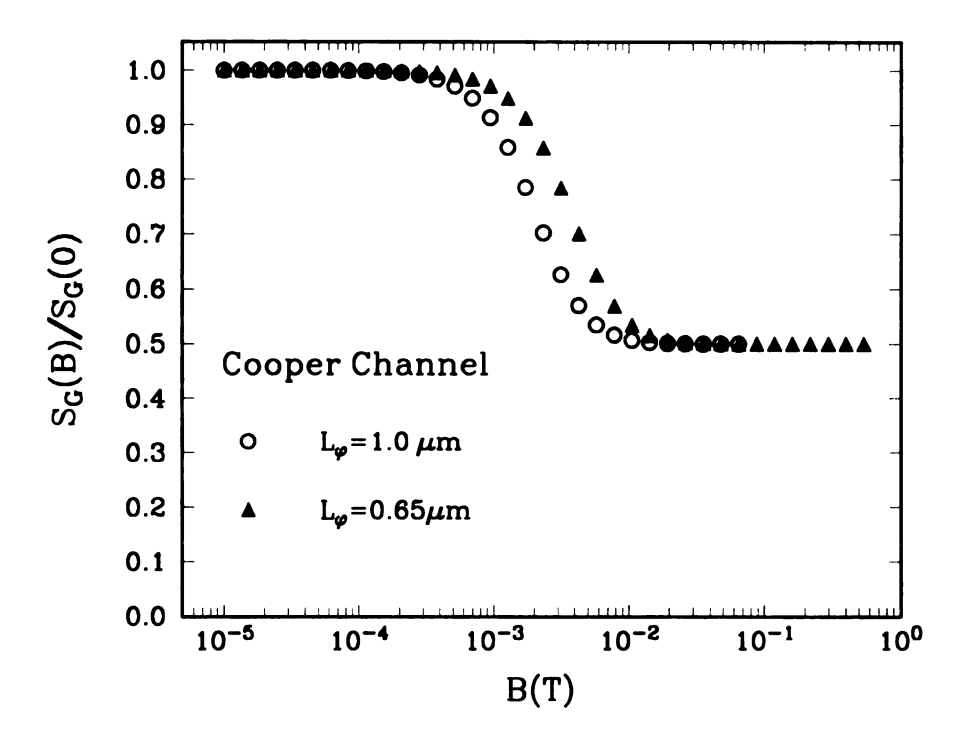


Figure 2.2 Evaluation of the 1D 1/f noise crossover function $\nu^{pp}(B)$ in particle-particle channel at L_{φ} = 1 μm and 0.65 μm . The L_T is fixed as 0.17 μm .

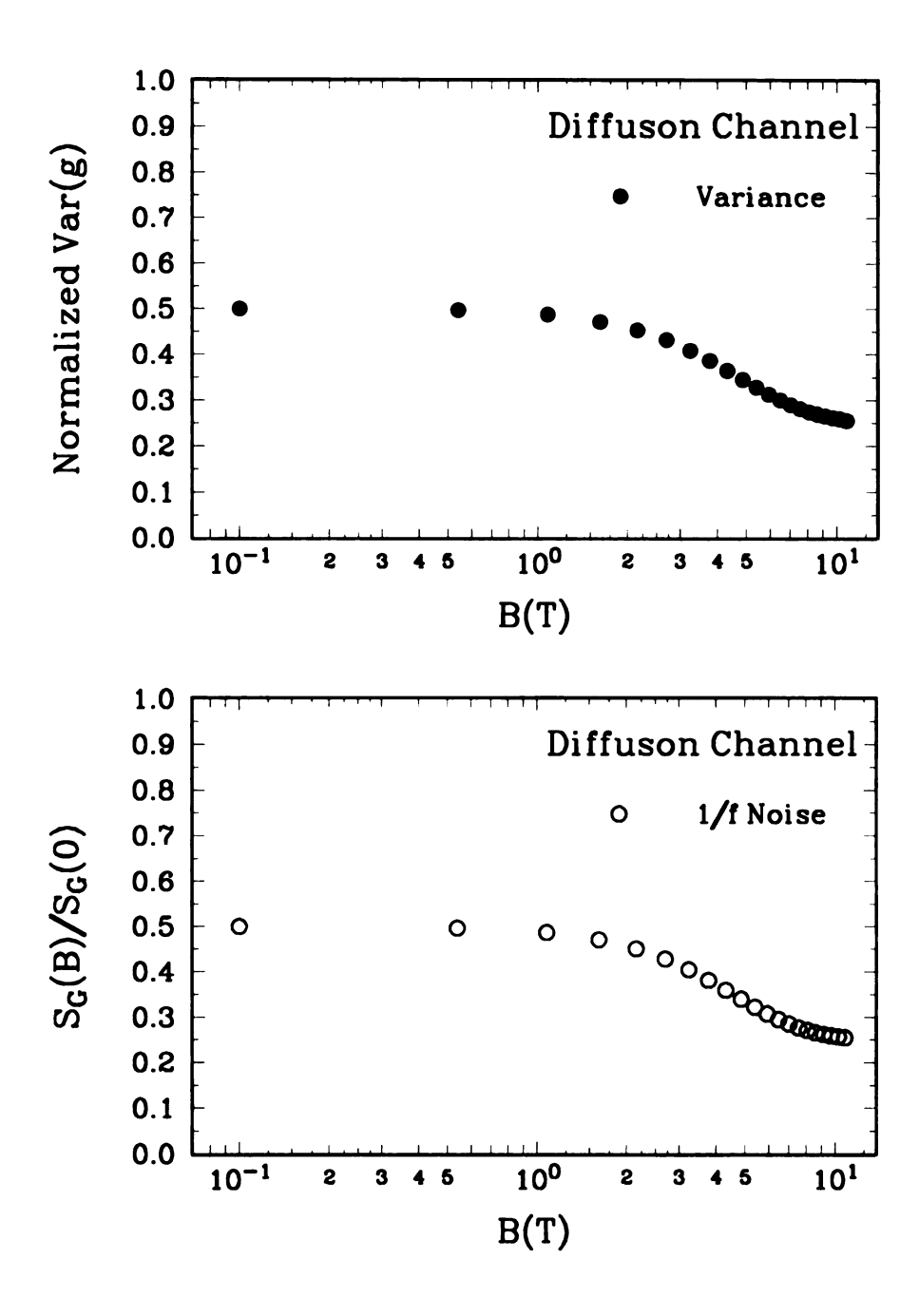


Figure 2.3 Evaluation of the finite temperature (a) 1D variance and (b) 1/f noise in particle-hole channel. The parameter values are $L_{\phi} = 1.0 \mu m$, T = 1.9 K, and $D(\text{diffusion constant}) = 7.8 \times 10^{-3} \text{ m}^2/\text{s}$.

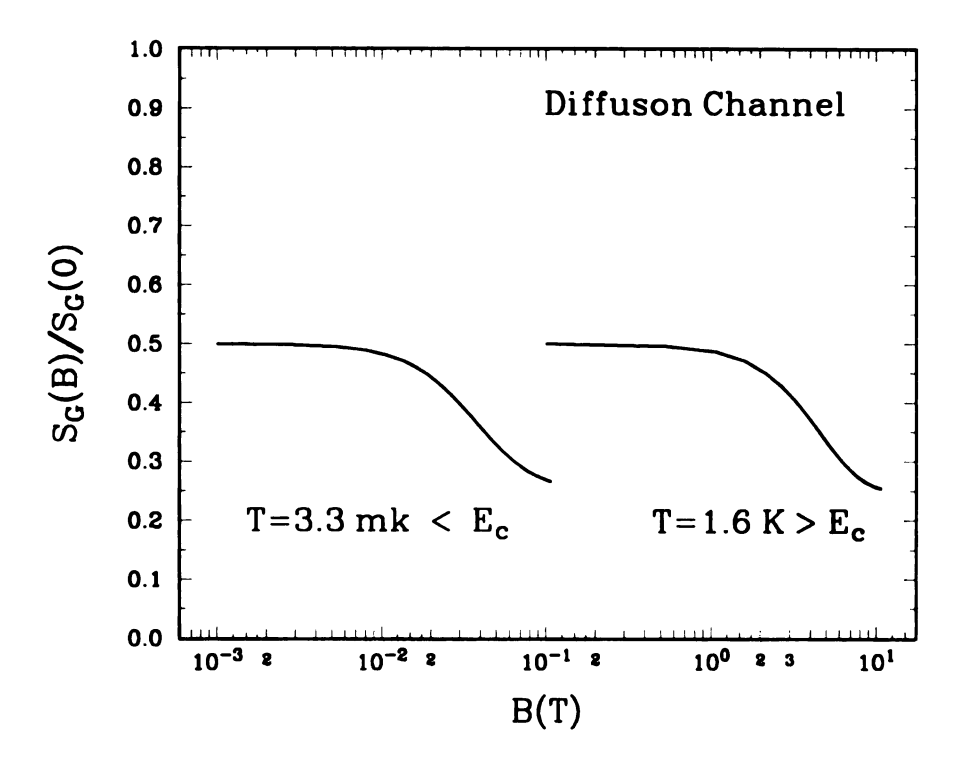


Figure 2.4 Evaluation of the 1/f noise crossover in the particle-hole channel for T = 3.3 mK and 1.6 K. In both cases E_c (Thouless energy) = 59 mK. For the case $k_BT > Ec$, $Bc2 \sim 4$ T and is determined by the temperature. For the case $k_BT < Ec$, $Bc2 \sim 0.04$ T and is determined by the Thouless energy

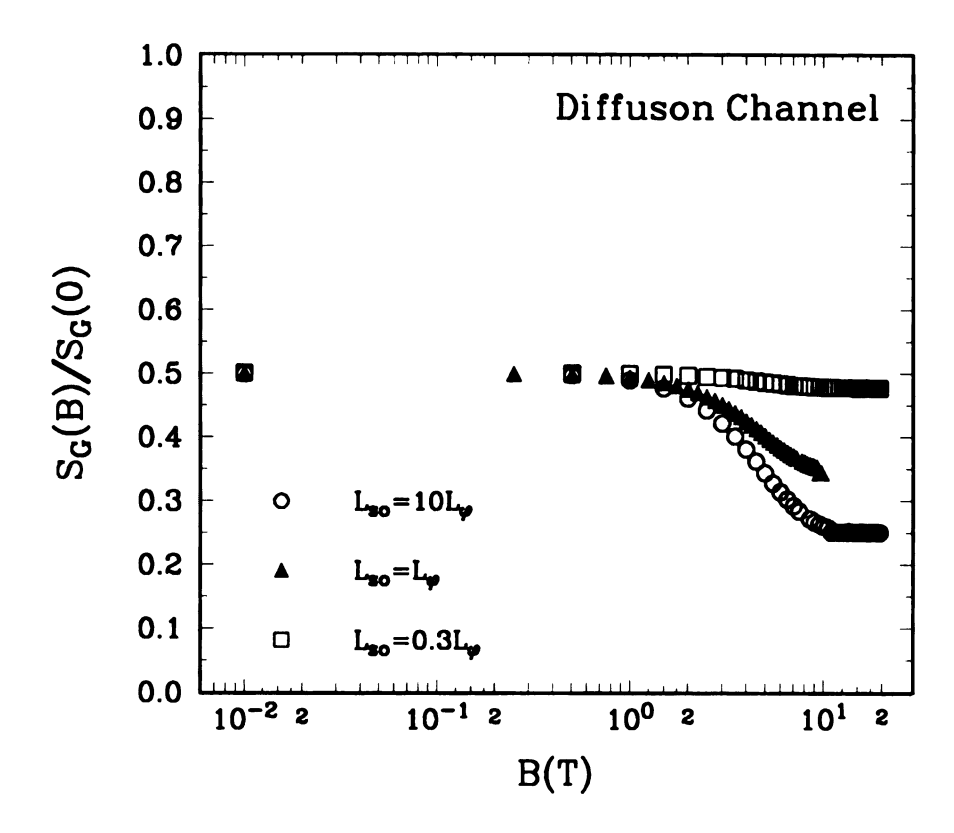


Figure 2.5 Evaluation of the 2D 1/f noise crossover in the particle-hole channel with different spin-orbit scattering rate. The parameter values are L_{φ} = 1.0 μm , L_{T} = 0.17 μm and E_{c} =59 mK. At L_{so} = 0.3 L_{φ} , the Zeeman effect on the 1/f noise is almost invisible.

Chapter 3

Experimental Techniques

In this chapter, I will discuss the experimental requirements and techniques to carry out quantum transport in a low spin-orbit metal. Since the spin-orbit scattering rate in metals depends on the atomic number(Z), we studied quantum wires and films made of the lightest of metals, lithium. For this experiment, we utilize quench-condensation of films, sub-micron electron beam lithography, optical lithography and in-situ measurement of the 1/f noise. To recover the small 1/f noise, we utilize a two-phase digital lock-in amplifier which allows simultaneous measurement of total noise(1/f noise + background) and background. A magnetic field up to 9T is applied with superconducting (SC) magnet outside the vacuum-can of a He-4 pumped cryostat..

3A. Ouench-Condensation

There are several ways to fabricate a film on a substrate; thermal evaporation, electron-beam evaporation, sputtering, chemical vapor deposition and molecular beam epitaxy. Different methods give different film quality from single crystal to highly disordered films. The thermal evaporation used in this work produces polycrystalline films and the grain size can be controlled by the substrate temperature at the evaporation stage.

The metallic lithium is very reactive in air, so, it must be handled in an inert gas (He, or Ar) atmosphere or in a high vacuum. Metallic lithium is thermally evaporated onto a cold substrate kept at liquid helium temperature and the deposited metal atoms are "quench-condensed" due to low diffusion mobility. All the electrical

measurements are performed in-situ, with electrical wires connected already on the substrate before the Li evaporation. The important factors in the quench-condensation are the following; fine alignment between the Li source and the lithographed mask on the substrate, a scheme for holding the Li source inside the filament, a pre-evaporation to remove the contaminated surface of Li source, and minimization of thermal load on the substrate by providing a good heat-sinking scheme and a fast shutter control during the evaporation.

Figure 3.1a shows a schematic set-up for the quench condensation with a cryo-evaporator inside the vacuum-can. The diameter of the vacuum-can tail is set as 2.5 inch due to a geometrical restriction given by the 9T supercondcting NbTi magnet. The substrate, shown in figure 3.1b, has a sub-micron mask fabricated with electron-beam lithography and is heat-sunk to the 1K pot. The RF-filtered electrical wires are for in-situ measurement.

Lithium has a high vapor pressure and is easy to evaporate. The melting point is 180°C. Lithium reacts with some metals, (for instance, W or Au) and forms alloys, so, materials such as Ta, Ni-Cr and Fe based alloys are used for the heating elements. Be aware that Cr or Fe impurities are strongly magnetic in the Li matrix[1]. To evaporate both directions, a filament geometry is used with a scheme to keep a Li blob from falling out of the filament. A blob of lithium is inserted into the filament in an Ar gas-filled glove bag. The Li blob is somewhat contaminated at its surface during loading into the cryostat. Several stages of pre-evaporation of the Li blob are carried out during the cooling of the cryostat. A spring-loaded shutter and radiation baffles are located between the filament and the substrate. The fast shutter control helps to minimize thermal shock to the mask on the substrate.

A film thickness monitor, located at the bottom of the vacuum can, is heatsunk at 4.2 K to minimize drift of the temperature, and hence the resonance frequency (~6 MHz) of the Quartz sensor crystal. A small area on the back of the sensor crystal is greased down to the housing without deteriorating the gold-plated electrical contact. All the electrical connections are made with a solid Copper miniature coaxial cable (capacitance ≈ 30 pF/ft at 5 kHz) except the connection just below the vacuum can lid where 304 stainless steel mini-coax (capacitance ≈ 50 pF/ft) is used. Hermetically sealed microdot miniature connectors are used. The noise level in the film thickness and rate readings is not problematic in the case of evaporation of heavy material, for example, Ag or Au. In the case of Li evaporation (lithium has a very low mass density only about half that of water), the signal to noise ratio is worse and sometime problematic in terms of reading the evaporation rate. Checking all the electrical contacts including the spring contact at the back of the sensor crystal and proper grounding of the electrical circuits are helpful.

3B. Electron-beam Lithography

The demand of large scale integrated circuit devices has driven the development of microfabrication technique. Nowadays, state-of-art lithography produces nano-meter scale structures which can be smaller than the electron phase coherence length.

In low temperature 1/f noise experiments, signal to noise ratio (SNR) is somewhat problematic. According to UCF theory[2], the quasi one-dimensional (1D) geometry (width $< L_{\varphi}$) has better SNR than 2D film. A typical value of the phase coherence length is of the order of one micron or less at low-temperature, so the transverse dimension of the sample must be in the sub-micron or nano-meter scale. Fabrication of sub-micron sized samples requires lithographic technique beyond optical. Several methods are known to fabricate sub-micron structures; X-ray lithography[3], deep UV lithography[4], step-edge technique[5] and electron-beam lithography[6,7]. For this work, we utilize electron-beam lithography (EBL). EBL is

done in a scanning electron microscope (SEM) system built with control for electronbeam writing. The focused electron beam of diameter a few nanometers or less, is scanned in the desired pattern over an e-beam sensitive resist. Then, the exposed resist is developed and the resulting image of the resist pattern is used as a mask.

The SEM is a JEOL JSM840A microscope with a tungsten source filament. Exposure onto the e-beam sensitive resist is done by the focused e-beam with energy of 30 keV (the maximum for this system is 35 keV). The e-beam current, used for small structure patterning, is 5 pA, and a beam-blanking shutter controls the exposure time. The important factors to get optimum performance in EBL are the following; (1) generation of a well-focused e-beam with fine tuning of astigmatism in the beam lenses, and sharp focusing of the high energy e-beam on top of the imaging layer, (2) correct beam dose distribution to minimize the proximity effect, i.e. overexposure of nearby parts of the pattern, (3) correct alignment of lithographic patterns, (4) correct procedure for developing the exposed resist with control of developing time and environmental conditions, (5) formation of the "undercut" profile of the developed area, (6) proper set-up of SEM electronics to minimize the noise from electrical lines.

3B.1 Resolution, Undercut profile.

The most popular electron-beam resist used as the imaging layer is PMMA (Polymethl Methacrylate) resist which has an inherent resolution of about 20nm[7]. Finite thickness of the resist leads to multiple scattering of the electron beam, resulting in a bulbous interaction volume. If the resist thickness is kept low, then the reduced scattering volume and shorter developing time lead to higher resolution. Even though the thin resist scheme can improve the resolution, thick resist is better to get the proper vertical profile, i.e. "undercut" profile, of the developed resist for the device applications. The undercut profile of the resist keeps the evaporated metal

through the mask from electrically shorting to the outside, so is crucial in the device fabrication. Bilayer resist systems[8,9] are used to improve the resist profile of the mask. A bilayer scheme consists of a thin PMMA layer on the top of a thick copolymer layer, MMA. The bottom layer planarizes substrate topography and minimizes backscattering at the top imaging layer. Because the copolymer is more polar than PMMA, the proper choice of a single strong developer such as methylisobutylketone (MIBK) produces the desirable undercut profile[6,7]. Although the undercut profile can be obtained in the bilayer resist system, the control of the resist thickness and developing rate for both layers is important. If the bottom layer is considerably thicker than the top layer, then developing of both layers at the same time could result in widening of the pattern.

We use 9%-copolymer dissolved in 2-ethoxyethanol solvent as a bottom layer and 2%-PMMA dissolved in chrolobenzene solvent as a top layer. A single developer, MIBK, for the both layers is used. Figure 3.2 demonstrates the line width versus line dose obtained from the fabrication of 1 µm-long line with five-terminals attached. Figure 3.3 shows the SEM photograph of the bilayer resist pattern just after it is developed. The line doses vary from 0.6 nC/cm to 1.4 nC/cm. To minimize the proximity effect on the sample line, critical doses are exposed in the big areas nearby the sample line. Two different sets of data in figure 3.2 correspond to the results obtained from two different thickness of the copolymer layer. Total thickness of each bilayer system is about 320 nm and 400 nm respectively. A line resolution as small as 30 nm is achieved. Thinning the bottom copolymer improves the line resolution with better yield of fine line fabrication.

For the pattern to work as a mask, the profile must be "undercut". Figure 3.4a shows both the undercut profiles and line resolutions, obtained in the \sim 400 nm thick bilayer system. Several lines, separated by 1 μ m, are patterned with the line doses from 3 nC/cm at the left to 7 nC/cm at the right. Line resolution as small as 40 nm is

obtained. The SEM photo in fig. 3.4b shows that the undercut profile expands ~80nm deep into each side wall. Figure 3.5 also shows the ~100 nm deep undercut profile of the bilayer resist exposed by an area dose of 225 μ C/cm². From this bilayer scheme, we are able to obtain the resolution and a reasonable amount of undercut in the submicron mask.

This bilayer resist scheme works in most applications but has limitation in terms of controlling the amount of the undercut without losing the line resolution. One approach to avoid the competition between resolution and undercut profile, is to use mutually exclusive developers for each layers[9]. For example, the copolymer is insoluble in a non-polar solvent such as chlorobenzene, which is a solvent for PMMA. PMMA is insoluble in a polar solvent such as ethoxyethanol, which is a solvent for the copolymer, MMA. In this scheme, the amount of the undercut is limited by the e-beam sensitivity of the bottom layer.

3B.2 sub-micron metal stencil.

Fabrication of a sub-micron mask for low-temperature quench-condensation, combined with in-situ measurement, requires a major change of the conventional lithography because the final "lift-off" can not be carried out. The mask should provide mechanical rigidity and electrical isolation between the deposited material on the substrate and that on the mask surface. Also, the mask must be thermally resistant during the evaporation or thermal cycling. Low-temperature application of the bilayer resist scheme is generally painful unless some extra treatment of the resist is done -- for example, evaporation of all the solvent out from the resist matrix. Application of a metal stencil is the best, and several techniques to produce sub-micron metal stencil have been reported, including the "brush-fire" technique[10], and trilayer lithography[11]. The brush-fire technique, developed by G. Dolan, produces

the metal stencil without losing the e-beam resist resolution. Instead, we utilize the trilayer structure, i.e. PMMA/metal/copolymer structure. A 50nm thick layer of aluminum is used for the metal layer because the aluminum can be etched easily. Figure 3.6 shows a schematic procedure for trilayer lithography and the details are given in Table 3.1. Although the trilayer process provides us with the easy control of the undercut and the relatively easy process in metal stencil fabrication, the resolution of the final mask is, however, determined by the isotropic chemical etching process on the metal layer, resulting in a wider pattern than the imaging layer. An alternative approach to avoid this problem is to do anisotropic etching of the metal layer; an aluminum layer can be etched using Cl-based reactive ion etcher(RIE).

Figures 3.7a, 3.7b show SEM photographs of the top view and the side view of a sub-micron metal stencil on top of the copolymer resist. The aluminum metal layer is etched in OH-based solution and the stencil opening is 0.3 μ m wide. The 0.3~0.4 μ m deep undercut into a side wall is shown and is quite uniform throughout the patterned edges. A stencil opening as small as 0.2 μ m has been achieved.

Figure 3.8 shows a schematic diagram of the sample geometry, which has five probes attached. For the 1/f noise measurement, the two sides of the sample form the two lower arms of the Wheatstone bridge circuit shown in figure 3.9.

The characteristics of the samples used in this thesis are summarized in Table 3.3. Samples #5 and #6 were fabricated using Ta filament and are discussed in Chapter 4. Samples #1-4 were fabricated using Ni-Cr filament and are discussed in Chapter 5.

Table 3.1. Procedure for trilayer e-beam lithography.

1. Copolymer coating

Spin(static dispense) 9%-copolymer (casting solution is 2-Ethoxyethanol) @ 4000 RPM and 1 min., then bake the substrate about 1 hour @ 137~140°C. (The air oven should be dehydrated.)

Hints:

- (1) The baking temperature could be lower than 140°C, but it is better to be above 124°C which is the glass temperature of the copolymer.
- (2) The sensitivity of copolymer has small dependence on the baking temperature.
- (3) For cryogenic usage, it is better to get the solvent out as much as possible. The melting point of 2-Ethoxyethanol is \sim -90F
- 2. AL layer coating: use thermal evaporator with water-cooled stage, and deposited thickness is ~50 nm with a chamber pressure, ~2E-6 torr.

3. PMMA layer coating.

Spin 2%-PMMA (casting solution; chlorobenzene) @ 4900 RPM, 1min, then bake the substrate about 1hr @ 125°C in air convetion oven. Don't bake the substrate at higher temperature -- aluminum metal layer will severely crack.

Hint:

- (1) The glass temperature of PMMA is ~ 104°C; as long as it is basked above the glass temperature, the resolution of polymer matrix is fine.
- (2) Eventually the PMMA layer is stripped out by O₂ RIE to maximize the cryogenic application.

4. Sample mounting in SEM chamber

Put a small drop of Ag paint on the substrate for the E-beam focusing and wait until it is completely dried. Using a clean dry gas, blow off dirt, if any. Mount the sample onto a stub. The sample must be flat against the stub. Load the sample into the chamber and wait until the pressure inside the chamber reaches the base pressure.

5. Electron- beam exposure.

(1) Set the SEM to the following configuration:

Voltage: 35 kV

Gun Bias: Auto

Coarse Probe Current: 6e-12 (the smallest)

Aperture: 4 (the smallest)

Working Distance: 15 mm

EOS Mode: SEM

Image Select: SEI

- (2) Obtain the proper saturation current and align the gun.
- (3) Adjust the aperture centering and alignment mark.
- (4) Focus the beam at as high as magnification. Correct the astigmatism in the beam using the standard. Repeat this step until an optimum image is achieved.
- (5) First, the sensitivity test related to e-beam exposure needs to be done critically.
- (6) Do coarse alignment. Coarse alignment is not a problem either SE mode or SEM mode for Al 50 nm case because Au contact pads underneath Al layer give enough contrast.
- (7) Do fine alignment between the contact pads and e-beam pattern.
- (8) Expose the e-beam.
- (9) Develop the resist about 45 sec with developer, MIBK:IPA(1:3) at room temperature.

Hint: the solubility ratio between the exposed and unexposed PMMA layer is high for MIBK:IPA developer.

(10) Rinse with IPA (30 sec), and blow dry with N2 gas

6. check pattern carefully with OPTICAL microscope (X1000)

7. Al layer Wet-ETCH

Prepare fresh etching solution(for example, diluted KOH), monitor humidity and temperature.

Calibrate the etching time everyday and etch the substrate.

See the distinct color changes.

Rinse it very carefully with DI water.

Dry the substrate either the N_2 gas blow dry or spinner dry(20 sec @ 4000 rpm).

Run a low power RIE process (19 W, 50 mtorr, 30 sec, 12 dc-bias)

Recheck the etching status of the substrate. -- The substrate should have a very nice edge and some shadow. Be sure to etch completely through out the pattern.

Develop the copolymer layer; as long as it etches through completely, the copolymer is developed homogeneously and reasonably fast.

8. Develop the COPOLYMER

Develop the copolymer resist with MIBK: IPA (1:3) developer in 90 sec, and rinse it with IPA, and rinse it with DI water. Dry the substrate (spinner dry or blow dry). Take a look and the substrate should be clean and uniformly developed. The nice, optically-visible undercut can be defined with the continuous developing as long as 3 min. Be aware that MIBK itself will dissolve the butylacetate based Ag paint.

9. RIE pattern transfer.

Use high power O_2 RIE (99W, pressure ~ 75 mtorr, processing time ~ 90 sec). It will take the top PMMA out and transfer the etched pattern in the metal layer down to the bottom copolymer layer. Proper control gives a well-defined undercut and clean substrate. A 3 min. long RIE process gives about $0.5\mu m$ undercut, with optical halo.

10. SEM check

Check the metal stencil opening with e-beam current of 5 pA, at magnification around 5000X ~15000X.

11. check connections between Al layer and Au pads electrically

3C. Optical Lithography

Microfabrication of features bigger than 1µm can be done optically. A photosensitive resist (for example, Shipley 1813) undergoes a chemical change after it is exposed optically. When developed, it forms a mask for microfabrication.

Defining a vertical profile of the mask is generally important in the application of photolithography and can be controlled easily using several different approaches. We use a bilayer photoresist scheme where the sensitivity of each resist is controlled by the different UV exposure on the layers. This bilayer scheme produces a $1 \sim 1.5 \, \mu m$ deep undercut profile at the bottom layer with proper exposure and developing. Evaporation of metal through the mask is done at an angle of 45° while spinning the substrate. This process allow us to get a well-tapered contact leads for the next step. Table 3-2 summarizes the procedure of bilayer optical lithography.

Table 3.2 Bilayer Optical Lithography

- 1. Make a contact printing mask and prepare clean substrates.
- 2. Spin the photoresist (Shipley 1813) @ 4900 rpm during 30 Sec. Watch out for the edge bead. Bake the substrate @ 90° C during 30 min. inside air convection oven. (The oven must be pre-baked and dehydrated). The resulting thickness of the photoresist layer is about $1.1\sim1.3~\mu m$
- 3. Warm up the Hg UV lamp (100 watt $\lambda = 240 \sim 350$ nm) more than 10 min.. Do blank exposure about $10 \sim 12$ second.
- 4 Spin and bake the top layer of photoresist (Shipley 1813) at the same condition. Cool the substrate down.
- 4. Do contact printing with mask; expose the UV on the substrate during 11 second.
- 5. Develop the substrate during about 45-50 second.
- 6. Check the developed pattern and amount of the undercut.
- 7. Evaporate metal onto the substrate; tilt the substrate at 40°~45° from the evaporation source and spin during the evaporation.
- 8. Soak into Acetone and lift off the resist.

Table 3.3: Sample characteristics. The samples discussed in chapter 5 are 1,2,3 and 4. Sample 5 and 6 are discussed in Chapter 4.

Sample	Length	Width	Thickness	$R_{\square}(\Omega)$	l _e (nm)	L _φ (μm)
	(μm)	(μm)	(nm)	at 1.6 K		at 1.6 K
1	20	0.11	13	5.75	13	0.3
2	20	0.11	13	11.5	4.4	0.18
3	5800	205		7.8		0.26
4	5800	205		1.7		0.57
5	20	0.2	33	0.9	32	1.3
6	20	0.45	54	0.45	40	1.4
Bishop		0.074	25	2.1	20	1.0

3D. 1/f Noise Measurement.

The standard procedures for measuring resistance fluctuations (1/f noise) involve passing a current through the sample, thereby converting resistance noise to voltage noise by Ohm's law. (See also figure A in the Appendix.) The chief difficulty in such measurement is that the noise from the sample may be hidden by large background noise-- either Johnson noise or preamplifier noise. Of course the signal from the sample can be increased simply by increasing the measurement current, but this is often unacceptable due to Joule heating. Several methods have been used to reduce the background noise such as an ac bridge technique[12], or use of a cooled step-up transformer[13]. Recovering the 1/f noise from the background requires a second measurement without current, then the background is subtracted from the first total noise measurement. This procedure relies on stable background noise.

An alternative approach is to measure noise and background simultaneously. Several such techniques have been discussed. The two amplifier cross-correlation technique[14] rejects the preamplifier noise in the background, but does not reject the sample Johnson noise. The double-frequency ac method[15] requires that the bridge circuit must be in balance at both frequencies.

3D.1 dual-phase technique.

There are two elegant methods that subtract background noise using the ac bridge method with a single drive frequency. First, one can simultaneously measure the in-phase (0°) and quadrature (90°) signals from the bridge using a dual-phase lock-in amplifier. The power spectrum of the former contains both sample resistance noise and background, while the power spectrum of the latter contains only background. Subtracting the two spectra yields the sample noise alone. Unfortunately, commercial lock-in amplifiers tend to have large phase noise, so this

technique is limited in practice. Verbruggen et al. showed that the background is eliminated by correlating the two orthogonal outputs of a dual phase lock-in amplifier set to phases of plus and minus 45° with respect to the bridge current[16]. The 45° cross-correlation method also requires extremely good orthogonality and low phase noise in the lock-in amplifier.

To achieve the extreme phase stability and orthogonality need for these methods, we use a completely digital measurement system[17]. In addition to these requirements, a digital measurement system demands a large real-time calculation bandwidth, since it acts as both lock-in amplifier and spectrum analyzer. The recent development of the digital signal processor (DSP) integrated circuits makes it possible to implement such a system using only a DSP board with a small amount of memory, a digital-to-analog interface, and personal computer.

3D.2 Digital lock-in amplifier.

(This part is based on our article published in Review of Sicentific Instruments in 1992.)

We have developed a noise measurement system based on the Motorola DSP 56001 digital signal processor. Figure 3.8 shows our noise measurement system using the Motorola DSP boards and personal computer(PC). The digital signal processor and several kilobytes of memory lie on one board. A second board contains 16 bit D/A and A/D converters which operate from a single clock, assuring their synchronization. A sine wave generated by the D/A converter excites the bridge. By choosing the frequency of the excitation signal to be commensurate with the D/A clock frequency, total harmonic distortion (THD) 140 dB below the carrier is achieved. A third board is an interfacing board with the PC.

The difference signal from the bridge is amplified by a low-noise preamp, such as the Stanford SR 560 or the PAR 116. The output of the preamp is low-pass

filter is sufficient to prevent aliasing with the sigma-delta-type A/D converter which has the high sample rate. The sigma-delta A/D converter samples the incoming signal at a rate 128 times faster than the normal data conversion rate, then averages groups of 128 points to get the output. Since the Motorola A/D converter is supplied with dc power levels of 0 and 5 V, the A/D inputs are dc biased to 2.5 V with a simple homebuilt differential-to-differential level shifter from the standard op-amp circuits. Hence the signal can be ac coupled.

Figure 3.9 shows the block diagram for the digital signal processing of the input signal. First, the phase of the signal is shifted to compensate for the overall phase shift of the experiment. The signal is digitally mixed (multiplied) by two orthogonal sine waves chosen to be either at 0° and 90° or at ±45° with respect to the reference. The mixed signals are digitally filtered[18] and the sampling rate is decimated to reduce the number of points stored in memory on the DSP board and later Fourier transformed by the PC. The processing of filtering and decimation is represented by the following equation:

$$y(m) = \sum_{k=1}^{N} h(k)x(mn-k)$$

where n is the decimation ratio, h(k) are the filter impulse response coefficients, N is the number of filter taps, and x and y are the input and output data streams, respectively. We performed the digital filtering in three nested stages to reduce the number of filtering taps in any one stage. The advantage of a multistage digital filter is that the initial stages may have wide transition bands as long as aliased signals do not appear in the final passband of the complete three-stage filter[19]. Only the final stage need have a sharp transition band to minimize the number of unusable points in

the power spectrum. We designed three Chevychev equiripple FIR filters with maximally flat passbands, using the Monarch software package. Three filters have 75, 51, and 40 taps, respectively. Transfer functions of the three filters are shown in figure 3.10. When used with a 10-5-2 decimation scheme, these filters provides over 100 dB attenuation of the signals above the Nyquist frequency of the final (decimated) sample rate.

The PC starts the DSP system to collect the data, and simultaneously analyzes the data from the previous run. The PC performs fast Fourier transforms (FFT) of each data channel to get the 1/f noise spectrum by cross correlation in the case of ±45 ° method, or it calculates two power spectra and subtracts the results in the case of 0°-90° method. Our program for the real-time signal processing is written in assembly language. Table 3.3 shows an assembly code used in the implementation of a dual-channel digital lock-in-amplifier.

The performance of our system is demonstrated in figure 3.11. The noise measurements are obtained by averaging 128 runs (~ 35 minuites). Our system suppresses the background noise by a factor of 100, and substantially out-performs commercial analog lock-in amplifier. The limit is set by statistical errors due to the finite measurement time.

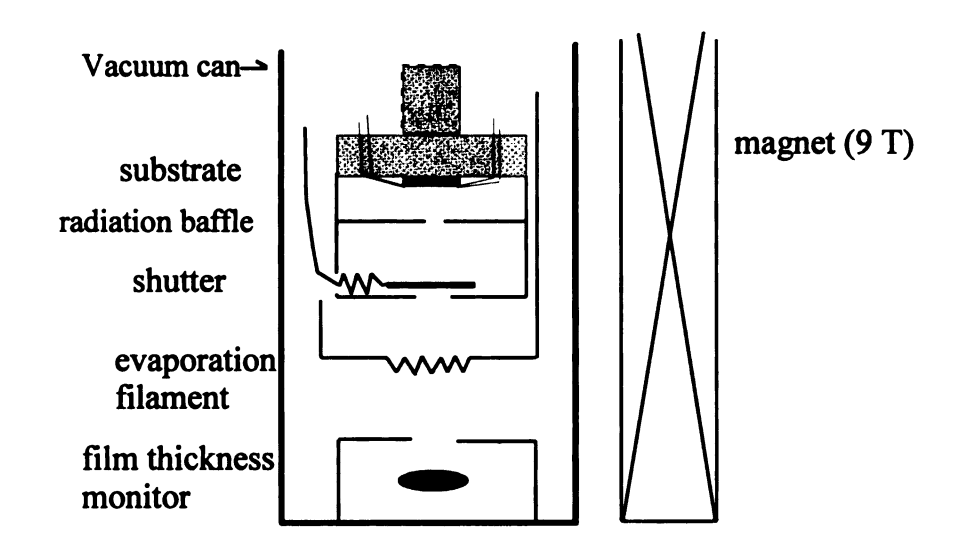
After we developed our DSP-based noise measurement system, Stanford Instruments introduced a commercial DSP lock-in amplifier which is convenient to vary the experimental set-up, for example, drive current and phase shift. We used a Stanford SR850 DSP lock-in for the actual noise measurements in this thesis. Since the Stanford DSP lock-in amplifier works as a voltmeter basically, the output signal is processed with the Iotech filter and digitizer to get a bandwidth-limited signal for the Fast-Fourier transform (FFT). The personal computer interfaced with Iotech instruments performs the FFT to extract the noise power.

References

- [1] N. Papanikolaou et al., Phys. Rev. Lett. 71, 629 (1993).
- [2] S. Feng, P. A. Lee, A. D. Stone, Phys. Rev. Lett. 56, 1960 (1986)
- [3] D. C. Flanders, Appl. Phys. Lett. 36, 93 (1980).
- [4] B. J. Lin, J. Vac. Sci. Technol. 12, 1317 (1975).
- [5] D. E. Prober et al., Appl. Phys. Lett. 37, 94 (1980).
- [6] A. N. Broers, J. M. E. Harper, and W. W. Molzen, Appl. Phys. Lett. 33,392 (1978).
- [7] R. E. Howard et al., J. Vac. Sci. Technol. **B1**, 1101 (1983).
- [8] R. E. Howard, E. L. Hu, and L. D. Jackel, Appl. Phys. Lett. 36, 141 (1980).
- [9] M. Hatzakis, J. Vac. Sci. Technol. 16, 1984 (1979).
- [10] G. J. Dolan and J. H. Dunsmuir, Physica B 152, 7 (1988).
- [11] B. J. Lin, and T. H. P. Chang, J. Vac. Sci. Technol. 16, 1669 (1979). B. D. Hunt, and R. A. Buhrman, J. Vac. Sci. Technol. 19, 1308 (1981).
- [12] J. H. Scofield, Rev. Sci. Instrum. 58, 985 (1987).
- [13] D. E. Prober, Rev. Sci. Instrum. 45, 849 (1974).
- [14] A. Van der Ziel, *Noise* (Prentice Hall, Englewood Cliffs, 1970); see also S. Demolder *et al.*, J. Phys. E **13**, 1323 (1980).
- [15] M. B. Weissman, Ph. D. Thesis, University of California, San Diege (1976); H. Stoll, Appl. Phys. 22, 185 (1980).
- [16] A. H. Verbruggen, H. Stoll, K. Heeck, and R. H. Koch, Appl. Phys. A 48, 233 (1989).
- [17]P. A. Probst and B. Collet, Rev. Sci. Instrum. 56, 466 (1985); N. O. Birge and S.
 R. Nagel, Rev. Sci. Instrum. 58, 1464 (1987); P. K. Dixon and L. Wu, Rev. Sci.
 Instrum. 60, 3329 (1989).

- [18] For an introduction to digital signal filtering, see Oppenheim and Schafer, Digital Signal Processing (Prentice-Hall, Englewood Cliffs, 1975).
- [19] For a discussion of multistage digital filtering, see R. E. Crochiere, *Multirate Digital Signal Processing* (Prentice-Hall, Englewood Cliffs, 1983).

Set-up for quench-condensation.



Substrate with metal stencil

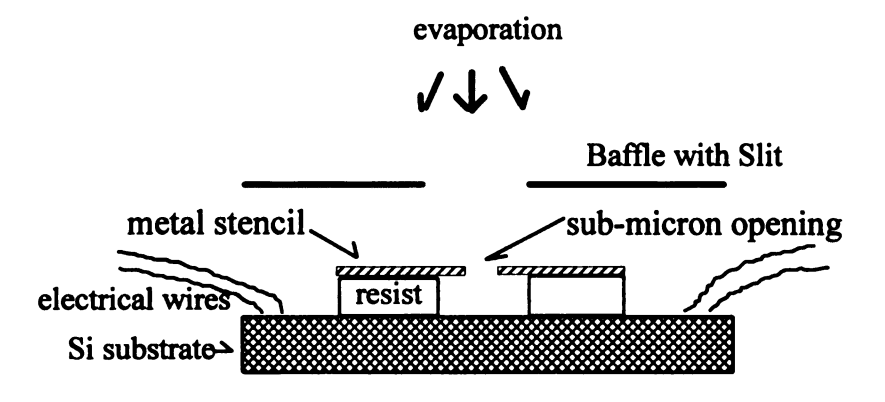


Figure 3.1 A schematic set-up for quench-condensation including (a) a cryoevaporator and (b) the substrate with sub-micron metal stencil mask.

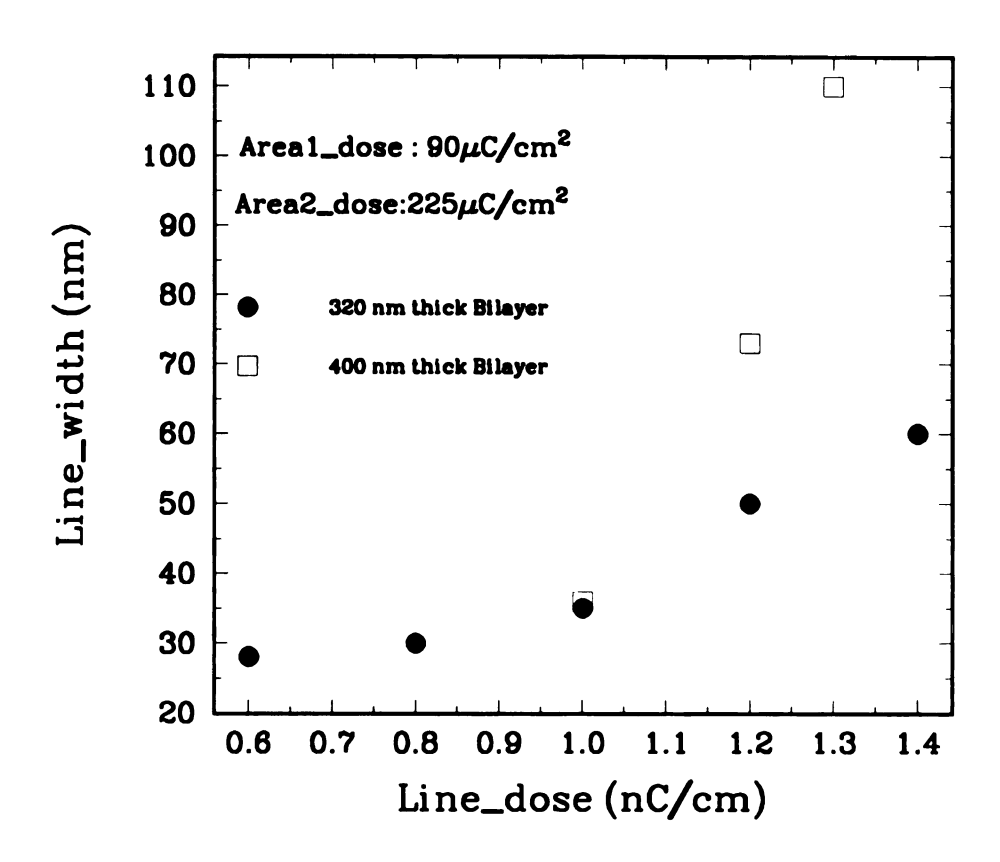


Figure 3.2 Line dose versus line width obtained by the bilayer electron-beam lithography. Thinning the resist gives the better control of line width well below 100 nm.

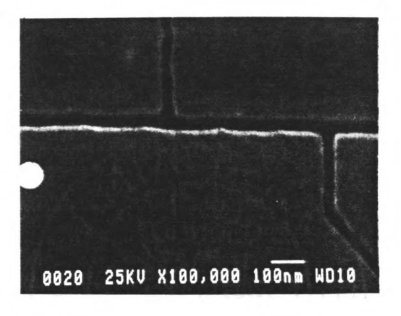
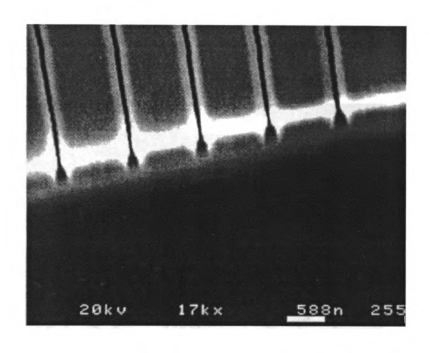


Figure 3.3 Scanning electron microscope photograph of the patterned bilayer resist itself. The developed lines are about 40 nm wide.



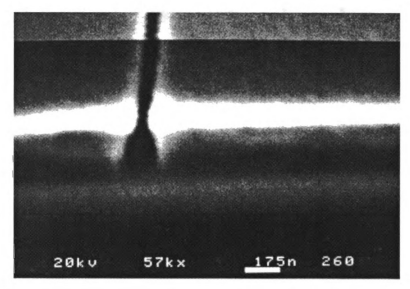


Figure 3.4 (a) The undercut profiles obtained from \sim 400 nm thick bilayer resist are shown. (b) Cross-section of the e-beam exposed line is shown with the \sim 80 nm deep undercut profile.

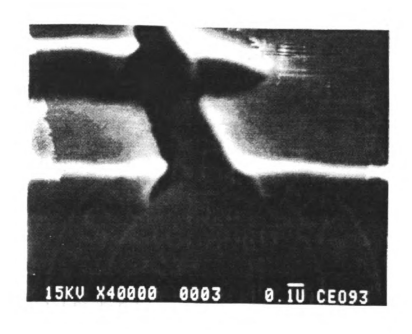


Figure 3.5 SEM photo of the area exposed by the area_dose, $225\mu C/cm^2$.

Trilayer Electron beam Lithography

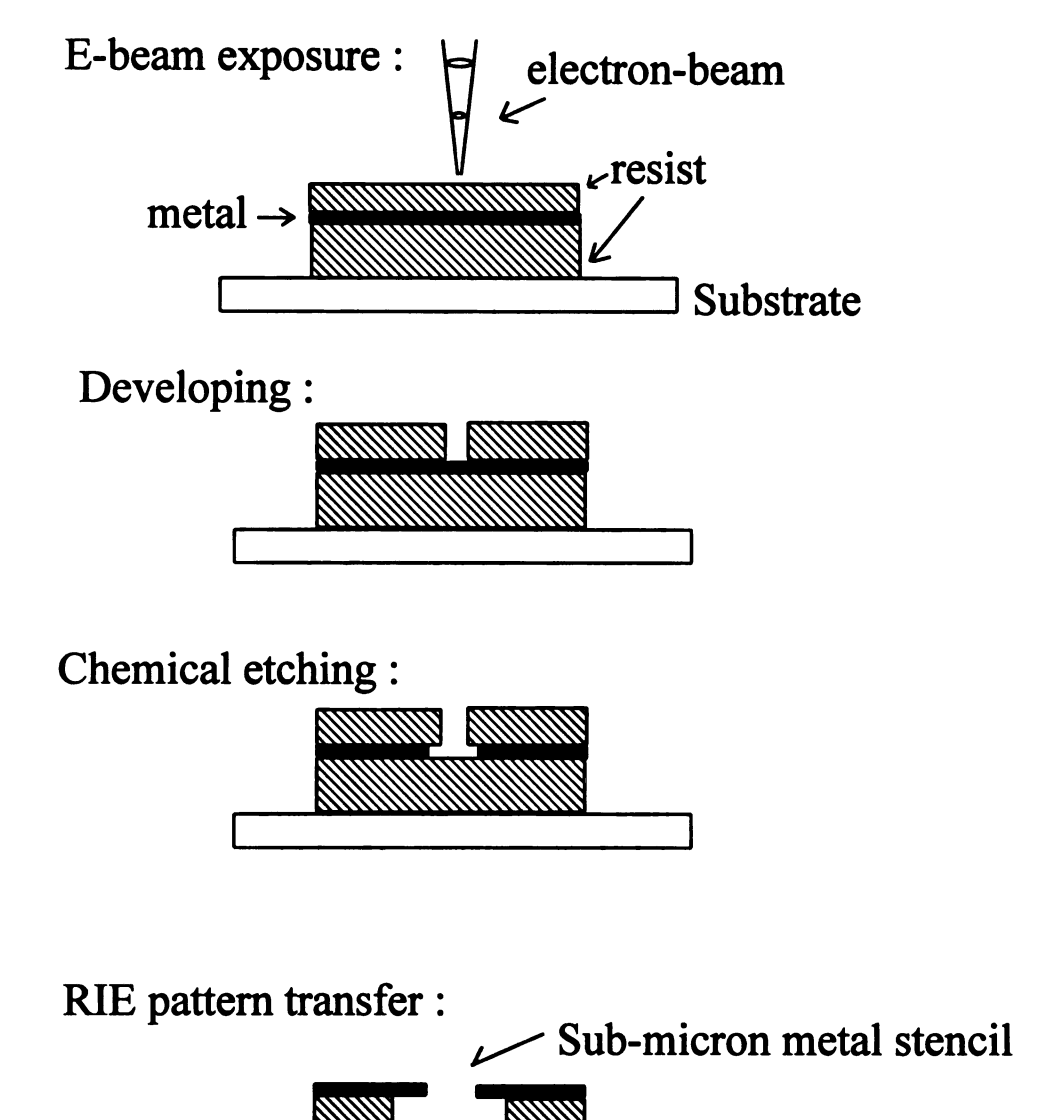


Figure 3.6 Schematic procedure of the trilayer electron beam lithography.

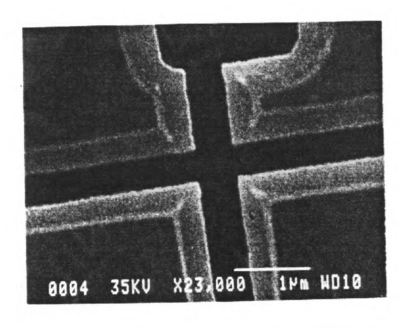




Figure 3.7 SEM photograph of a sub-micron metal stencil. (a) The top view shows the uniform undercut profile developed underneath of the metal stencil. (b) The side view shows the metal stencil on top of the resist.

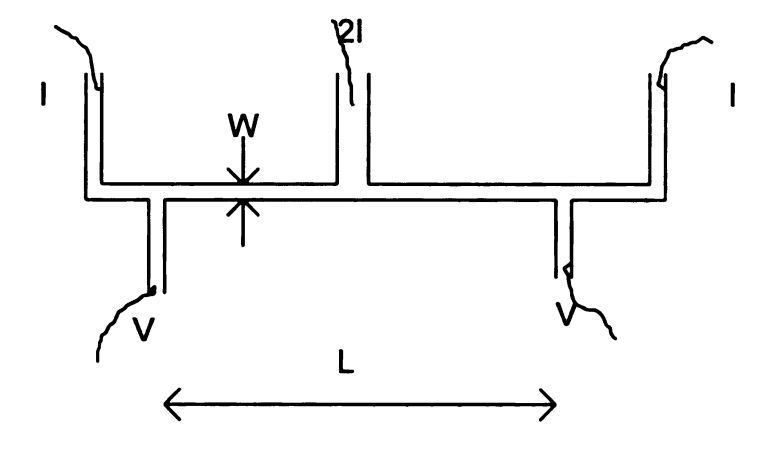
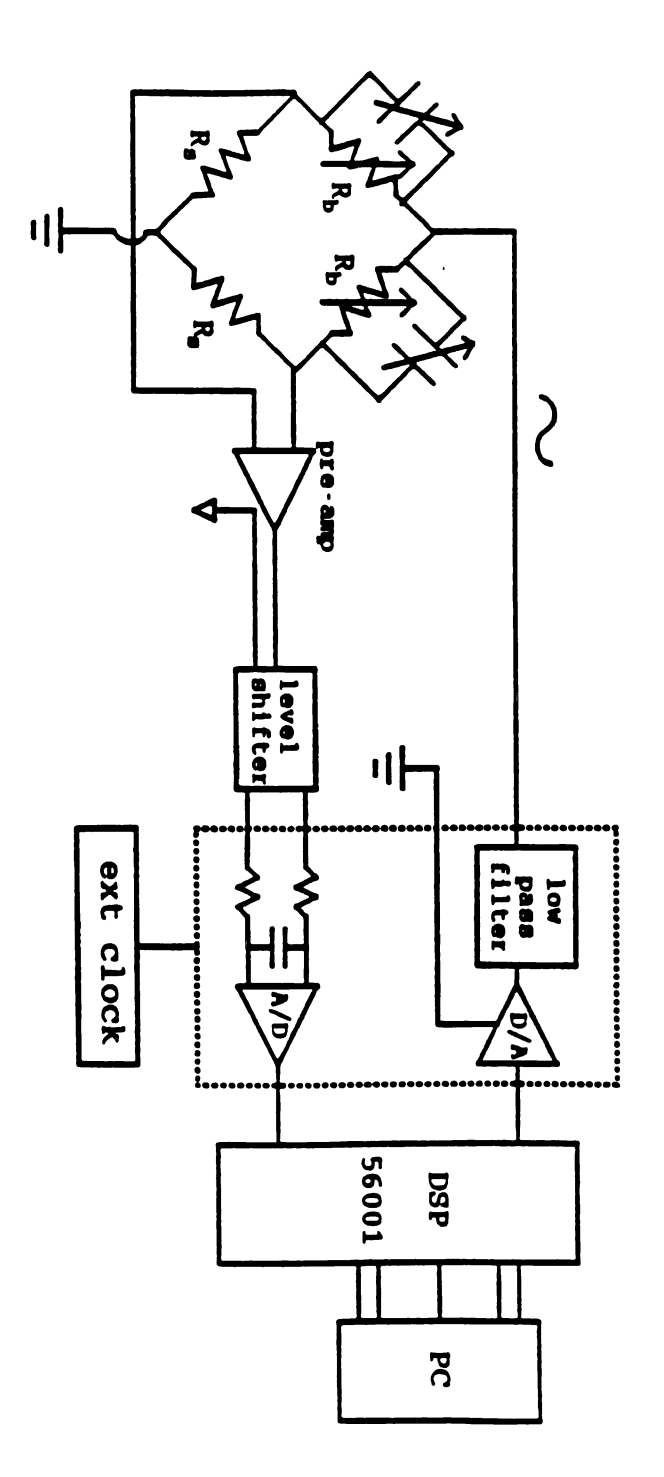


Figure 3.8 Schematic diagram of the sample geometry.



ballast resistors. the lower two arms of the Wheatstone bridge, while the upper arms are adjustable Figure 3.9 Schematic diagram of noise measurement system. The sample forms

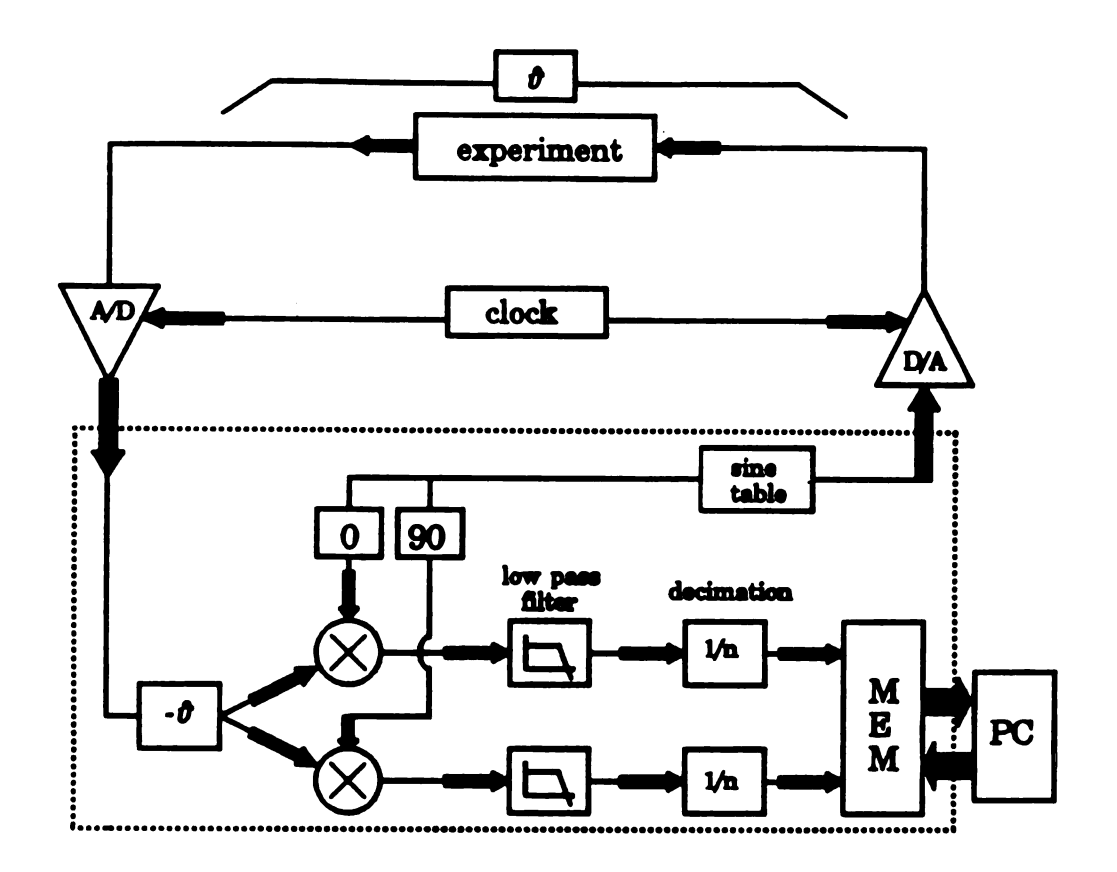


Figure 3.10 Block diagram of digital signal processing system. The mixing and digital filtering and decimation are performed in real time by the Motorola DSP 56001.

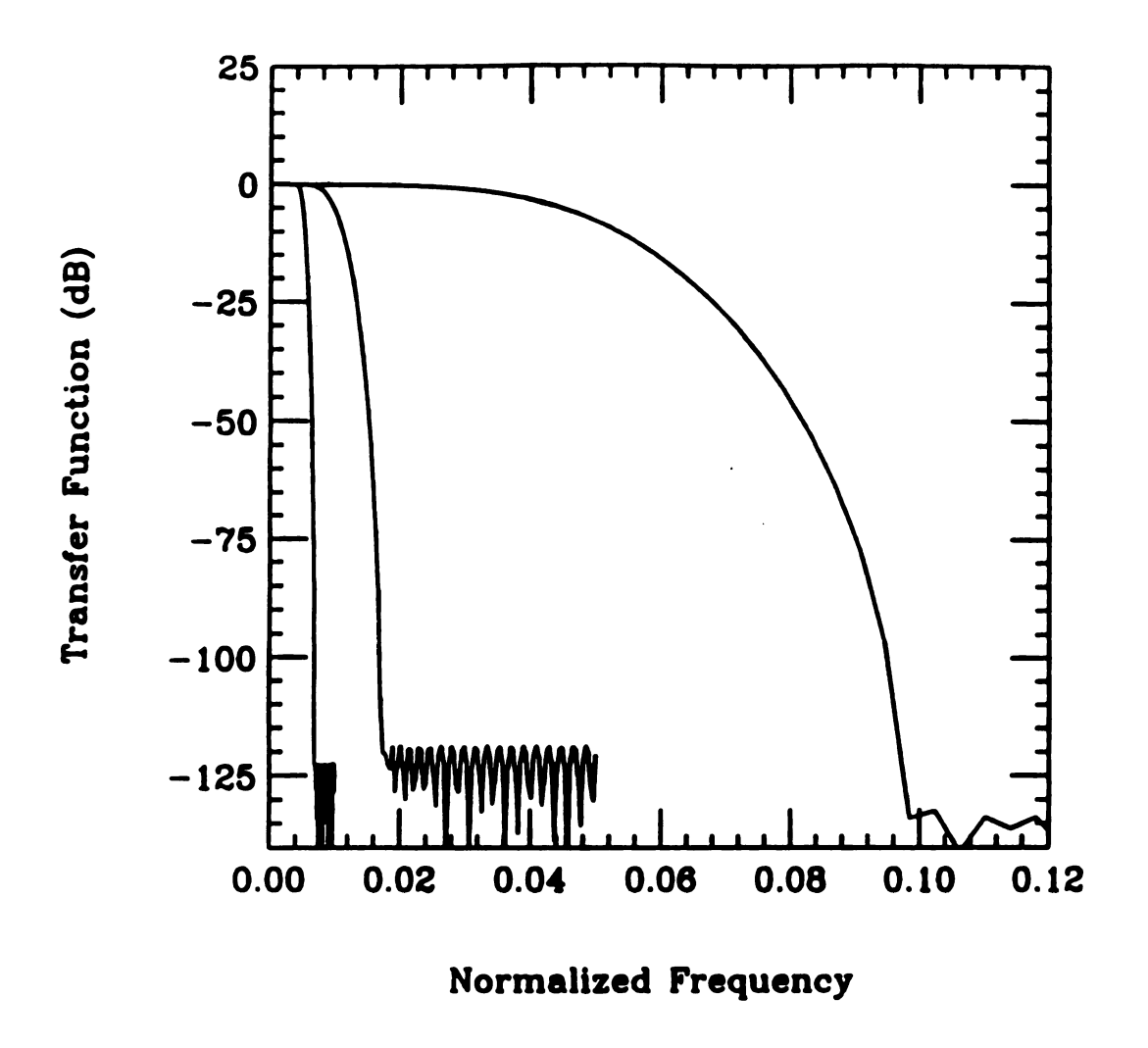


Figure 3.11 Transfer function of the three FIR digital filters preceding the three decimations. The frequency scale is referred to the original sample rate of 14.4 kHz before decimation. The sample rate is reduced by factors of 10, 5, and 2 in successive decimation stages.

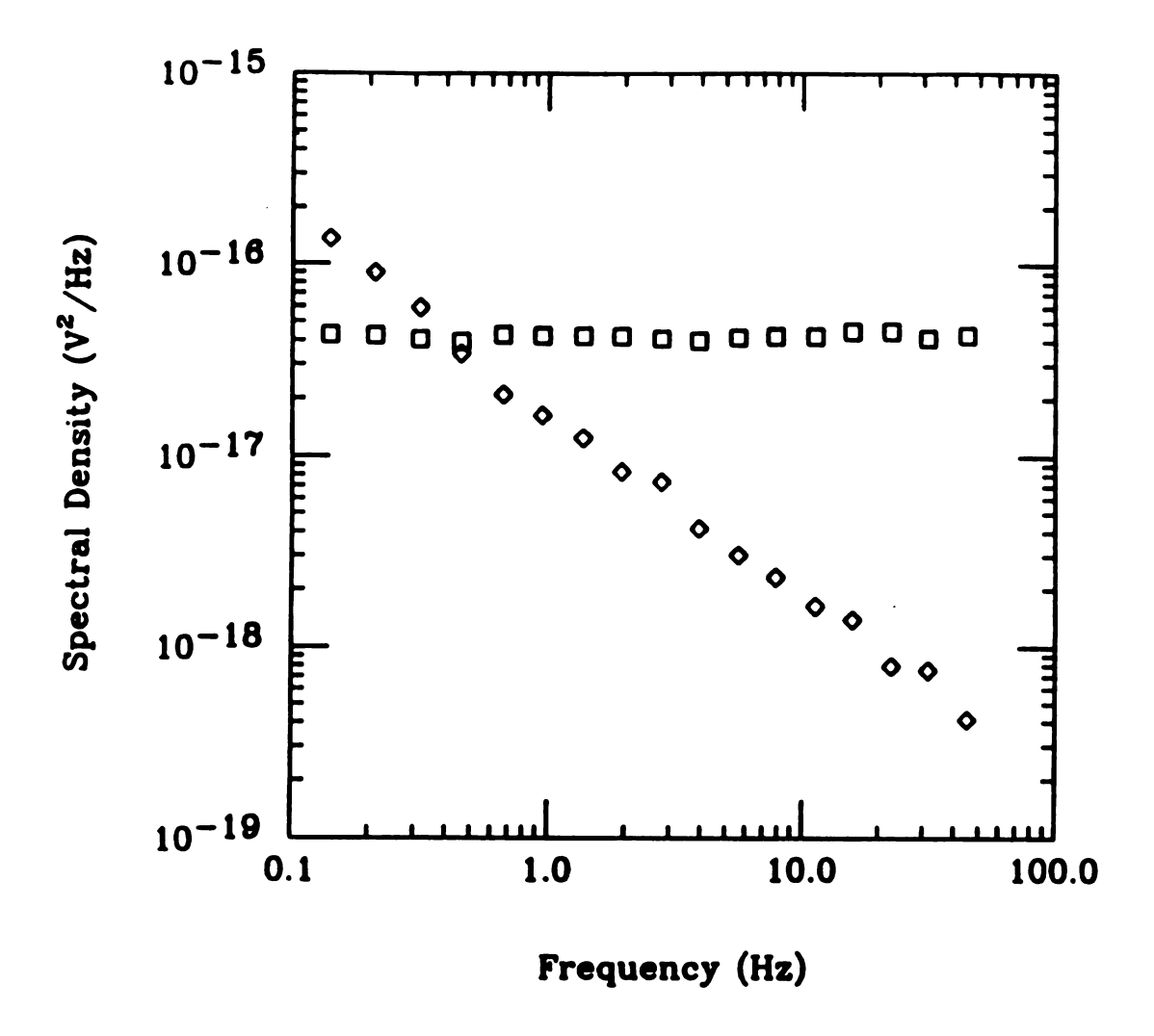


Figure 3.12 Noise measurements of a pair of 480- Ω carbon resistors. The background (\square) was measured with the 90 method, and the sample noise (\Diamond) was measured with the 45 cross-correlation method.

Table 3.4 The part of Assembly code for implementation of dual-phase lock-in amplifer using DSP 56000.

```
do
                      #prepts, predo
input 0
           jclr
                     #7,x:$ffee,input_0
           move
                     p:(r7)+n7,x1
           move
                      x1,x:$ffef
predo
           nop
           do
                      #pts,endo out
           do
                      #dec3, endo 3
           do
                      #dec2, endo 2
           do
                      #dec1, endo 1
input
           jclr
                      #7,x:$ffee,input
                      x:$ffef,x0
           move
                      #shift,n7
           move
                      p:(r7),x1
           move
                      x1,x:$ffef
           move
                      (r7) - n7
           move
                      #delta,n7
           move
                      x:(r7),x1
           move
           mpy
                      x1, x0, a
                      a,x:(r0)
                                  y: (r7) + n7, y1
           move
           mpy
                      y1,x0,a
                      #shift,n7
           move
           move
                      a, y: (r0) -
           move
                         (r7) + n7
endo 1
           nop
; perform
           first
                   filtering for each carriers
           move
                      (r0) +
calcs1
           clr
                            x:(r0)+,x0
                                          y: (r4) +, y0
                      #ntabs1-1
           rep
                                 x:(r0)+,x0 y:(r4)+,y0
           mac
                      x0,y0,a
           macr
                      x0, y0, a
           move
                      a,x:(r1)
calcc1
           clr
                           y:(r0)+,y1
                                          x: (r4) + , x1
           rep
                      #ntabs1-1
           mac
                      x1, y1, a
                                 y: (r0) + y1  x: (r4) + x1
           macr
                      x1, y1, a
                                   (r0) -
           move
                      a,y:(r1)-
endo 2
           nop
; perform second filtering for each carriers
           move
                      (r1) +
calcs2
           clr
                           x:(r1)+,x0
                                          y:(r5)+,y0
                      a
           rep
                      #ntabs2-1
                      x0,y0,a
                                 x:(r1)+,x0 y:(r5)+,y0
           mac.
           macr
                      x0, y0, a
           move
                      a,x:(r2)
calcc2
           clr
                           y:(r1)+,y1
                                          x:(r5)+,x1
           rep
                      #ntabs2-1
                                 y: (r1) +, y1  x: (r5) +, x1
           mac
                      x1, y1, a
                                   (r1) -
           macr
                      x1, y1, a
           move
                      a,y:(r2)-
endo 3
          nop
           ;perform third filtering for each carriers
           move
                      (r2) +
calcs3
           clr
                            x:(r2)+,x0
                                          y: (r6) + , y0
           rep
                      #ntabs3-1
                                x:(r2)+,x0 y:(r6)+,y0
           mac
                      x0, y0, a
```

Chapter 4 Zeeman effect on UCF

4A. Introduction.

In this chapter, we describe our electron transport measurements on a 1D metallic Li wire in the regime of negligible spin-orbit and spin-flip scattering, which has the feature of maximum symmetry (GOE)[1] in the absence of a magnetic field. Application of a magnetic field causes a transition from GOE to GUE, and hence a reduction of conductance fluctuations $(\delta G)^2$ by exactly a factor of 2. Application of a much larger field breaks the electron spin degeneracy and creates two independent eigenvalue sequences, thereby causing a second factor of 2 reduction. Our data show good agreement with the theory[2,3,4] for the complete crossover function, both for the GOE to GUE transition and for the splitting of the Zeeman degeneracy. Our results show that the magnetic field scale for the Zeeman crossover is determined by the sample temperature, rather than by the Thouless energy as has previously been suggested[3,5].

4B. Experiment.

We have studied metallic Li films for minimal spin-orbit (SO) scattering with sample dimensions in the quasi-1D regime (thickness t and width $W < L_{\phi}$) because this restricted geometry further enhances the noise power via UCF[6]. Samples were patterned with five leads on silicon substrates using electron-beam lithography and a trilayer resist/metal/resist structure as discussed in Chapter 3. The lateral dimensions of the sample were $0.44 \times 20 \ \mu\text{m}^2$ as determined from a scanning electron microscope (SEM) picture before the sample was loaded into the ⁴He cryostat. The Li film was quench-condensed *in-situ* at 4.2 K through the metal stencil, then annealed at 35 K. The low-temperature sheet resistance was $0.46 \ \Omega$. The film thickness was obtained at

the conclusion of the experiment by a comparison of the linear temperature dependence of the resistance above 80 K, shown in figure 4.1, with that of bulk lithium[7]. By this method, we estimated the thickness of the film to be 54 nm. This implies $l_e = 40 \text{ nm}$, $k_F l_e = 450 \text{ with free-electron values for the electronic constants.}$ The resistance and resistance fluctuations (1/f noise) were measured using a low frequency ac bridge method[8], with a liquid-nitrogen cooled Triad G-5 transformer to increase the sample-to-preamplifier noise ratio. To compensate for possible background fluctuations during the 1/f noise measurement, the total noise (1/f noise + background) and the background were measured simultaneously with a two-phase digital lock-in amplifier. Figure 4.2 demonstrates the sensitive detection of the 1/f noise with a large background. In this measurement, background noise is mostly from Johnson noise of the cooled transformer.

A magnetic field perpendicular to the film was provided by a 9 T superconducting magnet in the liquid He bath outside the vacuum can. We measured the 1/f noise as a function of magnetic field at two fixed temperatures, 1.6 K and 4.2 K.

4C. Magnetoresistance measurement.

Figure 4.3 shows the magnetoresistance at different temperatures and the fit based on one-dimensional weak localization theory[9]. (The fits were done with $\tau_{so}^{-1}=0$.) Figure 4.4 illustrates the effect of SO scattering rate in the fit. Fits to these data provide an upper bound on the SO scattering rate of $\tau_{so}^{-1}<0.2\cdot\tau_{\phi}^{-1}$ at 1.6 K; hence we are always in the low SO scattering limit. Since the 1D weak localization correction to the magnetoresistance depends on the width of the sample, it gives another estimate of film width, W \approx 0.45 μ m, close to the SEM observation. L_{ϕ} is 1.4 μ m and 0.75 μ m at 1.6 K and 4.2 K, respectively, hence the sample is quasi-1D (L_{ϕ} > W).

Figure 4.5 shows the temperature dependence of the electron phase breaking length, L_{ϕ} assuming no spin-dependent scattering in the magnetoresistance fits. The straight line, $L_{\phi}^{-2} = (0.096T^2 + 0.20)\mu\text{m}^{-2}$, is a linear least-squares fit to the data. This linear behavior, although unusual for metal films, has been observed previously for Li films over a wide temperature range[10] and will be discussed further in Chapter 5. We believe that the finite intercept at T=0 arises from the presence of a small amount of spin-dependent scattering (either spin-orbit or spin-flip)[10].

4D. 1/f noise measurement.

Figure 4.6 illustrates the 1/f noise power spectra at 1.6 K at three different values of magnetic field; B = 0 T, 1.0 T, 8.8 T. At least 64 simultaneous spectra for total noise and background were averaged to reduce the statistical uncertainty at each data point. The relatively large error bars at high frequencies are due to the error propagation from the background subtraction. The straight lines are least-squares fits to a power law. The noise slopes are very close to -1.0 ± 0.03 at all values of magnetic field. The data in fig. 4-6 demonstrate clearly that the amplitude of the 1/f noise power drops as the magnetic field increases.

4D-1 Quantitative analysis of GOE-GUE crossover

Figure 4.7 shows the relative 1/f noise power at 0.1Hz as a function of the perpendicular magnetic field at temperatures of 1.6 K and 4.2 K. The relative noise power at 1.6 K shows a first reduction to 1/2 with characteristic field $B_{c1} \approx 22$ G, where B_{c1} is defined as the field where the noise is 3/4 of its zero-field value. B_{c1} is temperature dependent, increasing to 34 G at 4.2 K. B_{c1} corresponds to the penetration of a flux quantum through a phase coherent region, $B_{c1} = A \frac{h/e}{L_{\phi}W}$ for a quasi-1D sample, where A is a numerical constant that depends weakly on the ratio of

 $L_{\phi} = \sqrt{D\tau_{\phi}}$ to $L_T = \sqrt{\hbar D/k_B T}$, where $D = v_F l_e/3$ is the electronic diffusion constant. For this film, D is $7.8 \times 10^{-3} \, \text{m}^2/\text{s}$ and the L_T is $0.17 \, \mu \text{m}$ at $1.6 \, \text{K}$.

For a detailed comparison of theory and experiment, we use Eq. (2-31) for the GOE-GUE crossover function. (See Chapter 2 for the details.) For pure UCF fluctuations, one would expect Eq.(2-31) to describe the low-field data in figure 4-7, with L_{φ} as the only free parameter. We observe, however, that the noise does not quite drop a full factor of 2. A similar behavior is observed in other Li samples, shown in figure 4.8, and in Ag films[11], and apparently arises from a small contribution of local interference (LI) type noise[12] that is magnetic field independent. We therefore include a second parameter to account for this small effect. The function fitted to the data is:

$$\frac{S_G(B)}{S_G(0)} = c + (1 - c)v(B) \tag{4-1}$$

where $\nu(B)$ is given by Eq. (2-31). The solid line in figure 4-7 shows the fit to the data for B < 0.1 T. The fit yields c=0.1 and 0.2 and L_{ϕ} =1.0 μ m and 0.65 μ m at 1.6 K and 4.2 K, respectively. The latter are remarkably close to the values 1.3 μ m and 0.75 μ m obtained from magnetoresistance measurements taken at the same drive level as the noise measurements. (The noise measurements at 1.6 K were taken with a drive level that caused sample heating to about 1.9 K, as determined from the magnetoresistance.)

4D-2 Quantitative analysis of Zeeman crossover

As the magnetic field increases above 1 T, the noise power begins a second decrease. At 1.6 K, the characteristic field scale for this second drop is $B_{c2} \approx 4$ T, with saturation at about 7 \sim 8 T. The solid line at high field in fig. 4.7 is our

numerical evaluation of the noise crossover function, Eq. (2-38), for the Zeeman effect, valid for $B >> B_{c1}$. In this computation, we use our experimental values for D, k_BT , and L_{ϕ} , and the free electron value of the g-factor (=2). We emphasize that there are *no free parameters* in the theory for the Zeeman splitting; the constant c in Eq. (4-1) was already determined by the fit to the low-field data.

It is of interest to ask whether the Zeeman crossover occurs when E_Z exceeds the Thouless energy, $E_C = \hbar D/L_\phi^2$ or the temperature, $k_BT[3,4]$. At 1.6 K, the value of E_C/k_B in our sample is about 59 mK, about 30 times smaller than the temperature; hence we can clearly distinguish which of these two energies governs the Zeeman crossover. In the former case, $B_{c2} \approx \frac{E_C}{g\mu_B} = 0.04$ T, which is clearly incompatible with the data. (The uncertainty in our estimation of D due to uncertainty in the film thickness is not enough to account for the discrepancy). In the latter case, $B_{c2} \approx \frac{k_B T}{g\mu_B} = 1.5$ T, which is not far from the experimental value $B_{c2} \approx 4$ T. When the correct numerical prefactor is put in, we indeed find the excellent agreement between theory and experiment shown in fig. 4-7. The result holds only in the regime $k_B T >> E_C$; numerical evaluation of the theoretical crossover function shows that it is always the larger of the two energies that governs the Zeeman crossover.

4E. Comparison with earlier work.

Mailly et al. [13] measured the variance of conductance jumps induced by applied voltage pulses in GaAs/AlGaAs heterojunctions at zero magnetic field and 0.2 T. At 50 mK, a decrease in the variance by a factor of 3 was observed at 0.2 T.

Debray et al. [5] studied UCF using a static method in a quasi-1D GaAs/AlGaAs heterostructure. They measured the conductance variance at sample temperature 1.3 K at several values of magnetic fields from 0 to 0.4 T and observed a first reduction of $(\delta G)^2$ by a factor of 2 below B ~ 0.001 T (with one data point!), and then a second

factor of 2 reduction near B \sim 0.06 T. They estimated the Thouless energy as $E_c \approx 88$ mK and concluded that the field scale for the Zeeman crossover is determined by the Thouless energy and the measured field scale is consistent with the theoretical prediction by Stone[3]. We mention that (1) they couldn't fit the magnetoresistance, which provides the phase breaking length and an estimate of the Thouless energy, (2) there are no data points showing the crossover regime of the first reduction in the variance due to the suppression of the cooper channel, and (3) most of all, we found that the prediction by Stone is wrong! (See Chapter 2 for further discussion on the field scale of the Zeeman crossover.) If we accept that their measurement is correct, then they observed a reduction by a factor of 4 in the relative UCF amplitude with the value of $B_{c2} \sim 0.02$ T, using our definition of B_{c2} as the midway point of the second reduction. Also, since $k_BT \gg E_c$, they should get $B_{c2} = 2.7k_BT/(g\mu_B) = 2.6$ T, which is about 100 times larger than the value observed. The value of B_{c2} above is calculated with the free electron value of g(=2). We note that several values of gfactor,~ 0.4[14] and 13[15], in GaAs/AlGaAs heterostructure have been reported. It is, however, unlikely that the g-factor in GaAs is ~100 times the free electron value. An important difference between those measurements and ours is that the GaAs experiment measures the saturated UCF amplitude, rather than unsaturated 1/f noise. But our numerical evaluation of the Zeeman crossover function for the saturated case also shows that B_{c2} is determined by the larger of k_BT and E_c . Therefore, we find it difficult to believe that their measurement and analysis were carried out correctly.

References

- Y. Imry, Europhys. Lett. 1, 249 (1986); P. A. Mello, Phys. Rev. Lett. 60,1089 (1988); K. A. Muttalib, J.-L. Pichard, and A. D. Stone, Phys. Rev. Lett. 59, 2475 (1987).
- [2] B. L. Al'tshuler and B. I. Shklovskii, Zh. Eksp. Teor. Fiz. 91, 220 (1986) [Sov. Phys. JETP 64, 127 (1986)], P. A. Lee, A. D. Stone, and H. Fukuyama, Phys. Rev. B 35, 1039 (1987).
- [3] A. D. Stone, Phys. Rev. B 39, 10736 (1989).
- [4] S. Feng, Phys. Rev. B 39, 8722 (1989). The calculation of the full crossover function for 1D was sent to us by Feng, private communication.
- [5] P. Debray, J.-L. Pichard, J. Vicente, P. N. Tung, Phys. Rev. Lett. 63, 2264 (1989).
- [6] S. Feng, P. A. Lee, A. D. Stone, Phys. Rev. Lett. 56, 1960 (1986).
- [7] J. S. Dugdale, D. Gugan, and K. Okmura, Proc. Roy. Soc. London, Ser. A 263, 407 (1961).
- [8] J. H. Scofield, Rev. Sci. Instrum. 58, 985 (1987).
- [9] B. L. Al'tshuler and A. G. Aronov, Pis'ma Zh. Eksp. Teor. Fiz. 33, 515 (1981)
 [JETP Lett. 33, 499 (1981)].
- [10] J. C. Licini, G. J. Dolan, and D. J. Bishop, Phys. Rev. Lett. 54, 1585 (1985).
- [11] Extensive low-temperature noise measurement on Ag films by our group show that the local interference contribution to the noise becomes significant (10 %) in both metals when L_φ/l_e ≈ 25. See also, P. McConville and N. O. Birge, Phys. Rev. B 47, 16667 (1993).
- [12] J. Pelz and J. Clarke, Phys. Rev. B 36, 4479 (1987).
- [13] D. Mailly, M. Sanquer, J.-L. Pichard, and P. Pari, Europhys. Lett. 62, 195 (1989).
- [14] S. Narita et. al, Jpn. J. Appl. Phys. Part 2 20, L447 (1981).

[15] C. Weisbuch and C. Hermann, Phys. Rev. B 15, 816 (1977); M. Dobers, K. v. Klitzing, and G. Weimann, Phys. Rev. B 38, 5453 (1988).

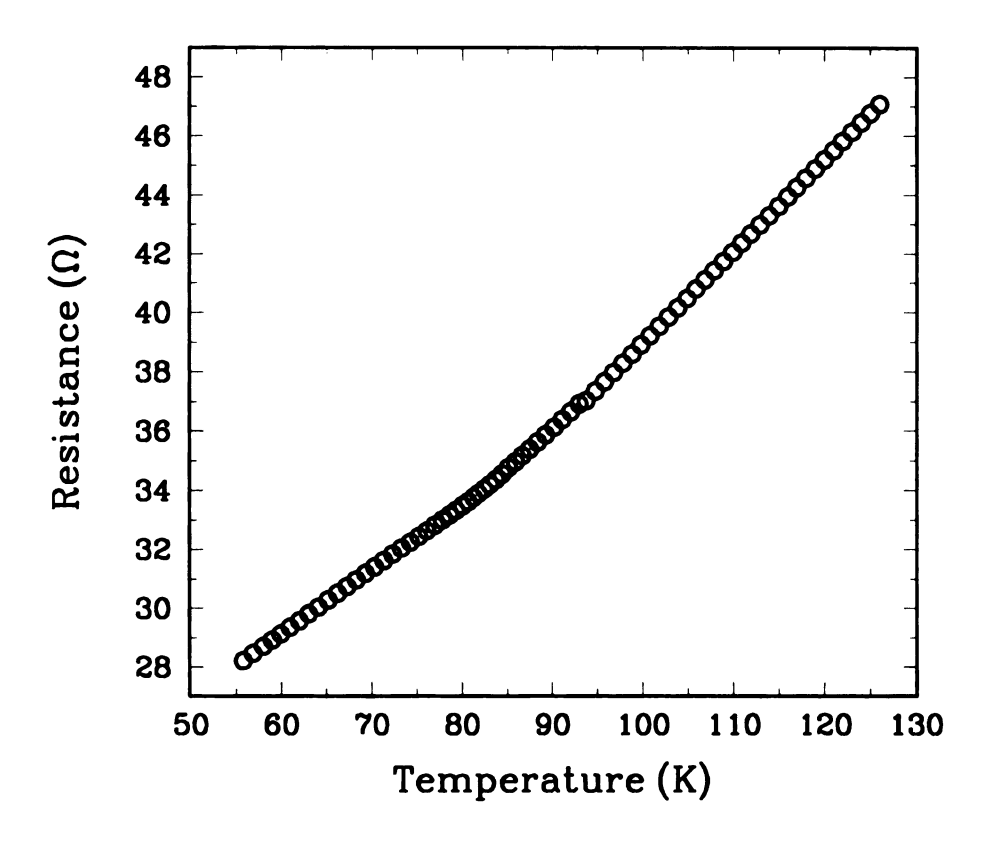


Figure 4.1 Sample resistance versus temperature obtained from quasi-one-dimensional metallic Li wire. The change in the linear temperature coefficient of the resistance is shown around 83 K due to martensitic structural transformation. We compare the linear temperature dependence of the resistance above 90 K with that of bulk lithium.

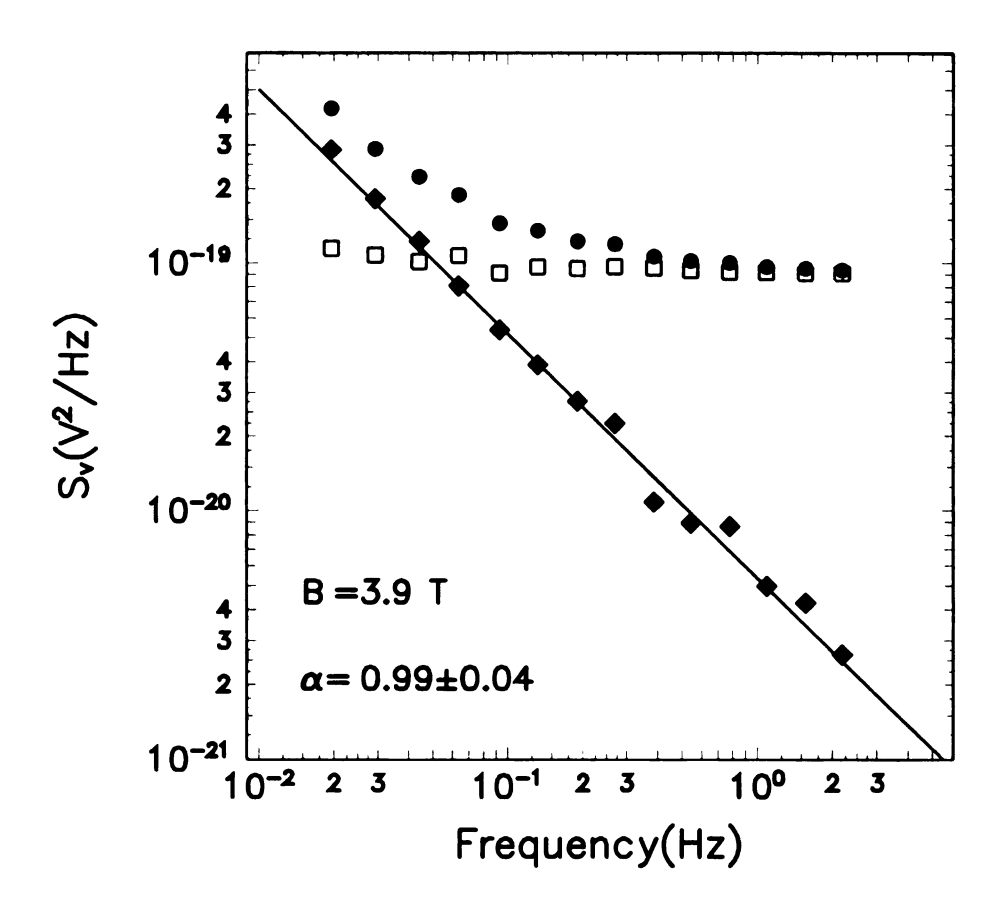


Figure 4.2 1/f noise power spectrum and background Johnson noise obtained simultaneously by two-phase digital lock-in amplifier. The spectral slope α is 0.99 \pm 0.04.

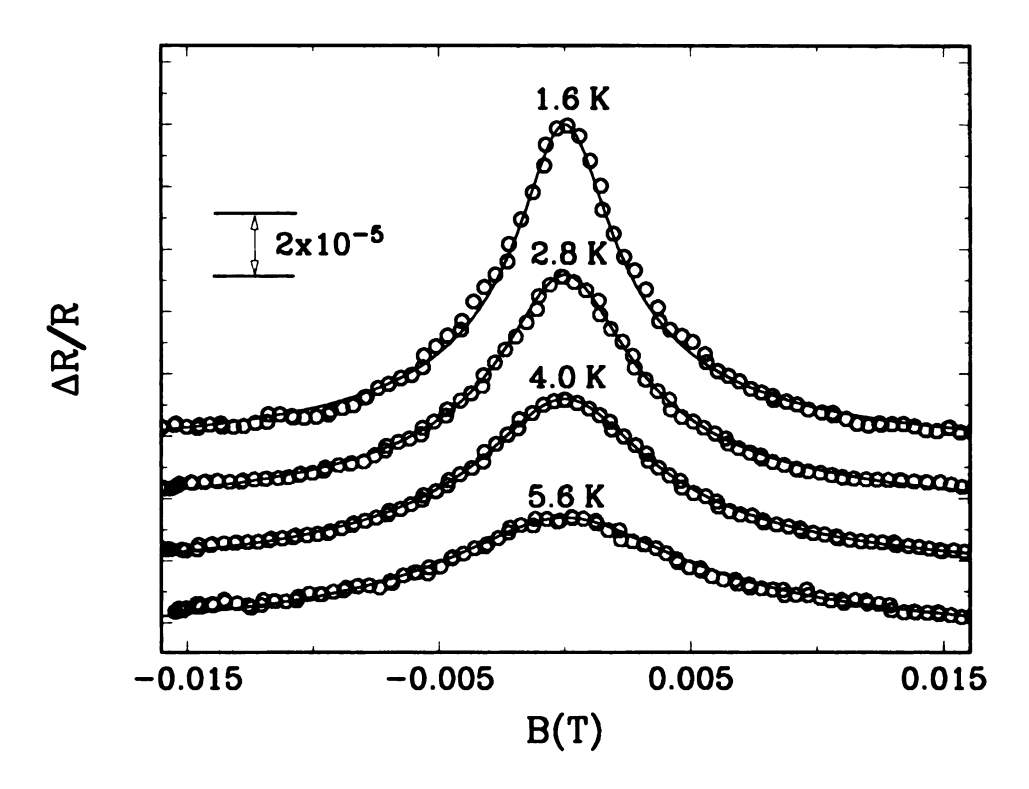


Figure 4.3 Magnetoresistance data at temperature, T = 1.6 K, 2.8 K, 4.0 K and 5.6 K. The solid line is the fit to the quasi-1D weak-localization theory with zero spin-orbit scattering.

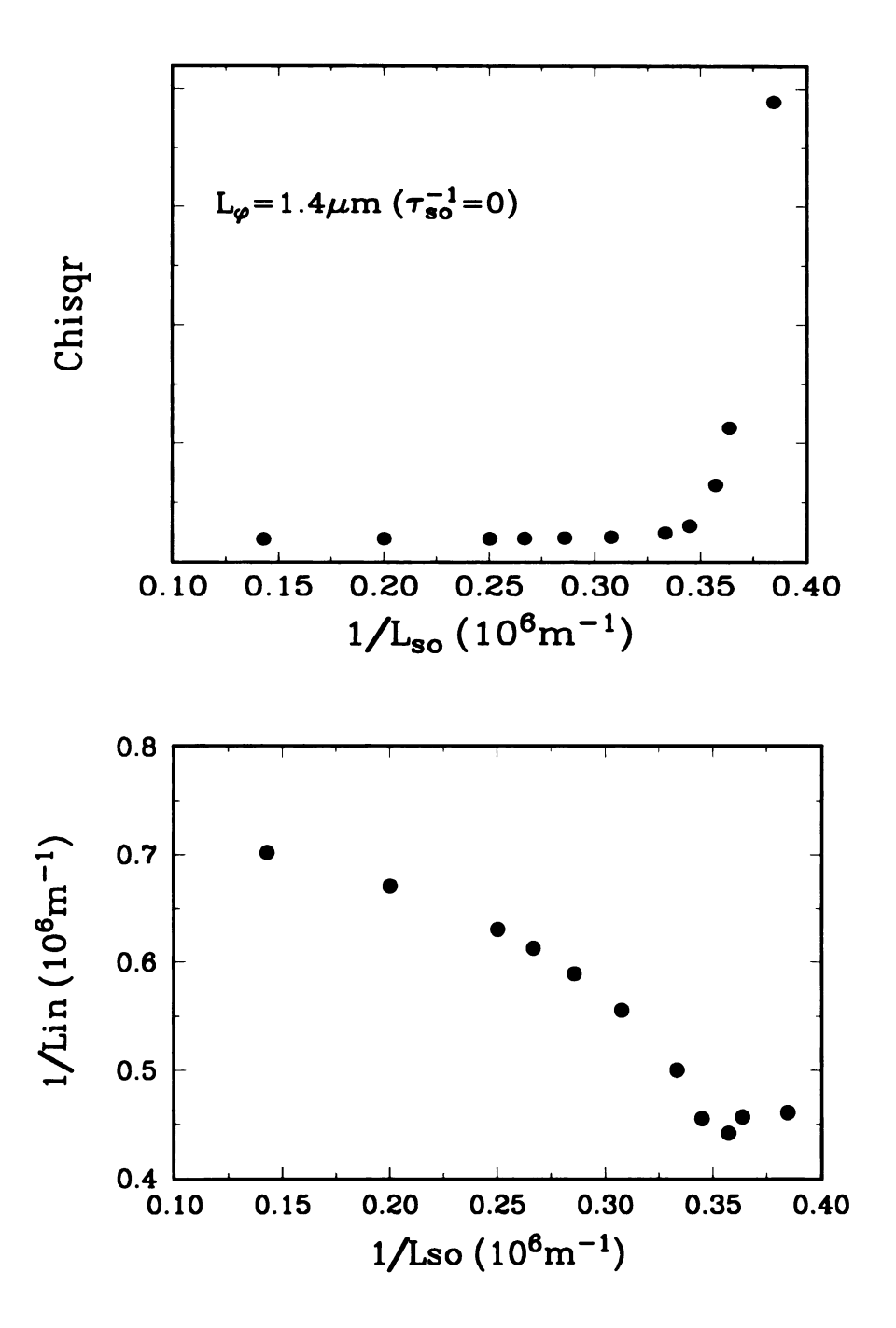


Figure 4.4 (a) The values of $\chi 2$ in the fit of the magnetoresistance data at 1.6 K as a function of the spin-orbit scattering rate assumed in the fit. The upper bound of spin-orbit scattering is set to be $\sim 0.2 \, \tau_{\varphi}^{-1}$. (b) the phase breaking length as a function of L_{so} .

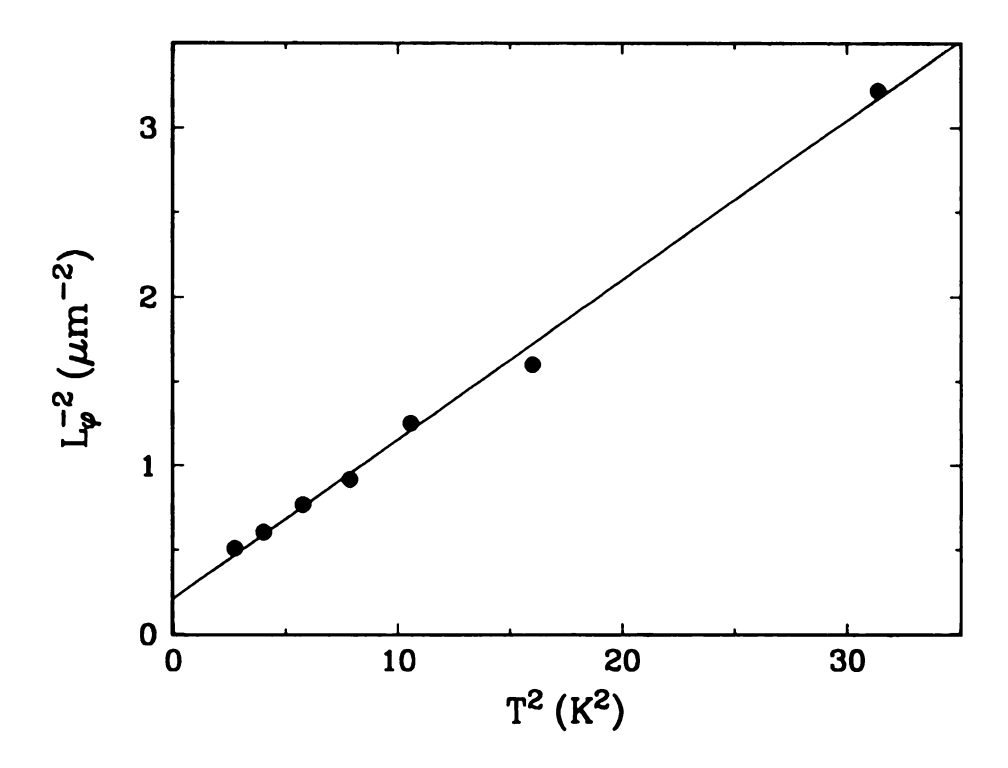


Figure 4.5 The electron phase breaking length versus temperature, obtained from the weak-localization fits of low field magnetoresistance.

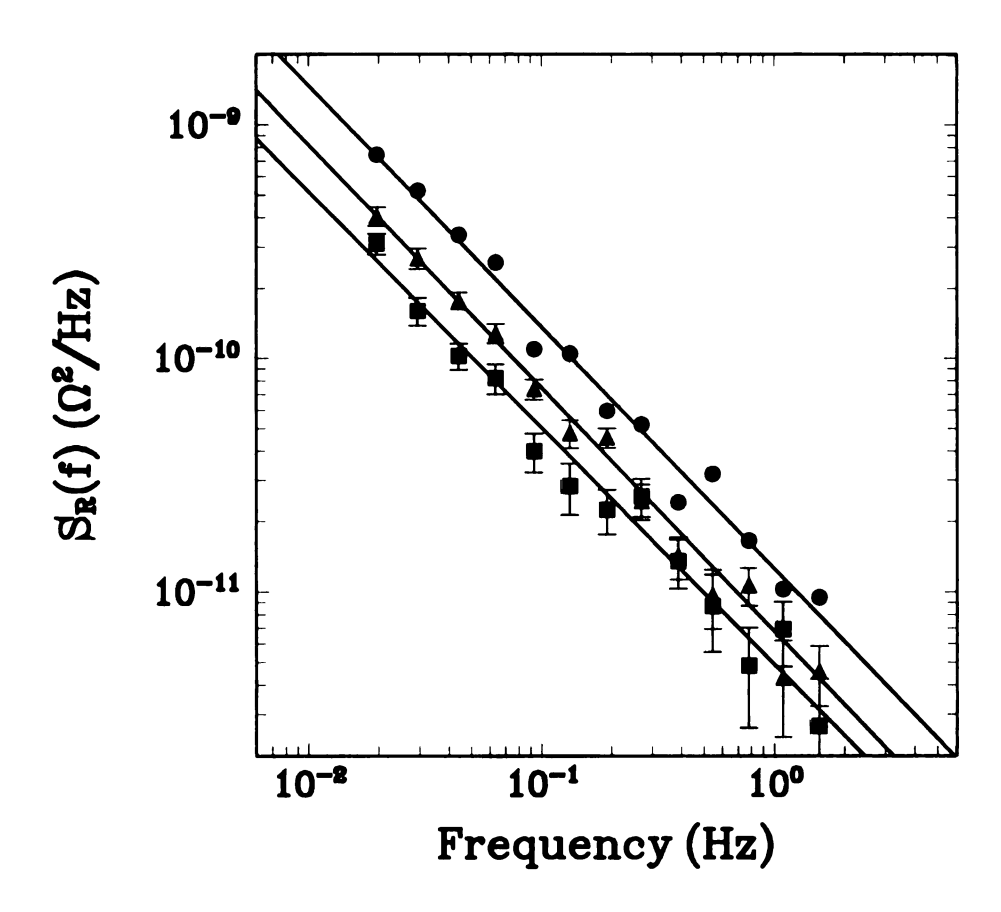


Figure 4.6 The resistance noise power spectra, $S_R(f)$, versus frequency at 1.6 K with fits to a power law, at three values of magnetic field, B = 0 T (\bullet), 1.0 T (\blacktriangle) and 8.8 T(\blacksquare). The spectral slopes for the three data sets are -1.03, -1.04, -1.01, respectively, with an uncertainty of ± 0.03 .

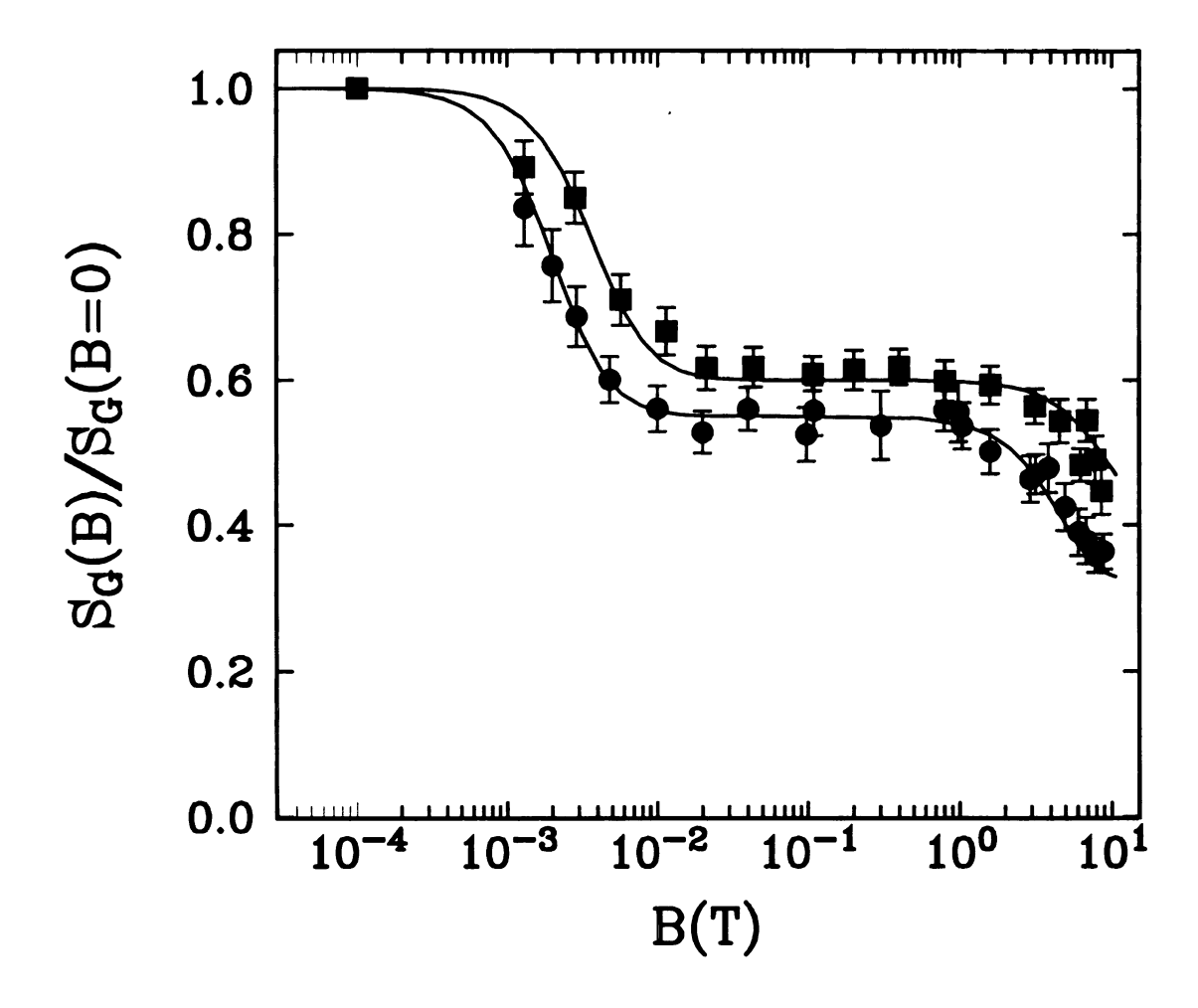


Figure 4.7 Conductance noise power, $S_G(0.1Hz)$, as a function of magnetic field at 1.6 K(•) and 4.2 K(•). The data are normalized by the noise power at zero field. The solid line is the theoretical expression for the noise crossover function. The theory for the low-field crossover is fit to the data with two free parameters, L_{φ} and c, as discussed in the text. The theory for the high-field crossover has no free parameters.

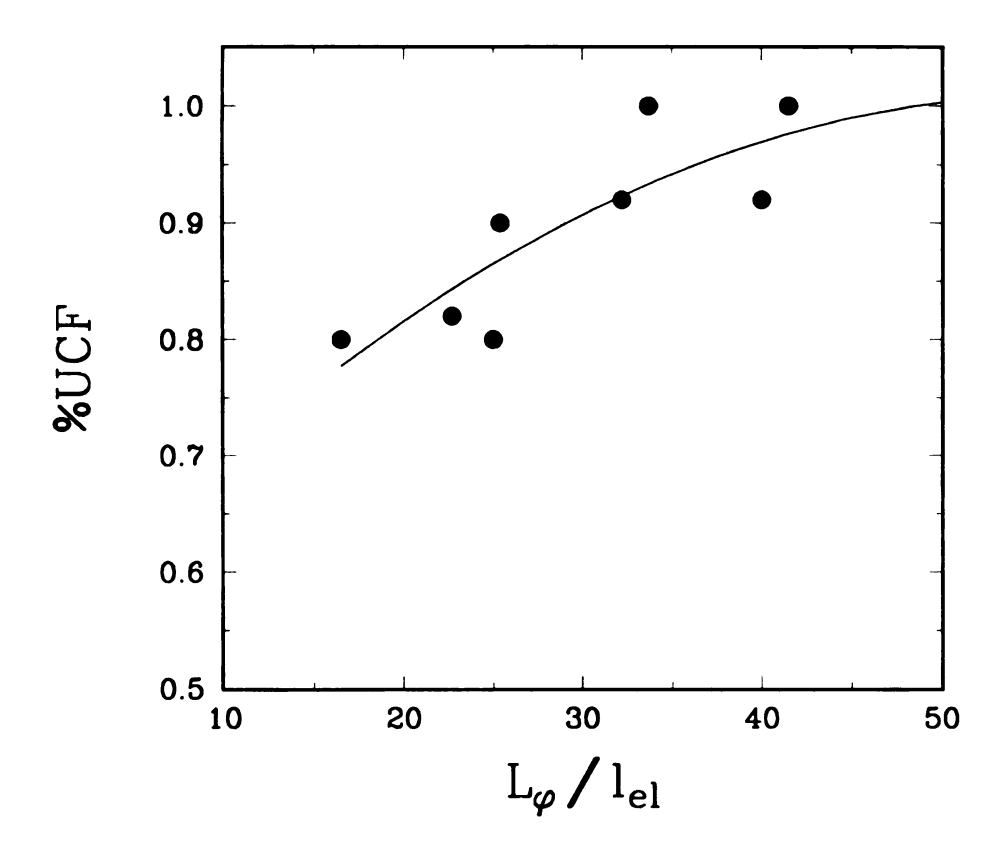


Figure 4.8 Contribution of %UCF to total noise power versus L_{φ}/l_e in Li samples. The contribution of local interference type noise becomes significant (10%) when $L_{\varphi}/l_e \approx 25$.

Chapter 5

SPIN-FLIP SCATTERING on UCF

5A. Introduction

In mesoscopic systems, the electrical conductance depends on the microscopic configuration of scatterers due to long-range quantum interference[1]. If the scatterers have free spin states (for example, paramagnetic impurities), then conduction electrons will experience the exchange interaction with the paramagnetic impurities, leading to relaxation of the electron spin states by spin-flip scattering[2]. Spin-flip scattering breaks the phase coherence and reduces the amplitude of conductance fluctuations. This picture is valid in a magnetic field that is not strong enough to align the impurity spins. When $\mu_{imp}B > k_BT$, spin-flip scattering is suppressed and the system behaves similarly to one without magnetic scattering. The magnetic scattering effect on weak localization[3] and conductance fluctuations[4] has been observed recently.

In this chapter, we report a quantum transport experiment on quasi-1D Li wires with a finite spin-flip scattering rate which is comparable to the electron phase breaking rate. The magnetoresistance measurement shows low-temperature residual scattering and suppression of the phase coherence. The 1/f noise measurement versus magnetic field shows that the phase coherence is recovered at high magnetic field causing a dramatic increase of conductance fluctuations. The noise power at low magnetic field shows a reduction by a full factor of 2. These observations are consistent with the effect of paramagnetic scattering on UCF.

5B. Experiment

Our samples were patterned with five leads on silicon substrates using electron-beam lithography on a bilayer resist structure, PMMA/Copolymer. The characteristics of the samples are summarized in Table 3.3. In this chapter, we discuss samples #1 - 4, which show the residual magnetic scattering. We presume that magnetic impurities such as Cr from the Ni-Cr filament wire contaminated the samples since Cr impurities in a Li matrix can be strongly magnetic[5]. The Li films were quench-condensed as described in Chapter 3 and magnetoresistance and 1/f noise were measured in-situ.

5C. Weak localization[6,7]

The inelastic scattering of conductance electrons comes from several mechanisms: electron-electron and electron-phonon scattering. The electron-electron scattering rate in a clean metal is determined by collisions with energy transfer of order of the temperature and momentum transfer of the order of the inverse screening length, which leads to a T^2 dependence, independent of the sample dimensionality. In disordered systems, the electron-electron scattering rate depends on the dimensionality of the sample which is set by the thermal diffusion length. In the 2D case, the electron-electron scattering rate is dominated by small energy transfer collisions, leading to a linear temperature dependence. Experimental observation of the dependence $\tau_{in}^{-1} \propto T$ are generally agreed to be due to the 2D electron-electron interaction. If the film is three dimensional with respect to electron-electron interaction one expects $\tau_{in}^{-1} \propto T^{3/2}$.

The electron-phonon scattering is governed by the electron-phonon interaction and leads to a T^d dependence in the clean-limit with dimensionality d. In dirty metals where $q_T l_e = \frac{k_B T}{\hbar S} l_e << 1$, where S is the velocity of sound, impurity scattering

causes the electron-phonon interaction to change and yields the different temperature dependence of the electron-phonon scattering rate: T^4 [8], or T^2 [9]. Thus, understanding the electron-phonon scattering requires more careful comparison between experiment and theory. Several experimental factors need to be considered carefully: the film homogeneity, the film-substrate boundary and phonon spectrum of the film. Despite experimental disputes, there are several cases reported, including experiments on relatively clean and thick aluminum films[10], thin and quench-condensed films[11].

Figure 5.1 shows our magnetoresistance data of quasi-1D and 2D samples and the fits to weak localization theory[6,12]. (The fits were done with $\tau_{so}^{-1}=0$ because our data at the lowest temperature couldn't determine τ_{so}^{-1} unambiguously.) From the fit we extract the electron phase breaking rate and the temperature dependence of L is shown in figure 5.2a for the quasi-1D wires and in figure 5.2b for the 2D films. The straight lines are linear least-squares fit to the data. For the temperature range T= 1.6 ~ 16 K, $\tau_{in}^{-1} \propto T^2$ is observed with a typical experimental value of τ_{in} (1.6 K) ~ 10-10 s. (This inelastic scattering time is estimated from sample #1 which has the diffusion constant $D = 2.5 \times 10^{-3} \text{ m}^2/\text{s.}$) Licini et al.[13] also measured weakly localized behavior in quasi-1D Li films and reported the $\tau_{in}^{-1} \propto T^2$ dependence down to 0.25 K with τ_{in} (1 K) \sim 1 x 10⁻¹⁰ s. The observed single power law of $\tau_{in}^{-1} \propto T^2$ behavior is consistent in form with clean-limit electron-electron scattering, the pure electron-phonon scattering involving two-dimensional phonons or the 3D electron-phonon scattering in the dirty metal. The inelastic lifetime due to the clean-limit electron-electron interaction is order of 10⁻⁷ ~10⁻⁸ s[14] and is too big to explain the experimental values. The electron-phonon scattering modified by the impurities yields the lifetime of order of $10^{-11} \sim 10^{-12}$ s[6] and the application of the dirty-limit electron-phonon scattering is questionable because the product $q_{\mathcal{I}} l_e$ is not less than 1 in the temperature range of interest. Belitz et al. [15] found the asymptotic expansion used for the electron-phonon scattering to be invalid above helium temperature and explained experimental results showing $\tau_{in}^{-1} \propto T^2$ for $T = 4 \sim 20$ K, from Bergmann and collaborators as a superposition of Coulomb and a two-dimensional electron-phonon contribution. However, the observation of $\tau_{in}^{-1} \propto T^2$ in Li films down to the temperature 0.25 K is quite puzzling at this moment and further investigation of the phase breaking mechanism in Li films needs to be carried out to clarify this problem.

From the weak localization phenomena, we were able to identify the relative strength of the spin-orbit scattering compared to the inelastic scattering. The negative magnetoresistance shown in figure 5.1 confirmed that our Li films were in the low SO scattering limit. We observed, however, the suppression of the phase coherence compared with samples discussed in Chapter 4 and saturation of L_{ϕ} at low-temperature, which results in the finite intercept at T=0 in the plot of L_{ϕ} -2 versus T2 shown in figure 5.2. The sample #1 yields L_{ϕ} -2 = 0.58 T2 + 9.8 (μ m-2) and sample #2 yields L_{ϕ} -2 = 0.79 T2 + 27.6 (μ m-2). We believe that the finite intercept at T=0 arises from residual magnetic scattering with very weak spin-orbit scattering [13].

5D. 1/f noise and UCF

5D.1 Orbital effect on UCF

Spin-flip scattering breaks the phase coherence of the electron, and leads to the suppression of conductance fluctuations. Theoretically, it is shown that spin-flip scattering suppresses the cooper and diffuson channels equally[16], so one should be able to observe the noise reduction by a factor of exactly 2 with application of magnetic field.

Figure 5.3a shows the relative 1/f noise power of sample #1 as a function of the perpendicular magnetic field at temperatures of 1.6 K and 4.2 K. As the theory predicted, the noise drop by a full factor of 2 at 1.6 K. The noise at 4.2 K does not quite drop to a full factor of 2 because there is a small contribution of local-interference type noise which is magnetic field independent, as discussed in Chapter 4. Figure 5.3b also shows the 1/f noise power versus magnetic field at temperatures of 1.6 K, 4.2 K and 10 K, measured in sample #2. We also observed the full factor of 2 reduction in the noise at 1.6 K and a small contribution of LI type noise at the other temperatures.

The 1/f noise crossover function due to the suppression of the orbital contribution (cooper channel) is governed by the phase breaking length, $L_{\varphi}[16,17]$. Therefore, we can extract another reliable estimate of L_{φ} from the noise measurement and compare the value of L_{φ} with that from magnetoresistance. In the fit of the noise data, we set $\tau_{so}^{-1}=0$ and include a second parameter to account for the LI contribution[18]. (See Eq. (4.1) in Chapter 4) The solid lines in figure 5.3 are the theoretical evaluations of the 1/f noise crossover and show excellent fit to the data. The fit parameters for sample #1 are c = 0 and 0.2 and $L_{\varphi}=0.28$ and 0.22 μ m at 1.6 K and 4.2 K, respectively. The fit parameters for sample #2 are c=0, 0.14 and 0.16 and $L_{\varphi}=0.19$, 0.14 and 0.09 μ m at 1.6 K, 4.2 K and 10 K, respectively.

In figure 5.4 the values of L_{ϕ} obtained from the noise data are compared with those from the magnetoresistance. Both measurements yield very close values of L_{ϕ} even though we observed finite spin-flip scattering in our samples. Chadrasekhar *et al.* [19] show that the spin-flip scattering effect on the conductance fluctuations can be incorporated via L_{ϕ} in the singlet(s) and triplet(t) channel:

$$L_{\phi,s}^{UCF} = [L_{in}^{-2} + L_{sf}^{-2}(B)]^{-1/2}$$

$$L_{\phi,t}^{UCF} = [L_{in}^{-2} + L_{sf}^{-2}(B) + \frac{4}{3}L_{so}^{-2}]^{-1/2}$$
(5.1)

where L_{in} is the inelastic length and L_{sf} is the spin-flip scattering length. In the magnetoresistance the spin-flip scattering rate enters into the phase breaking length of the singlet and triplet channel in a slightly different way[6,10,13]:

$$L_{\phi,s}^{WL} = [L_{in}^{-2} + 2L_{sf}^{-2}(B)]^{-1/2}$$

$$L_{\phi,t}^{WL} = [L_{in}^{-2} + \frac{2}{3}L_{sf}^{-2}(B) + \frac{4}{3}L_{so}^{-2}]^{-1/2}$$
(5.2)

In the strong SO scattering regime, a finite spin-flip scattering yields a big difference in the measured value of L_{φ} from the two methods because the triplet channel is suppressed. In the negligible SO scattering limit, the singlet and triplet channel have the same diffusion length in the noise measurement but not in the magnetoresistance measurement. Since magnetoresistance measurements yield the longer diffusion length in the triplet channel and the shorter diffusion length in the singlet channel compared to that from the noise measurement, it is not surprising to get a very close value of L_{φ} from these two measurements on our samples.

Since the fit parameter L_{ϕ} in the low-field noise data is $L_{\phi} = L_{\phi,s}^{UCF} = [L_{in}^{-2} + L_{sf}^{-2}]^{-1/2}$, the spin-flip diffusion length L_{sf} can be estimated if we know the inelastic length L_{in} . From the slope of the L_{ϕ}^{-2} versus T^2 plot for sample #1 in figure 5.2, the inelastic diffusion length L_{in} is estimated as 0.78 μ m at 1.6 K. Then L_{sf} is estimated as 0.30 μ m, given $L_{\phi} = 0.28 \mu$ m from the fit to the noise data and we get $L_{\phi,s}^{WL} = 0.2 \mu$ m, $L_{\phi,t}^{WL} = 0.33 \mu$ m. The noise measurement provides $L_{\phi,s}^{UCF} = L_{\phi,t}^{UCF} = 0.28 \mu$ m. The inferred length scales for singlet and triplet channel from two measurements are larger than the sample width (0.11 μ m), ensuring

that quasi-1D localization theory is valid in our sample. For sample #2, we get $L_{\rm sf}$ = 0.2 μm .

5D.2 Spin effect on UCF

Figure 5.5 shows the magnetic field dependence of the relative 1/f noise power up to 9T obtained from sample #1. (Data below 0.5 T has been discussed in figure 5.3.) The noise power increases with field dramatically when B > 0.5 T at 1.6 K, and slightly when B > 1T at 4.2 K. This behavior is in contrast to the reduction, we saw in Ch. 4, due to the Zeeman splitting of the conductance electrons. Figure 5.6 shows similar behavior of the relative 1/f noise power from sample #2.

A possible explanation of the behavior shown in figures 5.5 and 5.7 is based on the assumption that there is a finite residual spin-flip scattering in the sample, as observed in the magnetoresistance. The strong magnetic field aligns the magnetic impurities and suppresses the spin-flip scattering, leading to the restoration of the phase coherence and the amplitude of conductance fluctuations. The magnetic field scale needs to be of order k_BT/μ_{imp} [2], which corresponds to 1.1 T and 3.1 T at 1.6 K and 4.2 K respectively if we assume $\mu_{imp} = 2\mu_B$. The estimated magnetic field scales are close to the experimentally observed values.

To analyze the data quantitatively, spin-flip scattering needs to be incorporated into UCF. Benoit et al. [20] assumed that (1) only the lowest two magnetic energy levels of the impurity would be important, so that the magnetic impurity could be treated as spin 1/2 and (2) the magnetic scattering rate would be proportional to P_uP_d where P_u and P_d are the probabilities of the spin 1/2 impurity being in the up or down state. The calculation of the magnetic field dependence of the spin-flip scattering rate gives:

$$L_{\phi}^{-2} = L_{in}^{-2} + L_{sf}^{-2} (B = 0) \frac{1}{\cosh^{2}(\frac{\mu_{imp}B}{k_{B}T})}$$
 (5.3)

At high magnetic field, the electron Zeeman splitting needs to be considered in the system with electron spin symmetry [16,21]. (See also Chapter 4) Unfortunately, the situation is more complicated due to the finite spin-flip scattering, $L_{\text{sf}}/L_{\text{in}} \sim 0.4$ and 0.3 at 1.6 K for sample #1 and #2, respectively. Since strong spin-flip scattering breaks the electron spin symmetry, we assume that the Zeeman effect on UCF is negligible in our samples. (See figure 4.7 for the Zeeman effect on UCF.) Then the theoretical function for the noise with the spin flip scattering is obtained following Eq. (2.31) and (5.3), where the parameters are L_{in} , $L_{sf}(B=0)$ and μ_{imp} . We used the values of L_{in} and $L_{sf}(B=0)$ determined by the low-field fit. The solid lines at highfield in figure 5.8 show our fits to the theoretical expression with only a single fit parameter $\mu_{imp} = 0.7 \mu_B$. The simple theoretical function matches the data fairly well and describes the temperature and field dependence of the noise power at high-field. Even though not all of the features in the noise data are explained from the simple model, we clearly observe the effect of the spin-flip scattering on the conductance fluctuations, and our data at high- magnetic field are consistent with previous work[4,20]. All the previous work related to the effect of the spin-flip scattering on the conductance fluctuations have been carried out at high magnetic field and found that the amplitude of conductance fluctuations increases with field.

5.E Summary

We have fabricated mesoscopic Li films using quench-condensation and measured both the weak-localization contribution to the average conductance and the conductance fluctuations in-situ. From the magnetoresistance, we are able to extract the electron phase breaking length and its temperature dependence. The magnetoresistance data confirm the low spin-orbit scattering in our Li films but show the suppression of the phase coherence due to the finite spin-flip scattering.

We observe that the noise power is reduced by a full factor of 2 with an application of weak magnetic field. This observation is consistent with the theoretical prediction that the spin-flip scattering suppresses the conductance fluctuations equally in the cooper and diffuson channel and an application of magnetic field suppresses the cooper channel contribution to UCF. This is one of our important results which has not been observed previously. We used the noise reduction versus magnetic field to measure L_{φ} and found that the value of L_{φ} is very close to that from the weak-localization measurement.

The amplitude of conductance fluctuations increases dramatically with high magnetic field. We attribute this behavior to the alignment of the magnetic impurities at the high magnetic field and the suppression of the spin-flip scattering. We developed a simple model following Benoit *et al.* [20] to fit our data over the magnetic field and the temperature. This paramagnetic model describes the data fairly well with a single value of the temperature-independent parameter μ_{imp} .

References

- [1] Mesoscopic Phenomena in solids, edited by B. L. Al'tshuler, P. A. Lee, and R. A. Webb (North-Holland, New York, 1991).
- [2] B. L. Al'tshuler and B. Z. Spivak, JETP Lett. 42, 447 (1985); P. A. Lee and T. V. Ramakrishnan, Rev. Mod. Phys. 57, 287 (1987); V. I. Fal'ko, JETP Lett. 53, 340 (1991); A. A. Bobkov, V. I. Fal'ko, and D. E. Khmel'nitskii., Sov. Phys. JEPT 71, 393 (1990)
- [3] Wei W, G. Bergmann and R-P. Peters, Phys. Rev. B 38, 11751 (1988).
- [4] S. Washburn and R. A. Webb, Adv. Phys. 35, 375 (1986); A. K. Geim et al., JETP Lett. 52, 247 (1990); W. F. Smith et al., Phys. Rev. B 43, 12267 (1991).
- [5] N. Papanikolaou et al., Phys. Rev. Lett. 71, 629 (1993).
- [6] For an excellent review, see G. Bergman, Phys. Report 107, 1 (1984).
- [7] B. L. Al'tshuler et al., Sov. Sci. Rev. A. Phys. 9, 223 (1987).
- [8] A. Schmid, Z. Phys. **259**, 421 (1973).
- [9] G. Bergmann, Z. Phys. B 48, 5 (1982).
- [10] P. Santhanam, S. Wind, and D. E. Prober, Phys. Rev. B 35, 3188 (1987).
- [11] R. P. Peters and G. Bergmann, J. Phys. Soc. Jpn. 54, 3478 (1985).
- [12] B. L. Al'tshuler and A. G. Aronov, Pis'ma Zh. Eksp. Teor. Fiz. 33, 515 (1981) [JETP Lett. 33, 499 (1981)]
- [13] J. C. Licini, G. J. Dolan, and D. J. Bishop, Phys. Rev. Lett. 54, 1585 (1985)
- [14] N. W. Ashcroft and N. D. Mermin, *Solid State Physics* (Holt, Rinehart and Winston, New York, 1976), P. 346 ff.
- [15] D. Belitz, S. D. Sarma, Phys. Rev. B 36, 7701 (1987).
- [16] A. D. Stone, Phys. Rev. B 39, 10736 (1989); P. A. Lee, A. D. Stone, and H. Fukuyama, Phys. Rev. B 35, 1039 (1987).

- [17] C. W. J. Beenakker and H. van Houten, phys. Rev. B 37, 6544 (1988)
- [18] J. Pelz and J. Clarke, Phys. Rev. B 36, 4479 (1987)
- [19] V. Chandrasekhar et. al, Phys. Rev. B 42, 6823 (1990).
- [20] A. Benoit et. al, in *Anderson Localization*, edited by T. Ando and H. Fukuyama (Springer-Verlag, Berlin, 1988), p. 346.
- [21] S. Feng, Phys. Rev. B 39, 8722 (1989).

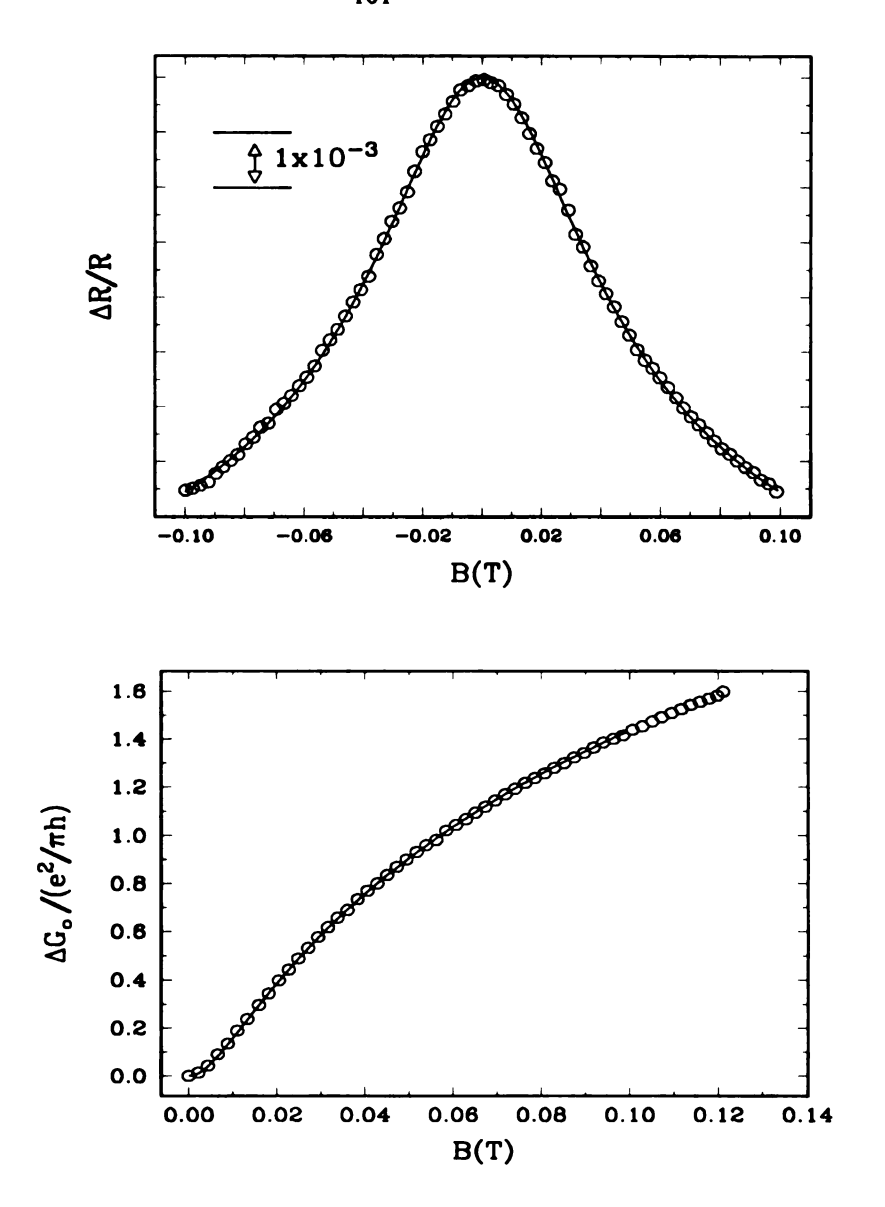


Figure 5.1 (a) Magnetoresistance of quasi-1D Li sample #1 (W = 0.11 μ m, R_{\square} = 5.7 Ω) taken at T=2 K. The solid line is the fit to the quasi-1D weak localization theory. (b) Magnetoresistance of 2D Li sample #3 (W = 205 μ m, R_{\square} = 7.8 Ω) taken at T=3.5 K. The solid line is the fit to the 2D weak localization theory.

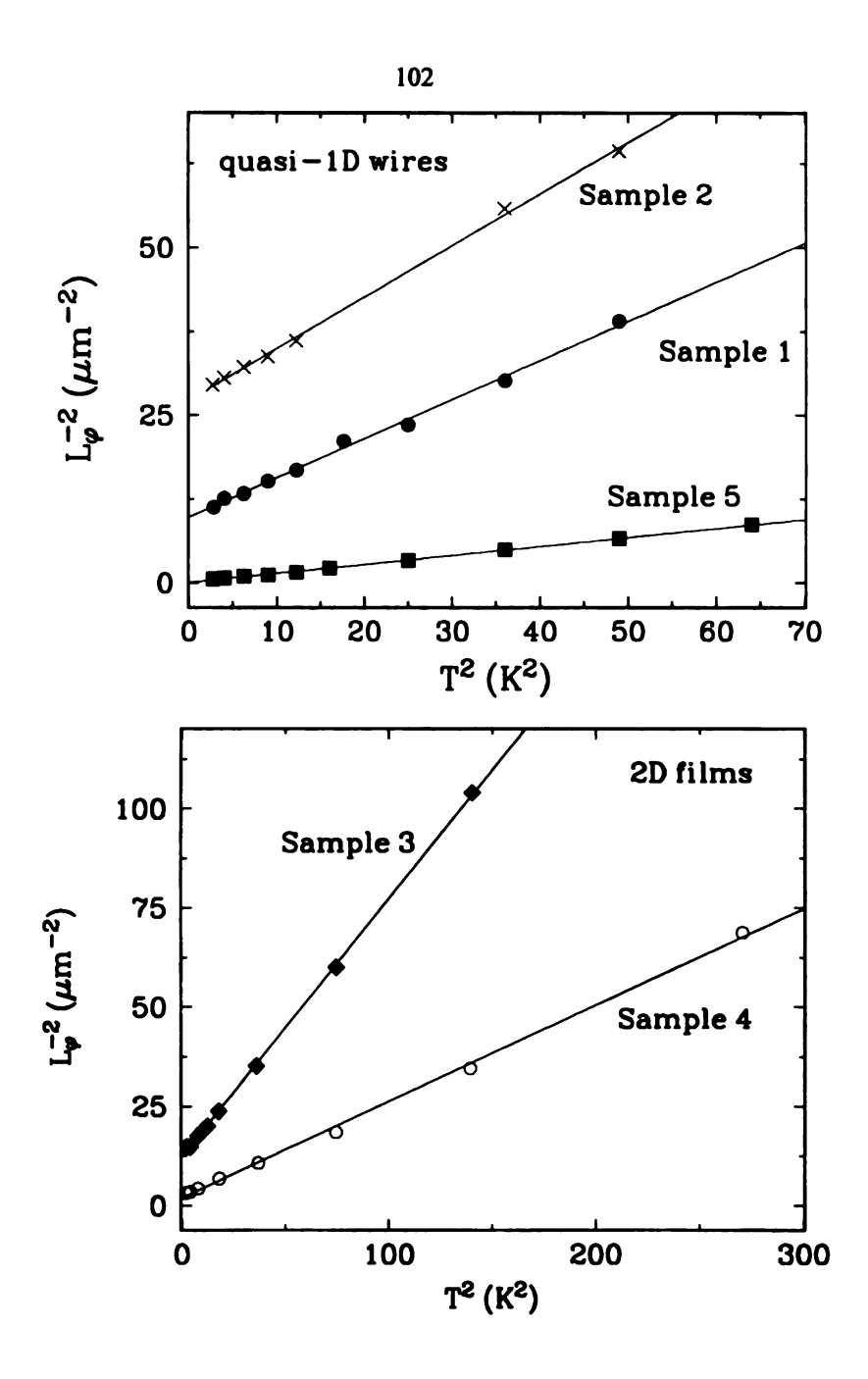


Figure 5.2 The electron phase breaking length versus temperature, obtained from the weak-localization fits of low field magnetoresistance (a) for quasi-1D wires and (b) for 2D films. The data for sample 5 (a) in fig. 5.2a are discussed in chapter 4 and are shown for contrast since they have no residual spin-flip scattering.

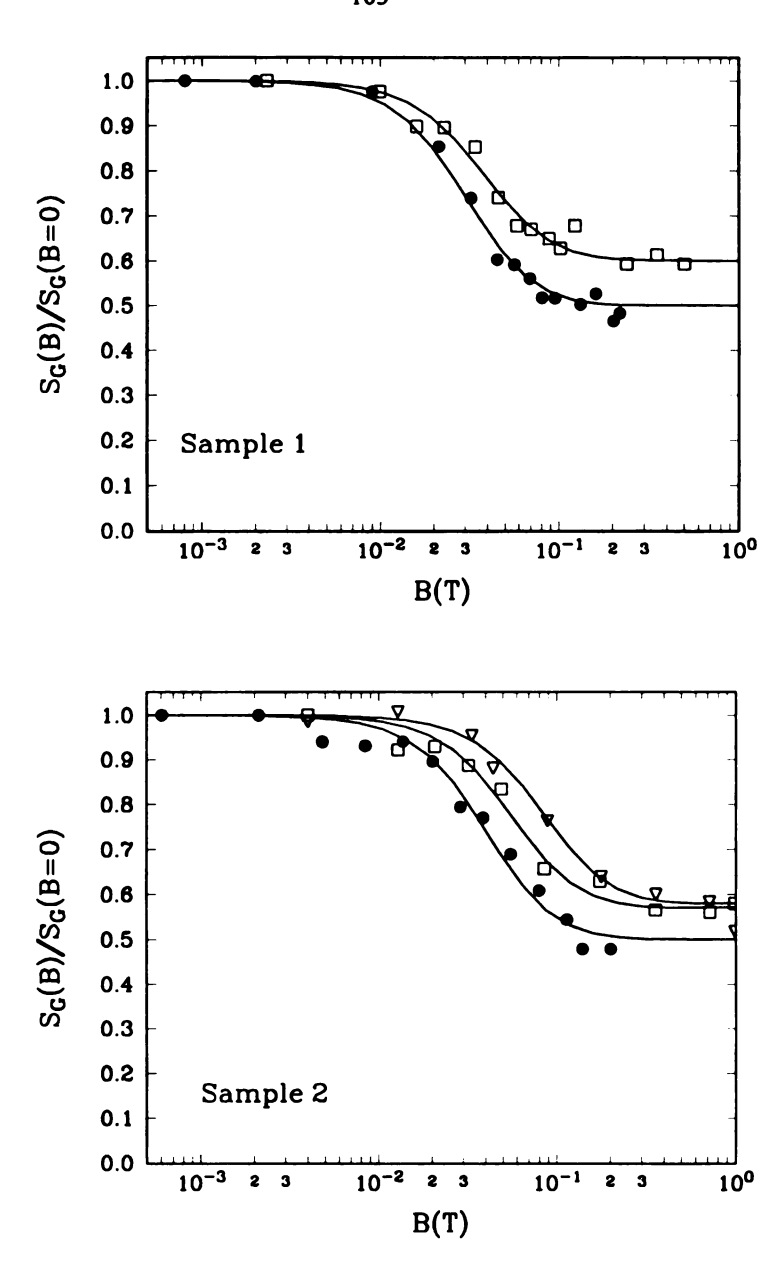


Figure 5.3 Conductance noise power as a function of the perpendicular magnetic field, normalized by its zero-field value. (a) The data for sample 1 are taken at the temperatures 1.6 K(\bullet) and 4.2 K(\square). (b) The data for sample 2 are taken at the temperatures 1.6 K(\bullet), 4.2 K(\square) and 10 K(∇). The solid lines are the least-squares fits to Eq. (4.1), as discussed in the text.

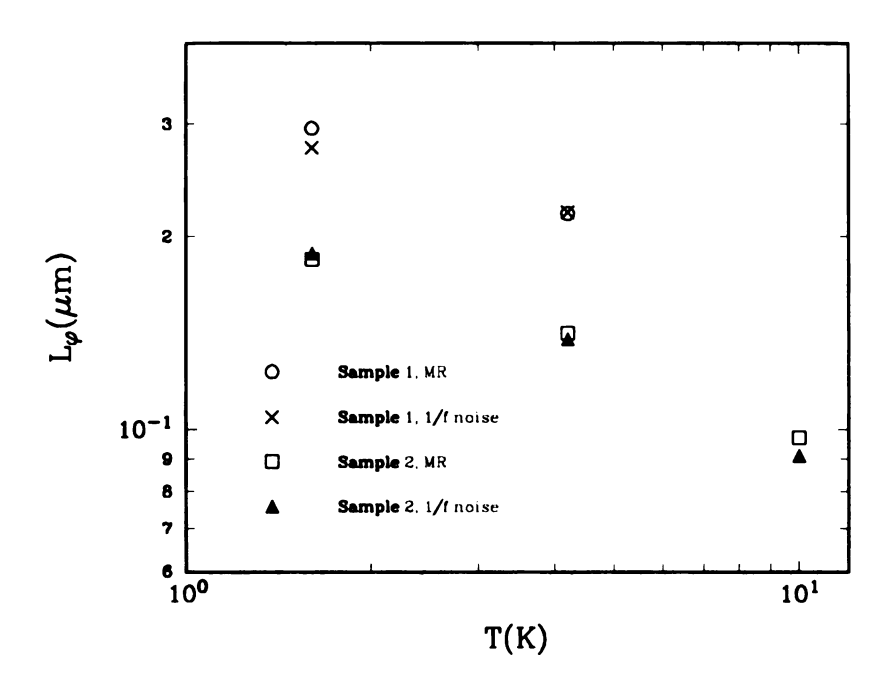


Figure 5.4 Values of the phase breaking length, obtained from the fits to the data of noise vs magnetic field in figure 5.3, and obtained from the magnetoresistance data in figure 5.2.

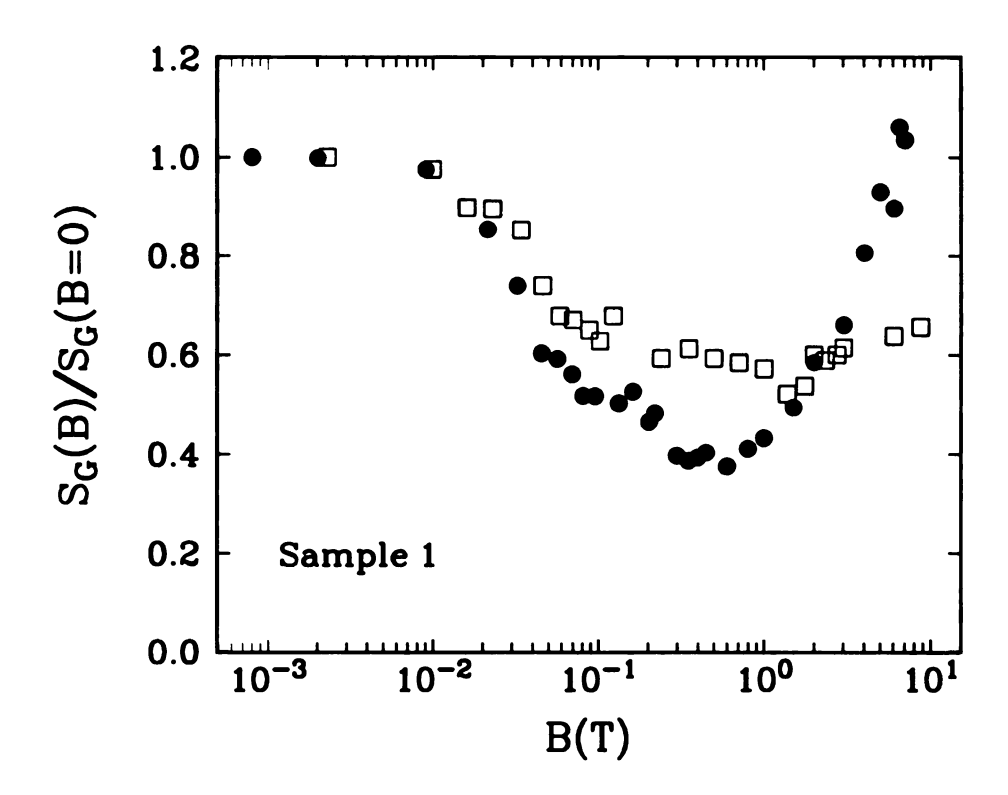


Figure 5.5 Noise power as a function of magnetic field from sample #1 at temperatures 1.6 K(•) and 4.2 K(□). (The data are normalized by the noise power at zero-field.)

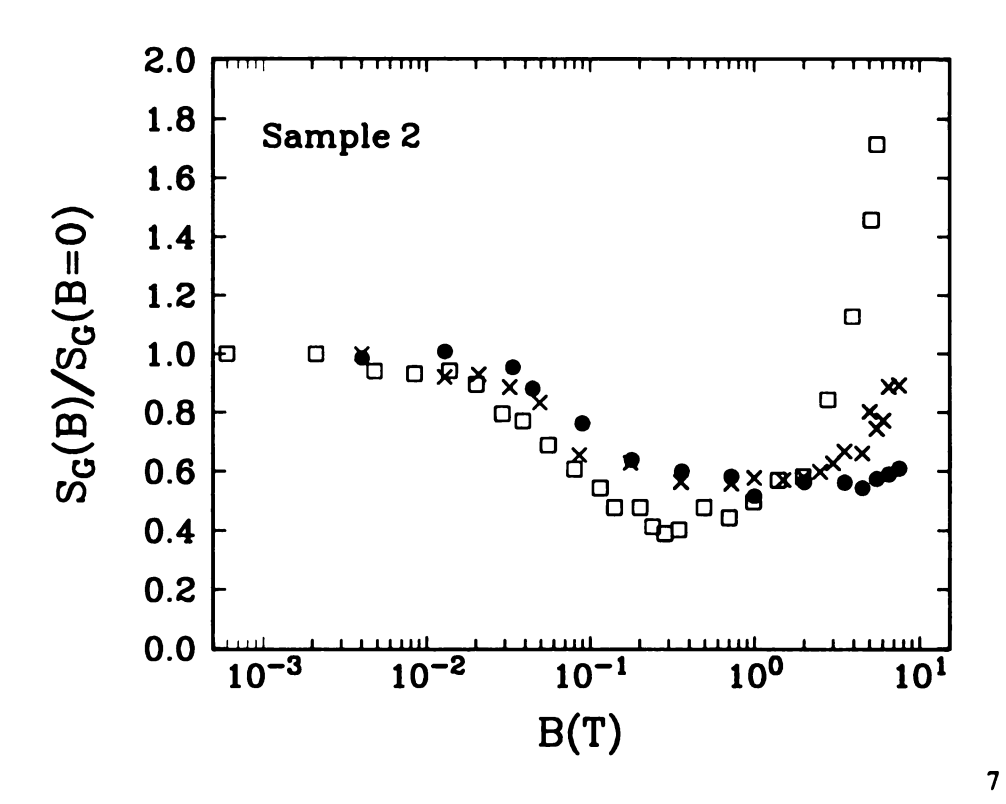


Figure 5.6 Noise power as a function of magnetic field from sample #2 at temperatures 1.6 K(\square), 4.2 K(x) and 10 K(x). (The data are normalized by the noise power at zero-field.)

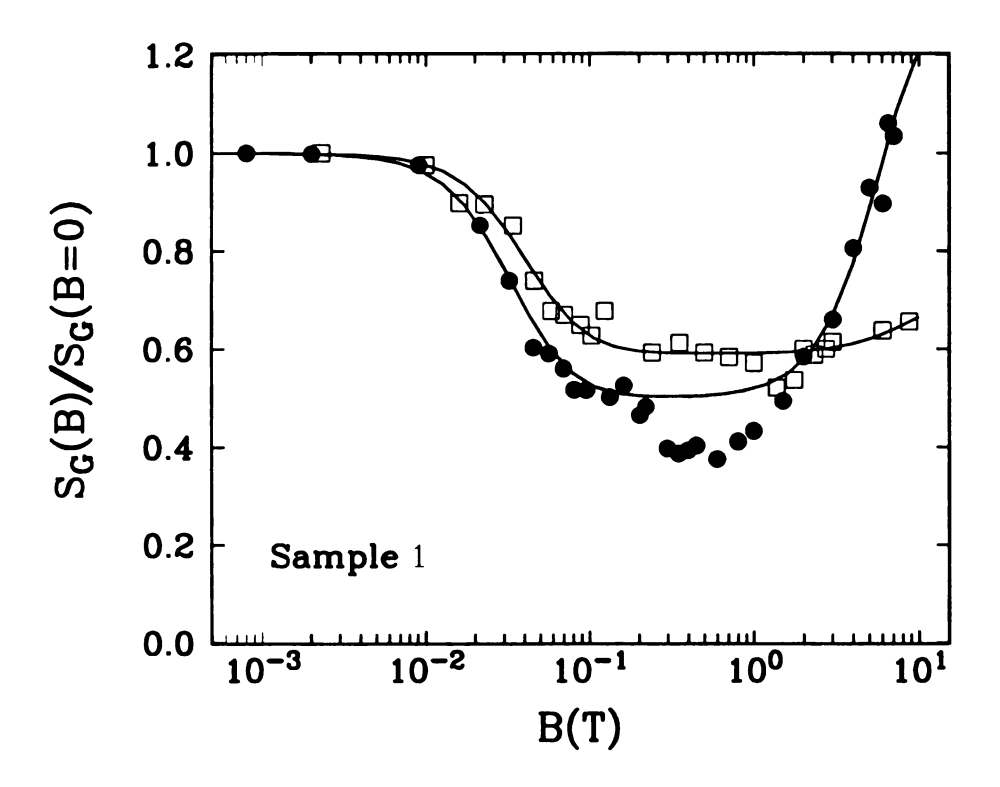


Figure 5.7 A fit to the noise power as a function of magnetic field from sample #1 at temperatures 1.6 K(\bullet) and 4.2 K(\square). The low field reduction fit to the quasi-1D theory is discussed in figure 5.4a. The noise data at high field is fit to the simple paramagnetic impurity model as discussed in the text.

Chapter 6

CONCLUSIONS

We have studied quantum transport in the low spin-orbit scattering limit by measuring the universal conductance fluctuations as a function of magnetic field and the weak-localization correction to the average conductance in mesoscopic Li wires and films. We were able to obtain several significant results which provide us with a better understanding of UCF and provide a chance to study random matrix theory pioneered by Wigner and Dyson.

First, we observed a factor of 2 reduction in the amplitude of UCF with application of weak magnetic field. We attribute the reduction to the suppression of the orbital effect on UCF which can be viewed as the crossover from Gaussian orthogonal ensemble to the Gaussian unitary ensemble due to broken time-reversal invariance. We calculated the UCF crossover function and found very good agreement with our data. We confirmed that the crossover field scale is determined by one flux quantum over the phase coherent area.

Second, we observed a second factor of 2 reduction in the amplitude of UCF with application of strong magnetic field. We attribute this reduction to lifting the Zeeman degeneracy of the conductance electrons, and found that our data are consistent with diagrammatic calculations. Our results show that the magnetic field scale for the Zeeman crossover is determined by the larger of the sample temperature and Thouless energy. This is very different from previous work, where the field scale was presumed to be determined by the Thouless energy alone.

Both observations are consistent with the predictions of the random matrix approach, which provides a more fundamental understanding of UCF. The

conductance is determined by the transmission matrix, the conductance fluctuations are universal in the diffusive regime and ultimately determined by the ensemble symmetry. Since the "universality" is generic for a whole class of transport properties in mesoscopic conductors and superconductors, future experiments can be carried out in several directions, including shot-noise, normal-superconductor interfaces and Josephson junctions.

We also studied the effect of spin-flip scattering on UCF in the low spin-orbit scattering regime. We confirmed the theoretical prediction that the spin-flip scattering suppresses the conductance fluctuations equally in the cooper and diffuson channel, by measuring the noise reduction by a full factor of 2 with application of a weak magnetic field. At high magnetic field, we observe that the amplitude of conductance fluctuations increases in a dramatic way and the increase in the noise power is highly temperature sensitive. We used a simple model based on residual paramagnetic scattering and found that the model describes our data fairly well.

Appendix

A. 1/f noise.

In disordered metals, defects or impurities can move either by tunneling at low temperature or by hopping at high temperature. This spontaneous rearrangement of scattering centers gives rise to temporal fluctuations in the interference pattern among all the paths in a coherent volume. This causes dynamical fluctuations of the conductance. Feng, Lee and Stone showed that the low-temperature conductance is extremely sensitive to a single impurity movement by a distance $\delta r \geq k_F^{-1}$. In the case of $k_F l_e = 1$ (close to strong localization), a single impurity can cause saturation of the conductance fluctuations, i.e. $\delta G \approx e^2/h$. In most metals, $k_F l_e$ is bigger than 1, so the conductance change due to the motion of a single impurity (δG_1) is much smaller than e^2/h . This case is called unsaturated noise.

The standard way to measure resistance noise is to apply a current through the sample, and monitor the temporal fluctuations of the voltage across the sample. Figure A shows a typical 1/f noise and background Johnson noise in the time domain. The power spectrum of the voltage fluctuations is given by

$$S_{V}(\omega) = \frac{2}{\pi} \int \langle \delta V(t') \delta V(t'+t) \rangle \cos \omega t dt$$

where $\delta V(t) = V(t) - \langle V \rangle$, and the brackets refer to an average over t'.

To understand the power spectrum of the noise, consider a random process with a single characteristic time τ from a defect moving between two or more positions. The power spectrum of that process is a Debye-Lorentzian spectrum:

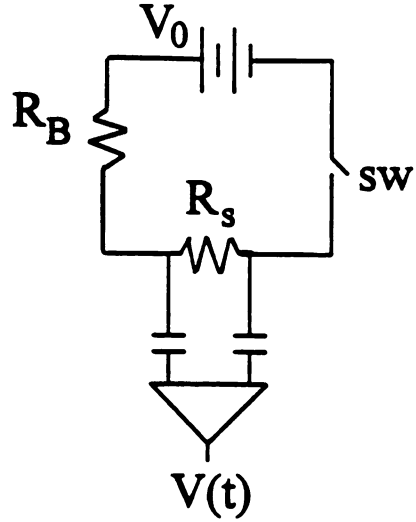
$$S^d(\omega) \propto \frac{\tau}{1+\omega^2\tau^2} (\delta G_1)^2$$

For the slow dynamical rearrangement of many impurities, we should consider the distribution $D(\tau)$ of the characteristic times of the impurities within a sample. Then

$$S_G(\omega) \propto (\delta G)^2 \int \frac{\tau}{1+\omega^2 \tau^2} \cdot D(\tau) d\tau$$

The $D(\tau)$ depends on the microscopic details of the disordered system. For the cases of thermal activation or tunneling, the characteristic time for a defect motion depends exponentially on parameters which are distributed broadly, so $D(\ln(\tau))$ is constant ($D(\tau) \sim \tau^{-1}$) over a wide range of τ . The resistance fluctuations show the "1/f" power spectrum.

A simple circuit for noise.



(sw--open): Johnson noise.



(sw--closed): Johnson noise + 1/f noise.

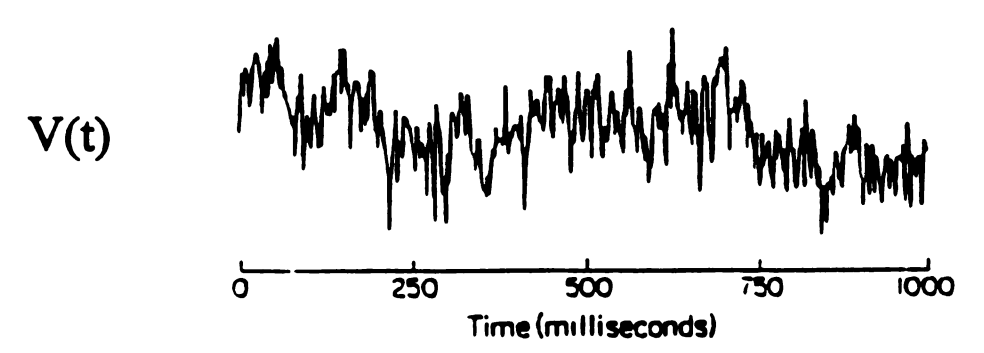


Figure A (a) Schematic diagram of noise measurement set-up.

- (b) Temporal presentation of background Johnson noise.
- (c) Temporal presentation of 1/f noise and background.

MICHIGAN STATE UNIV. LIBRARIES
31293014100345